Universität Hamburg
DER FORSCHUNG | DER LEHRE | DER BILDUNG

FAKULTÄT
FÜR MATHEMATIK, INFORMATIK
UND NATURWISSENSCHAFTEN

Dynamics of driven antiferromagnetic skyrmions

Dissertation

zur Erlangung des Doktorgrades
an der Fakultät für Mathematik,
Informatik und Naturwissenschaften

Fachbereich Physik

Universität Hamburg

vorgelegt von

Michael Matthias Lau

Hamburg
2025

Gutachter/innen der Dissertation:	Prof. Dr. Michael Thorwart Prof. Dr. Michael Potthoff
Zusammensetzung der Prüfungskommission:	Prof. Dr. Michael Thorwart Prof. Dr. Michael Potthoff Prof. Dr. Daniela Pfannkuche PD Dr. Wolfgang Häusler PD Dr. Kirsten Tina von Bergmann
Vorsitzende/r der Prüfungskommission:	Prof. Dr. Daniela Pfannkuche
Datum der Disputation:	08.05.2025
Vorsitzender des Fach- Promotionsausschussess PHYSIK:	Prof. Dr. Wolfgang J. Parak
Leiter des Fachbereichs PHYSIK:	Prof. Dr. Markus Drescher
Dekan der Fakultät MIN:	Prof. Dr.-Ing. Norbert Ritter

Abstract

Magnetic Skyrmions are vortex-like quasi-particles stabilized by their topology and exist in several magnetic materials. While originally described by continuous vector fields that ensure topological protection, stable Skyrmions can also form in magnetic lattices, allowing for their experimental observation. Not least due to their potential applications in magnetic storage devices, Skyrmions have gained popularity since their first experimental observation in 2009. Ferromagnetic (FM) Skyrmions are nanometer-sized and can be driven by electric currents. They move as massless particles at an angle to the current flow and, therefore, exhibit the Skyrmion Hall effect. While ferromagnetic Skyrmions are still extensively studied in current research, the field of study evolve further to advanced structures. An emerging topic is the study of antiferromagnetic (AFM) Skyrmions. Unlike their ferromagnetic counterparts, AFM Skyrmions do not exhibit the Skyrmion Hall effect and can reach higher velocities when driven by electric currents, making them more attractive for technological applications. Moreover, AFM Skyrmions have a finite mass and exhibit behavior akin to classical particles, making them a fascinating subject for fundamental research.

Theoretical studies of AFM Skyrmions typically focuses on either synthetic antiferromagnets or G-type antiferromagnets, making it crucial to understand the distinctions between them. Synthetic antiferromagnets are a composition of two or more ferromagnetic layers that are coupled antiferromagnetically through a non-magnetic spacer layer. In contrast, G-type antiferromagnets exhibit a chessboard-like structure, where the sublattices are within the same layer. While Skyrmions have been experimentally observed in synthetic antiferromagnets, they remain elusive in other types of antiferromagnetic systems up to now. Both types are considered in this thesis. After introducing classical micromagnetic dynamics and general properties of a magnetic Skyrmion, we will discuss these two realizations of antiferromagnets. Furthermore, we will demonstrate that, independent of the type, the antiferromagnetic system can be treated as two effectively coupled ferromagnetic sublattices. In this thesis, the underlying mechanics of antiferromagnetic Skyrmion dynamics play a crucial role. To investigate them, we utilize the separation into two sublattices and treat the Skyrmions forming on these sublattices as rigid objects. This approach reveals that the driving mechanism of an AFM Skyrmion is due to a small displacement of its sublattice constituents. We develop a formalism that incorporates this mechanism and demonstrate that an AFM Skyrmion eventually mirrors the dynamics of a classical particle with finite mass. Furthermore, this framework allows us to fully characterize the resulting motion of an AFM Skyrmion driven by an external force. We apply this formalism to the case of current-driven Skyrmions, showing that it can predict the dynamics of an antiferromagnetic Skyrmion, regardless of the type of antiferromagnet, in various scenarios, even in fine detail. All results are compared to micromagnetic simulations.

As another possibility for driving AFM Skyrmions, we examine spin wave-driven Skyrmions in the second part of this thesis, focusing on a two-dimensional square lattice. We begin

with formulating a classical spin wave theory explicitly tailored to this system by linearizing the equations of motion around a homogeneous ground state. This allows us to derive the dispersion relation and characterize different types of spin wave polarization, namely circularly and linearly polarized spin waves. All results are confirmed by simulations. Subsequently, we investigate the impact of spin waves on the Skyrmion. To do so, we simulate an isolated Skyrmion in the lattice and inject the spin wave via edge spin manipulation. Our observations reveal that spin waves generally accelerate the Skyrmion. While linearly polarized spin waves move the Skyrmion in the direction of wave propagation, circularly polarized spin waves induce an additional motion perpendicular to this direction, resulting in a Skyrmion Hall effect. The resulting Skyrmion acceleration depends on the properties of the spin wave, such as its wave number and amplitude. Furthermore, we investigate the impact of damping on spin waves and the resulting Skyrmion motion. We derive an expression for the decay of spin waves as they propagate through the lattice, focusing on the decay length. Additionally, we propose a concept for an antiferromagnetic Skyrmion racetrack that incorporates both spin wave decay and the Skyrmion Hall effect.

Zusammenfassung

Magnetische Skyrmionen sind vortex-artige Quasiteilchen, die durch ihre Topologie stabilisiert werden und in verschiedenen magnetischen Materialien beobachtet wurden. Während sie ursprünglich durch kontinuierliche Vektorfelder beschrieben wurden, welche den topologischen Schutz gewährleisten, können auch in magnetischen Gittern stabile Skyrmionen entstehen, was eine Beobachtung in realen Experimenten ermöglicht. Nicht zuletzt aufgrund potenzieller Anwendung in magnetischen Speichervorrichtungen haben Skyrmionen seit ihrer ersten experimentellen Beobachtung im Jahr 2009 an Beliebtheit gewonnen. Ferromagnetische (FM) Skyrmionen haben eine Größe im Nanometerbereich und können durch elektrische Ströme bewegt werden. Sie bewegen sich wie masselose Teilchen in einem Winkel zur Stromrichtung und weisen somit den Skyrmion-Hall Effekt auf. Auch wenn ferromagnetische Skyrmionen weiterhin umfassend in der aktuellen Forschung untersucht werden, entwickelt sich das Forschungsfeld weiter zu fortgeschritteneren Strukturen. Ein aufkommendes Thema ist das Studium von antiferromagnetischen (AFM) Skyrmionen. Im Gegensatz zu ihren ferromagnetischen Verwandten unterliegen AFM Skyrmionen nicht dem Skyrmion-Hall Effekt und können höhere Geschwindigkeiten erreichen, wenn sie durch elektrische Ströme angetrieben werden. Das macht sie für technologische Anwendungen attraktiver. Darüber hinaus haben AFM Skyrmionen eine endliche Masse und zeigen die gleichen dynamischen Verhaltensweisen wie ein klassisches massives Teilchen, was sie zu einem faszinierenden Thema für die Grundlagenforschung macht.
Theoretische Studien zu AFM Skyrmionen beziehen sich typischerweise entweder auf synthetische Antiferromagneten oder G-Typ Antiferromagneten. Daher ist es wichtig, die Unterschiede zwischen den beiden Typen zu verstehen. Synthetische Antiferromagneten

setzen sich aus zwei oder mehr ferromagnetischen Schichten zusammen, die antiferromagnetisch über eine nicht-magnetische Zwischenschicht gekoppelt sind. Im Gegensatz dazu weist der *G*-Typ Antiferromagnet eine schachbrettartige Struktur auf, bei der sich die Untergitter innerhalb derselben Schicht befinden. Während Skyrmionen in synthetischen Antiferromagneten experimentell beobachtet wurden, konnten sie bis heute in anderen Arten von antiferromagnetischen Systemen noch nicht experimentell nachgewiesen werden. Beide Typen werden in dieser Dissertation betrachtet. Nach einer Einführung in die Dynamik klassischer Magnetfelder und die allgemeinen Eigenschaften eines magnetischen Skyrmions, werden wir die beiden zuvor erwähnten Arten von Antiferromagneten diskutieren. Darüber hinaus werden wir zeigen, dass das antiferromagnetische System, unabhängig vom Typ, als zwei separate, effektiv gekoppelte, ferromagnetische Untergitter behandelt werden kann. In dieser Dissertation spielt der zugrunde liegende Mechanismus der antiferromagnetischen Skyrmion-Dynamik eine entscheidende Rolle. Um diesen zu studieren, nutzen wir die Separation des Systems in zwei Untergitter und betrachten die Skyrmionen, die von diesen Untergittern gebildet werden, als starre Körper. Mit diesem Ansatz sehen wir, dass der treibende Mechanismus des AFM Skyrmions auf einer kleinen Verschiebung der Untergitter-Skyrmionen beruht. Wir entwickeln in dieser Arbeit einen Formalismus, der den erwähnten Mechanismus nutzt, und zeigen, dass ein AFM Skyrmion letztendlich die Dynamik eines klassischen Teilchens widerspiegelt. Darüber hinaus können wir die resultierende Bewegung eines von einer externen Kraft angetriebenen AFM Skyrmions vollständig charakterisieren. Mit der Anwendung dieses Formalismus auf stromgetriebene Skyrmionen zeigen wir, dass wir die Dynamik eines antiferromagnetischen Skyrmions, unabhängig vom Typ des Antiferromagneten, in verschiedenen Szenarien herleiten können. Alle Ergebnisse werden mit mikromagnetischen Simulationen verglichen. Als eine weitere Möglichkeit zur getriebenen Bewegung von AFM Skyrmionen untersuchen wir im zweiten Teil dieser Dissertation spinwellengetriebenen Skyrmionen in einem zweidimensionalen Quadratgitter. Dazu beginnen wir mit der Formulierung einer klassischen Spinwellentheorie, die explizit auf dieses System zugeschnitten ist, indem wir die Bewegungsgleichungen um einen homogenen Grundzustand linearisieren. Dies ermöglicht es uns, die Dispersionsrelation herzuleiten und verschiedene Arten der Polarisation von Spinwellen zu charakterisieren, nämlich zirkulär und linear polarisierte Spinwellen. Alle Ergebnisse werden durch Simulationen bestätigt. Im Anschluss daran untersuchen wir den Einfluss von Spinwellen auf das Skyrmion. Dazu simulieren wir ein isoliertes Skyrmion im Gitter und injizieren die Spinwelle durch Randspinmanipulation. Unsere Beobachtungen zeigen, dass Spinwellen im Allgemeinen das Skyrmion beschleunigen. Während linear polarisierte Spinwellen das Skyrmion in Richtung der Wellenausbreitung bewegen, verursachen zirkulär polarisierte Spinwellen eine zusätzliche Bewegung senkrecht zur Wellenausbreitungsrichtung, was den Skyrmion-Hall Effekt zur Folge hat. Die daraus resultierende Beschleunigung des Skyrmions hängt von den Eigenschaften der Spinwelle ab, wie zum Beispiel der Wellenzahl und der Amplitude. Darüber hinaus untersuchen wir den Einfluss

der Dämpfung auf Spinwellen und die Skyrmionenbewegung. Im Zuge dessen leiten wir einen Ausdruck für den Zerfall, insbesondere der Zerfallslänge, von Spinwellen während ihrer Bewegung über das Gitter her. Zusätzlich präsentieren wir ein Konzept für einen antiferromagnetischen Skyrmion Racetrack, der sowohl den Zerfall der Spinwelle als auch den Skyrmion-Hall Effekt berücksichtigt.

Publications:

- M. Lau, W. Häusler, and M. Thorwart, *Spin wave driven skyrmions in a bipartite antiferromagnetic lattice*, Phys. Rev. B **109**, 014435 (2024).
- M. Lau, W. Häusler, and M. Thorwart, *Moving skyrmions in antiferromagnets by sublattice displacements*, Phys. Rev. B **111**, 144411 (2025).

A further publication in this field does not directly enter in this thesis:

- F. Austrup, W. Häusler, M. Lau, and M. Thorwart, *Dynamics of skyrmion shrinking*, Phys. Rev. B **111**, 134446 (2025).

Contents

1. Introduction

In the classical world as we perceive it, particles are understood as objects with finite mass and a definite position in space. However, from the perspective of field theory, particles can be viewed as localized excitations of a field. Similar to a single wave traveling across the surface of the sea, the wave itself is an excitation being transported through space, while the underlying water, as the medium, remains in place. Likewise, we can characterize these excitations of a medium or field in much the same way we characterize particles. Each excitation possesses attributes such as position, momentum, extent, and a lifetime, akin to the gradual decay of a traveling sea wave over time. Beyond the illustrative example of a wave on the sea, localized excitations that form particle-like structures, known as quasi-particles, are found in various types of fields. In 1961, T. H. R. Skyrme proposed in Ref. [1] that quasi-particles can be formed in pion fields. He found a new constant of motion, identified with the number of particles N, which can only take integer numbers. Since this particle number can not be changed by a continuous transformation of the field, the particles are topologically protected. Although Skyrme found this topological constant while studying Baryon numbers, it is the same topological protection which is exhibit by a particular kind of magnetic vortices. Therefore, these vortices are today known as magnetic Skyrmions.

In 1975, A. A. Belavin and A. M. Polyakov applied the same idea of a topologically protected excitation of a continuous field to a magnetization field. They interpreted the magnetization of a material as a continuous two-dimensional vector field with constant vector length. They found that a mapping from the 2D plane (position) to the 2D sphere (vector of constant length) defines an number of times that the sphere is covered by the plane [2]. By this they found that there has to be a topologically protected state since the number of wrappings is an integer number and can not be transformed continuously. They found those states by considering only Heisenberg interaction and for high energies. Therefore, the resulting quasi-particles are, although topologically protected, high energy excitations and, thus, in reality highly unstable. By including additional energy constituents commonly found in realistic magnetic system such as the Dzyaloshinskii-Moriya interaction (DMI) and an external magnetic field, A. N. Bogdanov and D. A. Yablonskii were able to predict realistic Skyrmions in the year of 1989. They considered real materials, categorized in crystallographic classes and found that a system of thermodynamically stable magnetic vortices can be realized for a certain choice of material parameters [3]. Later in 2006, Rößler, Bogdanov, and Pfleiderer suggested in Ref. [4] that such a system of magnetic vortices, a so-called Skyrmion lattice, may exist as a ground state in a large number of

materials. It should exist at surfaces and in thin films, as well as in bulk compounds, where a sufficiently large DMI provides chiral interactions. Indeed, three years later in 2009 S. Mühlbauer *et al.* observed the spontaneous formation of such a system in MnSi as one phase of the magnetic phase diagram for MnSi. They found a two-dimensional lattice of Skyrmion lines using neutron scattering [5]. Shortly after, two-dimensional magnetic Skyrmion lattices have also been observed using Lorentz transmission electron microscopy [6] and spin-polarized scanning tunnelling microscopy [7]. Those lattices of Skyrmions are called Skyrmion crystals, or the SkX phase of a helimagnet [6].

In addition to being intriguing structures for fundamental study, magnetic Skyrmions have emerged as promising candidates for technical applications, particularly in advanced magnetic storage devices. A substantial realization of such a storage device is the racetrack memory, which was originally proposed for magnetic domain walls by Parkin et al. [8]. Domain walls are magnetic structures found in both ferromagnetic [9] and antiferromagnetic [10] systems. These stable magnetic entities can be manipulated by external forces, such as electric currents with current densities of $j \sim 10^{11} A/m^2$ [11] (for ferromagnets, see Ref. [12]; for antiferromagnets, see Ref. [13]) and spin waves (for ferromagnets, see Ref. [14]; for antiferromagnets, see Refs. [15, 16]), which makes domain walls suitable candidates for magnetic storage devices. However, magnetic Skyrmions have emerged as a more popular solution. Their smaller size, which lies in the nanometer scale [17–19], and a significantly lower threshold current for motion, being in the order of $j \sim 10^6 A/m^2$ for ferromagnetic Skyrmions [20], make them the preferred option. A notable drawback of using ferromagnetic Skyrmions on a racetrack is that, in general, they do not move in a straight path. Current-driven ferromagnetic Skyrmions move at an angle relative to the applied current direction, a phenomenon known as the Skyrmion Hall effect [21]. In recent years, various methods have been proposed to suppress the Skyrmion Hall effect [22]. These methods include, among others, manipulation of the ferromagnetic racetrack [23, 24], the use of compensated ferrimagnetic Skyrmions [25], and constructing an antiferromagnetic Skyrmion racetrack [26]. The latter is closely related to the topic of this thesis.

Despite providing technical application is not the task of fundamental research, it serves as a boost of motivation. Not at least by this motivation the field of antiferromagnetic Skyrmions became more and more relevant recently. In 2015 (published in 2016), Zhang *et al.* investigated the existence of antiferromagnetic Skyrmions. In Ref. [26], they simulated two opposing domain walls confined within a channel-like geometry leading them horizontally from left to right, and subsequently moved them into a larger, wider area. Through this process, they created a stable antiferromagnetic Skyrmion on a single-layer lattice, similar to the way one would blow a bubble.They found that antiferromagnetic Skyrmions were more stable when colliding with the lattice edges and moved an order of magnitude faster than the typical velocity of current-driven ferromagnetic Skyrmions [26]. In addition they are more robust against external magnetic fields [27]. Thus, antiferromagnetic Skyrmions would provide faster and more stable data storage. Skyrmions in synthetic

antiferromagnets, which are antiferromagnetically coupled multi-layer systems, have been studied theoretically [28] and have even been experimentally realized at room temperature [29]. In contrast, the experimental realization of a single-layer antiferromagnetic Skyrmion crystal remains elusive up to present, although a proposal for such a realization has been suggested theoretically in Ref. [30]. Thus, it is reasonable to conclude that both systems, single-layer antiferromagnetic lattices and synthetic antiferromagnets, exhibits Skyrmions and are intriguing for investigating the dynamics of antiferromagnetic Skyrmions. Here, this thesis sets in, focusing on a detailed examination of these topics.

Magnetic Skyrmions are typically examined as configurations of classical magnetic moments. There are two ways to approach this topic. Originally, Skyrmions were described by treating the magnetization of the material as a continuous vector field, with the magnetic Skyrmion viewed as a topologically protected excitation of that field. Although this is an approximation, it enables the analysis of the system through classical field theory and validates the application of topological principles. The other approach, primarily used for simulations, is to consider a lattice where each site hosts a classical magnetic moment. A lattice is inherently discrete, and we assume a constant distance between these individual sites, resembling the unit cells of the crystal formed by the material. Since both approaches offer distinct advantages, we will utilize both throughout this thesis. Accordingly, we begin Chapter 1 by explaining the fundamentals of classical spin dynamics, including the Landau-Lifshitz-Gilbert equation. Following this introduction, we will focus on the details of the two approaches mentioned previously. For the discrete lattice, we will present the components of the employed lattice Hamiltonian and show the peculiarities of the equations of motion regarding a discrete lattice. For the continuous vector field, we will demonstrate how the Lagrangian formalism can be used to derive the equations of motion. Furthermore, in Chapter 1, we will investigate the properties of an isolated ferromagnetic Skyrmion. This part provides the key concepts and terminology necessary to engage with Skyrmion-related topics. In the final part of Chapter 2, we introduce the treatment of antiferromagnetic systems using classical magnetization fields. We will begin with a universal description of the energy of an antiferromagnetic system based on the framework proposed by Bogdanov *et al.* [31]. Additionally, we will examine two specific models in detail, the antiferromagnetic single-layer square lattice, a so-called G-type antiferromagnet [32], and the bilayer synthetic antiferromagnet, both of which are employed in this thesis.

The focus of this thesis is on driven antiferromagnetic Skyrmions. In Chapter 3, we investigate the underlying mechanisms of an antiferromagnetic Skyrmion in motion. We will demonstrate that an antiferromagnetic Skyrmion can be effectively described as two coupled, rigid ferromagnetic Skyrmions, with a small displacement between them serving as the driving mechanism. We employ Thiele's approximation to derive a formalism that incorporates this mechanism. Following this, we conduct a more detailed analysis to provide a deeper understanding of the external and internal forces acting on a driven

antiferromagnetic Skyrmion. We then apply our formalism to the frequently studied scenario of current-driven antiferromagnetic Skyrmions as a representative example. In this context, we investigate two different scenarios for the application of the driving electric current and validate our results through simulation.

As an additional possibility for driving antiferromagnetic Skyrmions, we investigate in Chapter 4 whether and how spin waves can move antiferromagnetic Skyrmions. Given that it is well established that ferromagnetic Skyrmions can be moved via spin waves, we aim to study the interaction between spin waves and Skyrmions in an antiferromagnetic lattice. To this end, we derive a classical spin wave formalism tailored to a single-layer antiferromagnetic square lattice, which we choose as our model. By linearizing the equations of motion we identify the two commonly known symmetric spin wave modes that an antiferromagnet exhibits. Furthermore, we characterize another type of antiferromagnetic spin wave resulting from an equal superposition of the spin waves from both modes. All findings are verified through simulations. Subsequently, we simulate the interaction between spin waves and Skyrmions by injecting the spin waves into the lattice through edge field manipulation, allowing them to interact with the Skyrmion. We observe different types of Skyrmion motion in response to various types of injected spin waves and demonstrate that the Skyrmion motion depends on the properties of the injected spin wave, such as the wave number. Furthermore, we compare the analytical description of the spin waves with the simulated outcomes of its interaction with the Skyrmion, which allows us to draw conclusions between the analytically derived spin wave properties and the Skyrmion motion induced by those spin waves. Finally, we employ the insights obtained from the formalism derived in Chapter 3. This enables us to enhance our understanding of the mechanics governing spin wave-driven Skyrmions in an antiferromagnetic lattice based on the ferromagnetic case.

2. Theoretical background

2.1. Time evolution of magnetization fields

In the the focus of this thesis are the dynamics of magnetic Skyrmions. A magnetic Skyrmion is a localized, topologically protected structure of the magnetization in a material, similar to a topological knot [5]. Due to it localization and its (meta-) stability it is also viewed as a quasi-particle. In order to study those and their dynamics, it is crucial to model the magnetization and its time behavior in an analytical way. In reality the system in which the scenarios we study take place are magnetic materials formed as a crystalline structure of atoms. The materials are mostly compounds of more than one element, e.g. MnSi which is, as a helical magnet [33], known to host magnetic Skyrmions [5]. The atoms in the material form periodically repeating unit cells and thus defining, depending on their orientation, a crystal lattice with a net magnetization of each unit cell of the lattice. Since the size of a Skyrmion is typically in the nanometer scale [34, 35], we consider this length scale as the typical order of magnitude in this thesis, and hence we are operating within the topic of micromagnetics. On those length scales the magnetization varies very slowly so that we can assume the magnetization to be a continuous field of vectors with a constant length [36]. Following Landau and Lifshitz, in Ref. [36], the motion of the magnetization must conserve the magnetization length $|\boldsymbol{M}|$ and is a precession,

$$\frac{\partial \boldsymbol{M}}{\partial t} = \boldsymbol{\Omega} \times \boldsymbol{M}, \tag{2.1}$$

where $\boldsymbol{\Omega}$ is the vector of the angular velocity of said precession. Furthermore, they conclude that the equilibrium distribution should minimize the free energy F, which depends on the aforementioned continuous vector field. The variation of this energy can be written as

$$\delta F = \int \boldsymbol{H}_{\text{eff}} \cdot \delta \boldsymbol{M} dV, \tag{2.2}$$

where $\boldsymbol{M}$ is the magnetization and $\boldsymbol{H}_{\text{eff}}$ is the "effective magnetic field" representing the environment acting on the magnetization. This is in analogy to a magnetic moment in an external magnetic field. From these considerations they conclude the famous Landau-Lifhsitz equation (LL)

$$\frac{\partial \boldsymbol{M}}{\partial t} = -\gamma \boldsymbol{M} \times \boldsymbol{H}_{\text{eff}}, \tag{2.3}$$

with the gyromagnetic ratio $\gamma = \frac{g|e|}{2mc}$ and the effective field $\boldsymbol{H}_{\text{eff}} = -\partial F/\partial \boldsymbol{M}$. The original work, which is of course more detailed, can be found in Ref. [36]. One should note that the original work did not consider the Dzyaloshinskii-Moriya interaction[1], but the exchange interaction, the interaction with an external magnetic field, and the uniaxial crystal anisotropy. However, the equation of motion is still valid when considering Dzyaloshinskii-Moriya interaction (details will be shown later). The Landau-Lifhsitz equation describes a magnetic moment which precises around a magnetic field. To also describe the realistic case of damping in the time evolution of a magnetic moment, a phenomenological damping term was added so that the precession eventually aligns with the effective field. To model this we use an equation which is the Landau-Lifshitz equation modified by Gilbert in 1955 [38] so that it became the equation of motion of a damped magnetic moment; the Landau-Lifshitz-Gilbert equation (LLG)

$$\frac{\partial \boldsymbol{M}}{\partial t} = -\gamma \boldsymbol{M} \times \boldsymbol{H}_{\text{eff}} + \frac{\alpha}{M} \boldsymbol{M} \times \frac{\partial \boldsymbol{M}}{\partial t}, \tag{2.4}$$

with the phenomenological damping parameter α. Throughout this thesis, we follow the convention that we only consider the direction of the magnetization field. Concretely, this means that we absorb the units of the magnetization vector field $\boldsymbol{M}$ into the model parameters and consider the unit-less vector field $\boldsymbol{n} = \boldsymbol{M}/|\boldsymbol{M}|$ indicating the direction of the magnetization, so that $|\boldsymbol{n}| = 1$. Since we assume the magnetization to be (approximately) constant over the regarded area, this convention is valid and the LLG reads

$$\frac{\partial \boldsymbol{n}}{\partial t} = -\gamma \boldsymbol{n} \times \boldsymbol{H}_{\text{eff}} + \alpha \boldsymbol{n} \times \frac{\partial \boldsymbol{n}}{\partial t}. \tag{2.5}$$

Note that the calculation of the effective field $\boldsymbol{H}_{\text{eff}}$ also changes when considering the dimensionless $\boldsymbol{n}$ instead of the magnetization. The explicit calculation of the effective field depends on whether one considers a discrete lattice (details in Sec. 2.2) or a continuous vector field (details in Sec. 2.3). Since in this work both models are used, the explicit form of the effective field is shown in the respective sections.

It is possible to apply an external driving to the magnetic structure by inducing an electric current into the material. In the following we will briefly explain this topic by closely following Tatara *et al.* [39]. The magnetic structure is given by the magnetic moment of localized spins. When a spin polarized electric current is applied, it means that itinerant electrons travel along the conduction band in current direction and interact with the localized electrons via s-d exchange coupling. Because the magnetic structure, i.e., the localized spins, vary, the conducting electrons align their spin with the localized spins. Due to angular momentum conservation they apply a torque onto the localized spins. This is sketched in Fig. 2.1. In this thesis, we consider, among others, current driven magnetic Skyrmions. To this end we use an adapted LLG equation. The model used in

[1] This interaction was not yet discovered. It was firstly described by Dzyaloshinskii in 1958 [37].

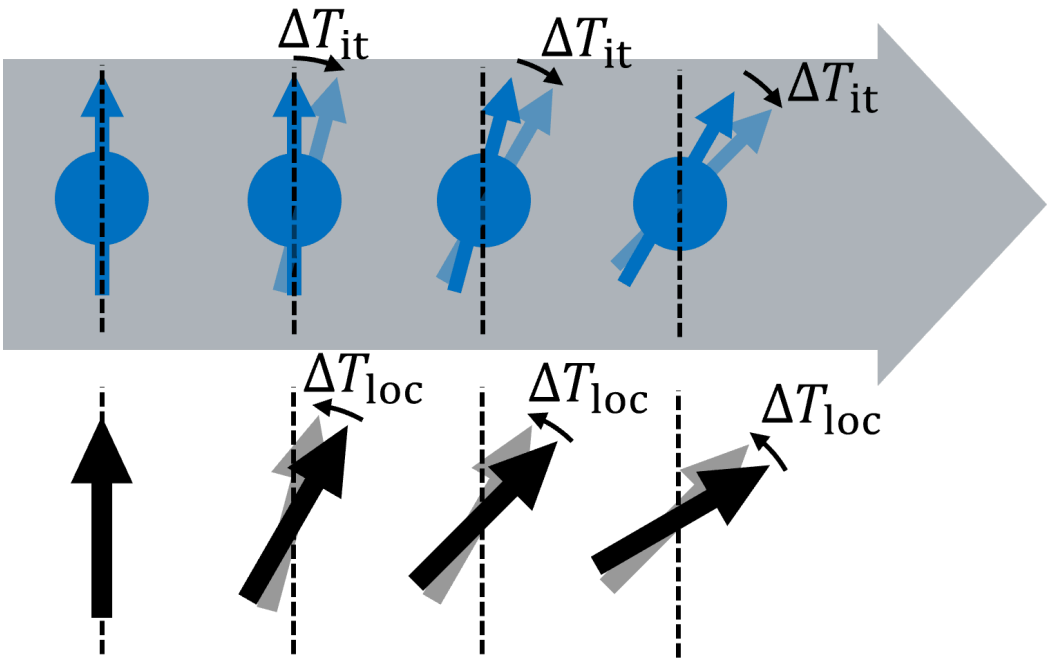

Figure 2.1.: Sketch of how a spin polarized electric current induces a torque onto a magnetic structure. The black arrows in the lower part represent the magnetic moments of the structure while the blue objects above represent the traveling electrons with their spin. The electron flow is, indicated by the grey arrow, from left to right. Initially, the electrons are spin polarized in z direction, but align with the magnetic structure over their course. This leads, due to angular momentum conservation, to a torque acting on the magnetic structure. The sketch is inspired by Ref. [40].

this work was originally derived in the period of time where current driven domain walls were intensively studied. In 1978 Berger stated that "domain walls are too thick to scatter electrons appreciably" [12]. Instead, the electrons travel along the wall and apply a torque to the magnetic moments. With a sufficiently smooth magnetic structure one could imagine that itinerant, spin polarized electrons travel along the domain wall structure and apply a torque in the way as explained above. The torque is called spin transfer torque (STT) after Slonczewski [41]. Due to this the adapted LLG is sometimes also called the Landau–Lifshitz–Gilbert–Slonczewski equation. To precise it further for the case of domain walls, in 2004 Thiaville *et al.* studied the effect of a spin-polarized current crossing a domain wall [42]. They support their micromagnetic simulations by a one-dimensional model of wall dynamics. They added the spin transfer torque in the adiabatic limit to the LLG, so that the equation of motion became [see 42]

$$\frac{\partial \boldsymbol{m}}{\partial t} = -\gamma_0 \boldsymbol{m} \times \boldsymbol{H}_{\mathrm{eff}} + \alpha \boldsymbol{m} \times \frac{\partial \boldsymbol{m}}{\partial t} - u \frac{\partial \boldsymbol{m}}{\partial x}. \tag{2.6}$$

Shortly after, Zhang and Li [43] and Thiaville [44] introduced an additional torque term which arises from spin relaxation of conduction electrons. After Thiaville this term is

called the β term and the final equation of motion is proposed from Ref. [44] to be

$$\frac{\partial \boldsymbol{m}}{\partial t} = -\gamma_0 \boldsymbol{m} \times \boldsymbol{H}_{\text{eff}} + \alpha \boldsymbol{m} \times \frac{\partial \boldsymbol{m}}{\partial t} - (\boldsymbol{u} \cdot \boldsymbol{\nabla})\boldsymbol{m} + \beta \boldsymbol{m} \times [(\boldsymbol{u} \cdot \boldsymbol{\nabla})\boldsymbol{m}]\,. \tag{2.7}$$

From the publication of Eq. (2.7) until today the spin transfer torque was studied intensively. A brief historic overview can be found in Ref. [39]. The equation of motion including spin polarized current used in this dissertation is based on Ref. [45]. In those works the authors considered two torques. One of them is

$$\boldsymbol{T}_{\text{ad}} = (\boldsymbol{v}_s \cdot \boldsymbol{\nabla})\,\boldsymbol{n} \tag{2.8}$$

and is called the adiabatic torque. The other torque

$$\boldsymbol{T}_{\text{non-ad}} = \beta \boldsymbol{n} \times (\boldsymbol{v}_s \cdot \boldsymbol{\nabla})\,\boldsymbol{n}, \tag{2.9}$$

is, in contrast to the adiabatic torque, sometimes referred to as non-adiabatic torque [46]. The parameter β is the non-adiabatic parameter [45, 46]. Equations (2.8) and (2.9) have the advantage that they directly include the "renormalized" spin-transfer velocity [47]

$$\boldsymbol{v}_s = \frac{pd^3}{2e}\boldsymbol{I}_c \tag{2.10}$$

a spin polarized current flowing in the magnetic plane produces. The polarization of the current is given by p while d is the lattice constant and $\boldsymbol{I}_c$ is the current density and direction. In the following discussion, when we refer to spin-polarized current, we specifically mean the renormalized spin-transfer velocity. To highlight that the torque is induced by a current, in the course of this work, we use the symbol $\boldsymbol{j}$ rather than $\boldsymbol{v}_s$. To summarize, in this work the equation

$$\frac{\partial \boldsymbol{n}}{\partial t} = -\gamma \boldsymbol{n} \times \boldsymbol{H}_{\text{eff}} + \alpha \boldsymbol{n} \times \frac{\partial \boldsymbol{n}}{\partial t} + (\boldsymbol{j} \cdot \boldsymbol{\nabla})\,\boldsymbol{n} - \beta \boldsymbol{n} \times [(\boldsymbol{j} \cdot \boldsymbol{\nabla})\,\boldsymbol{n}] \tag{2.11}$$

is used when an applied electric current is considered. For numerical simulations (see Appendix A) it is convenient to use the explicit equation for the time derivative of the vector field, obtained from Eq. (2.11), which is

$$\begin{aligned}\frac{\partial \boldsymbol{n}}{\partial t} = \frac{1}{1+\alpha^2}\big[&-\gamma \boldsymbol{n} \times \boldsymbol{H}_{\text{eff}} - \alpha\gamma \boldsymbol{n} \times (\boldsymbol{n} \times \boldsymbol{H}_{\text{eff}}) + (1+\alpha\beta)\,(\boldsymbol{j} \cdot \boldsymbol{\nabla})\,\boldsymbol{n} \\ &+ (\alpha - \beta)\beta \boldsymbol{n} \times [(\boldsymbol{j} \cdot \boldsymbol{\nabla})\,\boldsymbol{n}]\big].\end{aligned} \tag{2.12}$$

The torque arising from the spin polarized current can move magnetic structures. The current-induced motion of ferromagnetic domain walls, for example, can be derived analytically from the aforementioned equation of motion [39] and has been observed experimentally [48, 49]. Likewise, Skyrmions can also be moved by this current. An often used tool to analytically describe the motion of a ferromagnetic Skyrmion, induced by a spin

polarized current, is the so-called Thiele equation. In 1972 A. A. Thiele derived an equation of forces to govern the steady-state motion of magnetic bubble domains [50]. Thiele used the approximation that the magnetic domain is rigid and only the position of the domain is time dependent, i.e. $\boldsymbol{M}_i = \boldsymbol{M}_i(\boldsymbol{x}_j - \boldsymbol{v}_j t)$. With only that (hard) approximation it was possible for Thiele to form the equation of motion for a continuous vector field into an equilibrium equation of forces

$$\boldsymbol{G} \times \boldsymbol{v} + \alpha \mathcal{D} \boldsymbol{v} + \boldsymbol{F}_{\text{extern}} = 0, \tag{2.13}$$

regarding the magnetic structure as a quasi-particle. Here, the velocity of the structure is $\boldsymbol{v}$, with the total gyrocoupling vector $\boldsymbol{G}$, the dissipation dyadic $\mathcal{D}$, and an externally applied force $\boldsymbol{F}_{\text{extern}}$. Since the dynamics of antiferromagnetic Skyrmions by sublattice displacement is based on the Thiele equation, a detailed description can be found in Chapter 3 and in Ref. [51]. Applying Thiele to the case of ferromagnetic Skyrmions leads to the insight, that the Skyrmion will not flow parallel to the current direction [21, 52], exhibiting the so-called *Skyrmion Hall effect* (SHE). This effect was also found in experiments [53]. Depending on the parameters α and β, the Skyrmion will move at an angle relative to the current direction, known as the Skyrmion Hall angle. However, if both parameters are equal, $\alpha = \beta$, the Skyrmion Hall angle vanishes and the Skyrmion moves parallel to the current direction [45]. The Thiele equation, among others, show how convenient it is to describe the magnetization as continuous vector field. In some cases, however, we want to explicitly take lattice effects into account. To do so it is necessary to consider the model of a discrete lattice as described below.

2.2. Hamiltonian and equation of motion

The original Landau-Lifshitz-Gilbert equation was, as described in the previous section, found and studied regarding the magnetization as a continuous vector field [36]. However, it is possible to derive a similar equation of motion for a discrete lattice where each site hosts a magnetic moment. Since in this thesis both, continuous vector field and discrete lattice, were studied and compared to each other, the equations of motion of both will be derived in this chapter. In this section the discrete lattice is considered while the next section will explain the equations of motion of the continuous vector field.

We consider a crystal of periodically arranged sources of the magnetic moments, or spins $\boldsymbol{S}$, and call it therefore a lattice. The total energy of the system is given by the lattice Hamiltonian

$$H = -\frac{J}{2} \sum_{\langle i,j \rangle} \boldsymbol{S}_i \cdot \boldsymbol{S}_j - \sum_{\langle i,j \rangle} \boldsymbol{D}_{ij} \cdot (\boldsymbol{S}_i \times \boldsymbol{S}_j) - \sum_i \boldsymbol{B}_0 \cdot \boldsymbol{S}_i - K \sum_i (S_i^z)^2 , \tag{2.14}$$

where the $\boldsymbol{S}_i$ are classical magnetic moments represented by a three-dimensional vector. The magnetic moments can represent, depending on the model, the net magnetization of a unit cell in a magnetic crystal, or even the magnetization of a localized spin in a lattice. For the latter assumption, it is possible to handle the system quantum mechanically (except for the last term, the anisotropy term). In recent studies, e.g., Ref. [54], the lattice spins are regarded as purely quantum mechanical in order to examine so-called "quantum skyrmions". In this thesis, however, we assume the magnetic moments as the classical net magnetization of the respective lattice site. Thus, those are handled as expectation values of quantum mechanical spins $\boldsymbol{S}_i = \langle \hat{\boldsymbol{s}}_i \rangle$. Nevertheless, for the following calculations we temporary stray beyond the classical spin model and neglect the fact that $\boldsymbol{S}_i$ is only the expectation value. By this we show that the equation of motion can be derived from the quantum mechanical behavior of spins. The time derivative of a quantum mechanical operator can be calculated by the Ehrenfest theorem [55]. Therefore, we assume that the equation of motion for a (not explicitly time dependent) quantum magnetic moment on a given site k is given by

$$i\hbar \frac{d}{dt} \langle \boldsymbol{S}_k \rangle = \langle [H, \boldsymbol{S}_k] \rangle \,, \tag{2.15}$$

where the square brackets denote the commutator and the vector characteristic of $\boldsymbol{S}_k$ implies that all three components fulfill this equation simultaneously.

Heisenberg exchange interaction

The first term in the Hamiltonian, $-\frac{J}{2} \sum_{\langle i,j \rangle} \boldsymbol{S}_i \cdot \boldsymbol{S}_j$, is the Heisenberg exchange interaction. It roots in the quantum mechanical principle that particles are indistinguishable. It was discovered by Heisenberg [56] and Dirac [57] independently. Later, Heisenberg applied this method to explain the ferromagnetic phenomena with exchange interaction [58]. In this thesis, as well as in most models regarding classical magnetic spins, the exchange interaction is the leading energy of the magnetic system. The sum $\sum_{\langle i,j \rangle} \boldsymbol{S}_i \cdot \boldsymbol{S}_j$ goes over each pair of nearest neighbors. It is more convenient to re-write the sum so that we focus on each lattice site i and its neighbors. Concretely, we (globally) sum over each lattice site i and starting from this site we (locally) sum over each neighbor r, so that the sum is in summary $\sum_{\langle i,j \rangle} \boldsymbol{S}_i \cdot \boldsymbol{S}_j \; = \sum_i \sum_r \boldsymbol{S}_i \cdot \boldsymbol{S}_{i+r}$. By this, the commutator amounts to

$$\left[-\frac{J}{2} \sum_{i,r} \hat{\boldsymbol{s}}_i \cdot \hat{\boldsymbol{s}}_{i+r}, \hat{\boldsymbol{s}}_k \right] = \frac{i\hbar J}{2} \sum_r \left(\hat{\boldsymbol{s}}_{k+r} \times \hat{\boldsymbol{s}}_k - \hat{\boldsymbol{s}}_k \times \hat{\boldsymbol{s}}_{k+r} \right) , \tag{2.16}$$

where we considered quantum mechanical spin operator $\hat{\boldsymbol{s}}$ on a symmetric lattice and outsourced the explicit calculations into the Appendix C. It turns out that the commutator results in a cross product of the spin at the regarded site k with each of its neighbors. In the classical approximation we assume that each single spin operator can be expressed by its expectation value. Since the magnetic moments $\boldsymbol{S}_i$ are then the expectation values of the quantum mechanical operators and thus real valued vectors, they commute. Consequently,

we can summarize Eq. (2.16) to

$$\langle \left[-\frac{J}{2} \sum_{i,r} \boldsymbol{S}_i \cdot \boldsymbol{S}_{i+r}, \boldsymbol{S}_k \right] \rangle \to -i\hbar J \sum_r \left(\boldsymbol{S}_k \times \boldsymbol{S}_{k+r} \right). \tag{2.17}$$

For an easier interpretation one can write the non-constant part as $\boldsymbol{S}_k \times (\sum_r \boldsymbol{S}_{k+r})$. By this, we directly see that it is a cross product of the moment at site k with the sum of all its neighbors. As a side note, considering very small distances between the lattice sites one can show that the sum of all neighbors approximate to $\boldsymbol{\nabla}^2 \boldsymbol{S}_k$ with a prefactor depending on the lattice geometry. This will be shown for the square lattice below in Sec. 2.5 and in Ref. [59] it is shown in detail for different types of cubic lattices.

Dzyaloshinskii-Moriya interaction

The second term in Eq. (2.14) is the Dzyaloshinskii-Moriya interaction (DMI). It is an anti-symmetric exchange interaction and was not known until the 1950s. Before the introduction of this interaction it was an open question that some antiferromagnetic crystals, such as $\alpha-Fe_2O_3$ or $MnCO_3$, proposed weak ferromagnetism [37]. In 1957 I. Dzyaloshinskii introduced a phenomenological term $\boldsymbol{D} \cdot [\boldsymbol{S}_i \times \boldsymbol{S}_j]$ based on the crystal symmetry of the regarded material [37]. He showed that due to this term some parameter configurations energetically favors the canted spin arrangement rather than the antiferromagnetic one. This leads to the weak ferromagnetism. Later in 1960 T. Moriya advanced the phenomenological theory of Dzyaloshinskii by concretely considering spin orbit interaction [60]. Furthermore, he proposed five rules for which crystal symmetry leads to which explicit formulation of the DM interaction. These rules can be found in Ref. [60]. In this thesis we only consider two types of DMI. One is the so-called *bulk* DMI which is present in the bulk of a magnetic material. One example exhibiting this kind of DMI in the bulk is MnSi or FeGe [33]. The other here considered type of DMI is the *interfacial* DMI. As the name suggests this interaction is present at the surface of the magnetic material or in the area between two different materials. It is due to the broken symmetry at the surface and can be found in, for instance, thin magnetic multilayers [61]. In the analytical calculations in this thesis, however, we consider the anti-symmetric tensor $\boldsymbol{D}_{ij} = -\boldsymbol{D}_{ji}$ in general and use the explicit expression only when it is necessary. Regarding the commutator with spin $\hat{\boldsymbol{s}}_k$ it is, again, convenient to separate the sum over $\langle i, j \rangle$ to the global sum over i and the local sum over its neighbors r. The commutator relation regarding the DMI term of the Hamiltonian is, thus,

$$\begin{aligned} \left[\sum_{i,r} \boldsymbol{D}_{i,i+r} \cdot \left(\boldsymbol{S}_i \times \boldsymbol{S}_{i+r} \right), \boldsymbol{S}_k \right] = & -i\hbar \sum_r \left(\boldsymbol{S}_{k+r} \times \boldsymbol{D}_{k,k+r} \right) \times \boldsymbol{S}_k \\ & + i\hbar \sum_r \boldsymbol{S}_k \times \left(\boldsymbol{S}_{k+r} \times \boldsymbol{D}_{k,k+r} \right). \end{aligned} \tag{2.18}$$

The detailed calculation can be found in the Appendix C. Since we are, in this thesis, interested in the classical magnetic moments, we, again, regard only the expectation values of the spin operators. By this, we assume $\boldsymbol{S}$ to be a classical magnetic moment and thus a three dimensional vector. Consequently, one can commute the spins in such a way that Eq. (2.18) simplifies to

$$\left\langle \left[\sum_{i,r} \boldsymbol{D}_{i,i+r} \cdot \left(\boldsymbol{S}_i \times \boldsymbol{S}_{i+r} \right), \boldsymbol{S}_k \right] \right\rangle \rightarrow 2i\hbar \sum_r \boldsymbol{S}_k \times \left(\boldsymbol{S}_{k+r} \times \boldsymbol{D}_{k,k+r} \right). \tag{2.19}$$

This can be seen in the same way as the commutator with the exchange interaction previously. By re-writing the magnetic term to $\boldsymbol{S}_k \times \sum_r \left(\boldsymbol{S}_{k+r} \times \boldsymbol{D}_{k,k+r} \right)$ it is clearly visible that this resembles the cross product of the considered spin $\boldsymbol{S}_k$ with an effective field regarding each of its neighbors.

Other terms

The last two terms of Eq. (2.14) are the Zeeman term $\sum_i \boldsymbol{B}_0 \cdot \boldsymbol{S}_i$ and the anisotropy term $K \sum_i \left(S_i^z \right)^2$. Both terms are on-site interactions. The Zeeman energy models the coupling of the magnetic moment of a spin to an external magnetic field and the commutation

$$\left[\sum_j \boldsymbol{B_0} \cdot \hat{\boldsymbol{s}}_j, \hat{\boldsymbol{s}}_k \right] = \sum_{j,a,b} B_0^a \left[\hat{s}_j^a, \hat{s}_k^b \right] \boldsymbol{e}_b \tag{2.20}$$

is essentially the commutation relation of two spin operators. Using the commutation relation $\left[\hat{s}_j^a, \hat{s}_k^b \right] = i\hbar \delta_{jk} \epsilon_{abc} \hat{s}_j^c$ yields for Eq. (2.20)

$$\left[\sum_j \boldsymbol{B_0} \cdot \hat{\boldsymbol{s}}_j, \hat{\boldsymbol{s}}_k \right] = i\hbar \hat{\boldsymbol{s}}_k \times \boldsymbol{B}_0. \tag{2.21}$$

One can immediately see that the quantum mechanical commutator resembles the classical assumption that a magnetic moment precesses (connected to the cross product) around an external magnetic field. The anisotropy term stems from the crystal symmetry in the material and is included here as a phenomenological term. It is thus considered here purely classical and will be explained more detailed below in Sec. 2.3. We include it in the lattice Hamiltonian by transforming it to the lattice term $K \sum_i \left(S_i^z \right)^2$.

Lattice equation of motion

Finally, we can summarize the previously derived equations in order to get the commutator of the lattice Hamiltonian from Eq. (2.14) with the spin $\boldsymbol{S}_k$. Regarding the lattice spins as quantum mechanical spin operators was only to show that the classical equation of motion can be inferred from quantum mechanical behavior. All topics in this thesis consider

classical magnetic moments, so that we can identify the lattice spins as expectation values and, thus, express them simply as three dimensional real valued vectors. The expectation value of the commutator can then be expressed as

$$\langle [H, \boldsymbol{S}_k] \rangle \to -i\hbar \boldsymbol{S}_k \times \left(J \sum_r \boldsymbol{S}_{k+r} + 2 \sum_r \boldsymbol{S}_{k+r} \times \boldsymbol{D}_{k,k+r} + \boldsymbol{B}_0 + 2K S_k^z \boldsymbol{e}_z \right), \tag{2.22}$$

where the last term was not derived from the lattice but from the continuous vector field equation of motion (see below) and adapted to the lattice. Comparing the commutator from Eq. (2.22) to the Ehrenfest theorem, Eq. (2.15), the time derivative of the (classical) spin at a given lattice site k can be described by

$$\partial_t \boldsymbol{S}_k = -\gamma \boldsymbol{S}_k \times \boldsymbol{H}_k^{\text{eff}}, \tag{2.23}$$

which looks identical to the Landau-Lifshitz equation. The effective field acting on a lattice site k can be calculated by

$$\boldsymbol{H}_k^{\text{eff}} = -\frac{1}{\gamma\hbar} \frac{\partial H}{\partial \boldsymbol{S}_k}. \tag{2.24}$$

In the calculations in this thesis we set $\hbar = 1$. Furthermore, we assume the same magnetization intensity on each lattice site, meaning we assume the magnetic moments on each site to have the same length $|\boldsymbol{S}_i| = |\boldsymbol{S}_j|$. It is, therefore, a usual method to absorb the magnetization units into the Hamilton parameter and solely focus on a normalized vector $\boldsymbol{n}_i = \boldsymbol{S}_i/|\boldsymbol{S}_i|$ on each lattice site. Using these assumptions, as well as a phenomenological damping term as in the Landau-Lifshitz-Gilbert equation, the magnetic equation of motion for the discrete lattice used in this thesis finally reads

$$\partial_t \boldsymbol{n}_i = -\gamma \boldsymbol{n}_i \times \boldsymbol{H}_i^{\text{eff}} + \alpha \boldsymbol{n}_i \times \partial_t \boldsymbol{n}_i. \tag{2.25}$$

This is the equation we use to describe how the magnetic moment on a single lattice site evolves in time based on the Hamiltonian and the damping. It is the crucial equation on which the spin wave theory in Chapter 4 and all numerical simulations (see Appendix A) in this thesis are based on.

2.3. Lagrange formalism

It is possible to derive the Landau-Lifshitz-Gilbert equation from the Lagrange formalism. Using the Euler-Lagrange equations instead of a phenomenological ansatz is more reliable. Furthermore, it enables us to derive the correct equation of motion for the considered model and compare it to experimental results. In order to derive the equations of motion by the Lagrange formalism, we closely follow Tatara, Kohno and Shibata [39]. The action is defined by the direction of the magnetization. As explained in the previous section we assume the magnetization to be smooth and of approximately the same intensity over the

whole area. It can, thus, be described by the unit vector field $\boldsymbol{n}$. The action in the sense of the Lagrange formalism is given by

$$\mathcal{S} = \int L(\boldsymbol{n}, \dot{\boldsymbol{n}}) \mathrm{d}t. \tag{2.26}$$

It is convenient to separate the Lagrangian into a dynamic and a static part $L = \mathcal{L}_{\mathrm{dyn}} + \mathcal{L}_{\mathrm{stat}}$, where the latter is the energy density $\mathcal{H}$ and the former is given by the Berry phase [62, 63]

$$\mathcal{L}_{\mathrm{dyn}} = -\frac{\hbar}{d^2} \boldsymbol{A}(\boldsymbol{n}) \partial_t \boldsymbol{n}. \tag{2.27}$$

Note that since we here consider a two-dimensional space, the area of the magnetic unit cell is considered in the term d^2 which is the square of the lattice constant. $\boldsymbol{A}$ is a gauge field resembling the gyroscopic structure of the spin dynamics. It is closely connected to the Berry phase and detailed derivations of these phase are widely found, e.g., in Refs. [62–64]. The lattice constant d is the typical spatial distance between two magnetic moments [62]. Under an infinitesimal variation $\boldsymbol{n} \to \boldsymbol{n} + \delta\boldsymbol{n}$ Eq. (2.26) leads to

$$\delta\mathcal{S} = \int \left(\frac{\mathrm{d}}{\mathrm{d}t} \frac{\partial L}{\partial \dot{\boldsymbol{n}}} - \frac{\partial L}{\partial \boldsymbol{n}} \right) \cdot \delta\boldsymbol{n} \, \mathrm{d}t. \tag{2.28}$$

The infinitesimal variation is perpendicular to the vector field, $\delta\boldsymbol{n} \perp \boldsymbol{n}$, so that it can be expressed as $\delta\boldsymbol{n} = \boldsymbol{n} \times \delta\boldsymbol{w}$. Thus, the vector field has to fulfill

$$\left(\frac{\mathrm{d}}{\mathrm{d}t} \frac{\partial L}{\partial \dot{\boldsymbol{n}}} - \frac{\partial L}{\partial \boldsymbol{n}} \right) \times \boldsymbol{n} = 0. \tag{2.29}$$

Regarding only the dynamical Lagrange, this resembles

$$\frac{\mathrm{d}}{\mathrm{d}t} \frac{\partial \mathcal{L}_{\mathrm{dyn}}}{\partial \dot{\boldsymbol{n}}} - \frac{\partial \mathcal{L}_{\mathrm{dyn}}}{\partial \boldsymbol{n}} = \frac{\hbar}{d^2} \left(\dot{\boldsymbol{n}} \times \boldsymbol{n} \right). \tag{2.30}$$

We refer to Ref. [39] for more details regarding the spin angles θ and ϕ, or to Ref. [64] for a quantum-classical derivation using vectors. The static part is simply the energy density $\mathcal{H}$. Thus, Eq. (2.29) becomes

$$\left(\frac{\hbar}{d^2} \left(\dot{\boldsymbol{n}} \times \boldsymbol{n} \right) - \frac{\partial \mathcal{H}}{\partial \boldsymbol{n}} \right) \times \boldsymbol{n} = 0. \tag{2.31}$$

Using the fact that $\dot{\boldsymbol{n}} \perp \boldsymbol{n}$ as well as $|\boldsymbol{n}|^2 = 1$ Eq. (2.31) leads to the equation of motion

$$\dot{\boldsymbol{n}} = \boldsymbol{n} \times \frac{d^2}{\hbar} \frac{\partial \mathcal{H}}{\partial \boldsymbol{n}}, \tag{2.32}$$

which resembles the non-damped Landau-Lifshitz-Gilbert equation, Eq. (2.5), where the effective field is $\boldsymbol{H}_{\mathrm{eff}} = -\frac{d^2}{\gamma\hbar} \frac{\partial \mathcal{H}}{\partial \boldsymbol{n}}$. Treating the damping can be done using the Rayleigh

method [39], which means we include a dissipation function

$$W = \frac{\alpha}{2d^2}\hbar\dot{\boldsymbol{n}}^2 \tag{2.33}$$

to Eq. (2.29), so that it becomes

$$\left(\frac{\mathrm{d}}{\mathrm{d}t}\frac{\partial L}{\partial \dot{\boldsymbol{n}}} - \frac{\partial L}{\partial \boldsymbol{n}} + \frac{\partial W}{\partial \dot{\boldsymbol{n}}}\right) \times \boldsymbol{n} = 0. \tag{2.34}$$

Repeating the same process as for Eq. (2.31), this leads to the Landau-Lifshitz-Gilbert equation, as described in Eq. (2.5) in the previous section. The equation derived from Eq. (2.34) reads

$$\dot{\boldsymbol{n}} = -\gamma \boldsymbol{n} \times \boldsymbol{H}_{\mathrm{eff}} + \alpha \dot{\boldsymbol{n}} \times \boldsymbol{n}, \tag{2.35}$$

with the damping parameter α. The effective magnetic field

$$\boldsymbol{H}_{\mathrm{eff}} = -\frac{d^2}{\gamma\hbar}\frac{\partial \mathcal{H}}{\partial \boldsymbol{n}} \tag{2.36}$$

depends on the spin Hamiltonian $\mathcal{H}_S$ describing the energy density. In the sense of Lagrange this is the static Lagrangian.

This makes the spin Hamiltonian a crucial tool for modeling the considered system. In this thesis the analytical descriptions of the energy follow A. Bogdanov who uses a "standard symmetry analysis" to derive an energy term belonging to different symmetry classes (see, e.g., Refs. [3, 65]). We adapted the energy term so that it models the two dimensional magnetic vector field studied in this thesis. The energy term is

$$\mathcal{H} = \int \left\{ A \sum_j \left(\frac{\partial \boldsymbol{n}}{\partial x_j}\right)^2 + \mathcal{E}_{\mathrm{DMI}} - \boldsymbol{n} \cdot \boldsymbol{B}_0 - K n_z^2 \right\} \mathrm{d}^2\boldsymbol{r}, \tag{2.37}$$

where we consider a two-dimensional model, so that the integral is over the xy plane. The energy depends on the direction of the magnetization $\boldsymbol{n} = \boldsymbol{M}/|\boldsymbol{M}|$ as a vector field and consists of those energy contributions which are typically the most prominent energies in materials hosting Skyrmions. Since the magnetization is assumed to be constant over space, it is sufficient to consider the unit-less vector field $\boldsymbol{n}$. The unit of the magnetization is assumed to be absorbed in the parameters of Eq. (2.37). This is a valid and often used method, see, for example, Ref. [62].

The first energy term $A\sum_j \left(\frac{\partial \boldsymbol{n}}{\partial x_j}\right)^2$ is the exchange energy density. The sum over j means that the derivative of the vector field in x and y direction is considered. In some works the notation $A(\boldsymbol{\nabla}\boldsymbol{n})^2$ is used instead. The parameter A is called the exchange (stiffness) parameter [65] and will be considered as the dominant energy part. The second term, $\mathcal{E}_{\mathrm{DMI}}$ refers to the Dzyaloshinskii-Moriya interaction (DMI). This interaction was intro-

duced by Dzyaloshinskii [37] and was later formulated more precisely by Moriya [60]. Its explicit form and intensity depend on the crystal symmetry created by the atoms in the material. In Ref. [66] this term is called w' and stands for the DMI of different symmetry classes. However, as explained in the previous section, in this dissertation we mainly use two particular forms of DMI - bulk DMI and interfacial DMI. Regarding the magnetic moments forming a continuous vector field, the two respective DMI energy densities are [67, 68][2]

$$\begin{aligned} \mathcal{E}_{\mathrm{DMI}}^{\mathrm{if}} &= D\boldsymbol{n} \cdot (\boldsymbol{e}_z \times \boldsymbol{\nabla}) \times \boldsymbol{n}, \\ \mathcal{E}_{\mathrm{DMI}}^{\mathrm{b}} &= D\boldsymbol{n} \cdot (\boldsymbol{\nabla} \times \boldsymbol{n}), \end{aligned} \tag{2.38}$$

where the DMI parameter D is assumed to be constant. The third term in Eq. (2.37) refers to the Zeeman energy which models the influence of an external magnetic field $\boldsymbol{B}_0$ onto the magnetic system. For ferromagnetic Skyrmion systems the external magnetic field always points in opposite Skyrmion direction (direction of the FM background). Throughout this thesis, however, we will consider antiferromagnetic Skyrmions and assume no external magnetic fields, thus setting this term to zero. Nevertheless, it is a crucial term for ferromagnetic Skyrmions and is therefore noteworthy in the general energy consideration. The fourth term contributing to the energy is the uniaxial anisotropy. In magnetic materials the symmetry of the crystal may lead to energetically favored axes in which the spins align. To model this fact the uniaxial anisotropy was introduced as a phenomenological energy term E_{ani}. In this thesis, we regard the uniaxial anisotropy term of second order in z direction, which is $-Kn_z^2$. Because we consider a model where the energy decreases when the spins align in z direction, we chose $K > 0$ so that it defines the z axis as the easy axis. Choosing $K < 0$ would define the xy plane as easy plane [36]. In principle, there may also be higher order terms of the anisotropy. Furthermore, other axes could be defined as easy axis in order to bring other topological objects, the so-called *Bimerons* into existence [69]. However, this is not in the scope of this work. A more detailed explanation of the crystal anisotropy term can be found in Ref. [70].

Apart from constructing the energy by the parts as mentioned previously, there is another consideration of the energy which is also often used, see, e.g., Refs. [5, 71]. There, the Ginzburg-Landau free energy functional is expanded in powers of the slowly varying magnetization and adapted by the DMI. This functional reads

$$F = \int \mathrm{d}^3 r \left\{ r_0 \boldsymbol{M}^2 + J(\boldsymbol{\nabla}\boldsymbol{M})^2 + 2D\boldsymbol{M} \cdot (\boldsymbol{\nabla} \times \boldsymbol{M}) + U\boldsymbol{M}^4 - \boldsymbol{B}\boldsymbol{M} \right\}, \tag{2.39}$$

where the natural arising expansion terms are weighted by the model parameters. A more deeper explanation including a detailed description of the parameters can be read in Ref. [72]. Despite the different ansatz, the Ginzburg-Landau theory for helimagnets provides structurally the same terms as Eq. (2.37). This being said, as we revisit the topic of the

[2]Note from the author: In Ref. [67] the formula for the interfacial DMI misses a $\times$ sign.

time evolution of the magnetic vector field, we see that the equation of motion, Eq. (2.35), brings the effective field into focus. With the concrete form of the energy of Eq. (2.37), the effective field, Eq. (2.36), is

$$\boldsymbol{H}_{\text{eff}} = \frac{d^2}{\gamma\hbar}\left[2A\boldsymbol{\nabla}^2\boldsymbol{n} - 2D\left(\boldsymbol{\nabla}\times\boldsymbol{n}\right) + \boldsymbol{B}_0 + 2Kn_z\boldsymbol{e}_z\right] \tag{2.40}$$

for the bulk DMI, and,

$$\boldsymbol{H}_{\text{eff}} = \frac{d^2}{\gamma\hbar}\left[2A\boldsymbol{\nabla}^2\boldsymbol{n} - 2D\left(\boldsymbol{e}_z\times\boldsymbol{\nabla}\right)\times\boldsymbol{n} + \boldsymbol{B}_0 + 2Kn_z\boldsymbol{e}_z\right] \tag{2.41}$$

for the interfacial DMI. This resembles the phenomenological LLG, see Eq. (2.5), with an effective field derived from the underlying model. In summary, those are the effective fields we consider when regarding ferromagnetic Skyrmions analytically.

2.4. Skyrmion properties

With the corresponding choice of parameters it is possible with the Hamiltonians of the previous section to form a (meta-) stable magnetic Skyrmion [65]. The existence of magnetic Skyrmions in the here considered system has two main reasons. One is the topological protection, which is the first topic we explain in this section. It determines that a Skyrmion can not be annihilated by a continuous deformation of the vector field. However, since the continuity of the vector field is only an approximation to granular matter, the topological argument may not apply in reality. In this context, the second reason assumes significance. It is the energy of the Skyrmion compared to the energy of the homogeneous ferromagnet. This will be explained in more detail below in this section. The energy of a magnetic Skyrmion suggests that it is at least meta-stable and, for some parameter configurations, even lower in the energy than the ground state [62]. Therefore, and due to the clear localization, the Skyrmion is called a quasi-particle.

Topological protection

The most prominent description of magnetic Skyrmions is that they are topologically protected spin structures. In the following we will explain in detail what this often-stated description implies. For the topological protection we regard the magnetization. It is considered to be a continuous vector field $\boldsymbol{n}(\boldsymbol{r})$ on a two-dimensional plane $\boldsymbol{r} = (x, y)$. The length of the vector field is assumed to be constant of unit length in each position $|\boldsymbol{n}(\boldsymbol{r})|^2 = 1$. Hence, the vector can be described solely by its position on a unit sphere

$$\boldsymbol{n}(\boldsymbol{r}) = \begin{pmatrix} \sin\left[\Theta(\boldsymbol{r})\right]\ \cos\left[\Phi(\boldsymbol{r})\right] \\ \sin\left[\Theta(\boldsymbol{r})\right]\ \sin\left[\Phi(\boldsymbol{r})\right] \\ \cos\left[\Theta(\boldsymbol{r})\right] \end{pmatrix}. \tag{2.42}$$

An example of describing the three dimensional vector, which represents the magnetization by its position on a unit sphere, is visualized in Fig. 2.2 (left). From this viewpoint it can be seen that the angles, describing the position on a sphere, depend on the position in space $\boldsymbol{r}$. Since the vector field lives on a two dimensional plane, it can be viewed as a mapping of each point of a plane to the unit sphere $(x, y) \mapsto (\Theta, \Phi)$. Due to this mapping it is possible to define a topological quantum number

$$Q = \frac{1}{4\pi} \int \boldsymbol{n} \cdot \left(\frac{\partial \boldsymbol{n}}{\partial x} \times \frac{\partial \boldsymbol{n}}{\partial y} \right) \mathrm{d}^2 \boldsymbol{r}, \tag{2.43}$$

which is an integer number $Q \in \mathbb{Z}$ counting how many times the plane wraps around the unit sphere. As an example of this, in Fig. 2.2 (right) the mapping from the sphere to a 2D plane is visualized. The right picture is taken from Ref. [73]. A detailed derivation of the

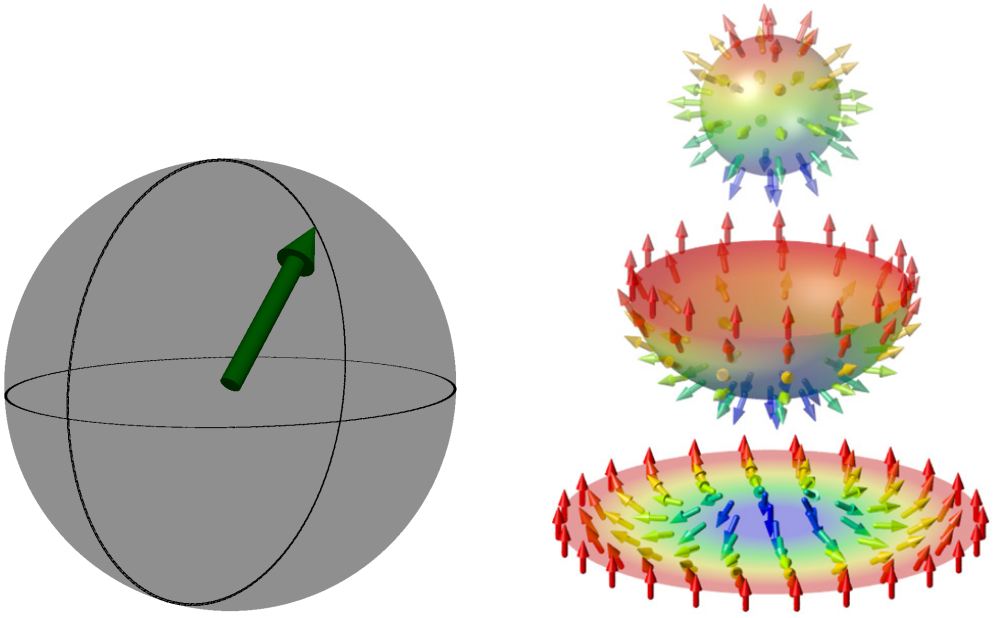

Figure 2.2.: Left: Visualization of how a three-dimensional vector with unit length can be represented by its position on a sphere. Right: Graphical representation of mapping the Skyrmion from a sphere onto a plane. Taken from Ref. [73].

topological quantum number can be found in, e.g., Ref. [74]. In 1975 A. A. Belavin and A. M. Polyakov showed [2] that a ferromagnet with only exchange interaction has a metastable state where the magnetization in the periphery is homogeneous, e.g. $+\boldsymbol{e}_z$, while the center magnetization points in the opposite direction. The existence of that state is argued by the aforementioned wrapping of the plane around the unit sphere. They concluded that due to the topology there is no phase transition between the ground state and this metastable state, despite its high energy of $8\pi Q$ [2]. By this, they predicted an early version of the topological quasi-particle which we know as Skyrmion today. However, Skyrmions are not the only topological objects which can arise in a magnetic system. Before Skyrmions were studied so widely as today, magnetic domain walls [75] and topological bubbles [76] were in the focus as topological objects. Another example of topological objects are Hopfions

[77, 78]. These are three-dimensional topological objects defined by an integer Hopf-index. Hopfions become more and more relevant in the field of study, see e.g. [79–81]. Nevertheless, these are merely examples of other topological objects, serving to illustrate that Skyrmions are not the only such entities. Turning our attention back to magnetic Skyrmions the topological quantum number Q, stemming from the mapping of a plane to a sphere, is calculated by integration as in Eq. (2.43). Therefore, a density can be constructed from this which is called the topological charge density

$$q = q(\boldsymbol{r}) = q(x, y) = \boldsymbol{n} \cdot \left(\frac{\partial \boldsymbol{n}}{\partial x} \times \frac{\partial \boldsymbol{n}}{\partial y} \right). \tag{2.44}$$

Strictly speaking, this density does not have a physical meaning and is simply the expression which is integrated over the whole space in the definition of the topological quantum number. Nevertheless, it is a useful tool for analytical studies about Skyrmions, or topological objects in general. Most commonly it is used to construct a continuity equation. This is a natural choice since the topological quantum number of a Skyrmion is constant, so that $\int \dot{q} \, \mathrm{d}^2\boldsymbol{r} = 0$. Combining the topological charge density q with the Equations of Motion of the vector field $\boldsymbol{n}$ yields the continuity equation $\partial_t q = -\boldsymbol{\nabla} \boldsymbol{j}$. This equation has been used to investigate a variety of results. In Ref. [45] it was used to show that Skyrmions and Anti-Skyrmions are driven in different directions by the Skyrmion Hall effect, while Komineas and Papanicolaou, Ref. [82], studied Skyrmion dynamics based on the concept of the Skyrmion as a topological charge. Despite the topological charge density being an interesting and promising topic, a more detailed study of this concept would be out of the scope of this thesis. Here, only the topological quantum number Q will be of interest and it can be shown by simple calculations that Q can, indeed, only take integer values.

Since the magnetic Skyrmion in its simplest form is radial symmetric, it is convenient to use polar coordinates $(x, y) \to (\rho, \varphi)$ with the Skyrmion center as coordinate origin $\rho = 0$. Revisiting the picture that the vector field can be seen as the position on a unit sphere in Eq. (2.42), the angles θ and Φ now depends on the polar coordinates ρ and φ. Due to the radial symmetry we conclude that the angle Θ only depends on the radial coordinate ρ while the angle Φ only depends on φ. While the form of $\Theta(\rho)$ is known to fulfill

$$\frac{d^2\Theta}{d\rho^2} + \frac{1}{\rho}\frac{d\Theta}{d\rho} - \frac{\sin(\Theta)\cos(\Theta)}{\rho^2} - \frac{K}{A}\sin(\Theta)\cos(\Theta) - \frac{B_0}{2A}\sin(\Theta) = 0 \tag{2.45}$$

(see Ref. [65]), the other angle can be expressed explicitly by $\Phi = m\varphi + \varphi_0$, depending on the vorticity m and the helicity φ_0 [67]. For the calculation of the topological charge we assume a Skyrmion with vorticity $m = \pm 1$. A positive vorticity, $m = 1$, is associated with a Skyrmion while $m = -1$ refers to its "anti-particle", the Anti-Skyrmion [67]. There exists a variety of 2D and 3D topological objects associated with Skyrmions like the Skyrmion lattice, Hopfions, and the Skyrmionium to only name a few [see 74, 83]. In the skyrmionics

community the name "Skyrmion zoo" has been established [84]. Nevertheless, in this thesis we consider only two-dimensional Skyrmions with topological quantum number $Q = \pm 1$. The radial symmetry combined with the use of polar coordinates for the spatial position and spherical coordinates for the vector field components enables us to explicitly calculate the topological quantum number Q from Eq. (2.43). To this end, the operators ∂/∂_x and ∂/∂_y have to be transformed into polar coordinates, too. This is done by

$$\begin{aligned} \frac{\partial \boldsymbol{n}}{\partial x} &= \cos(\varphi)\frac{\partial \boldsymbol{n}}{\partial \rho} - \frac{\sin(\varphi)}{\rho}\frac{\partial \boldsymbol{n}}{\partial \varphi}, \\ \frac{\partial \boldsymbol{n}}{\partial y} &= \sin(\varphi)\frac{\partial \boldsymbol{n}}{\partial \rho} + \frac{\cos(\varphi)}{\rho}\frac{\partial \boldsymbol{n}}{\partial \varphi}\ . \end{aligned} \tag{2.46}$$

Applying these to the topological quantum number in Eq. (2.43), yields

$$Q = \frac{1}{4\pi}\int \boldsymbol{n}\cdot\left(\frac{\partial \boldsymbol{n}}{\partial \rho}\times\frac{\partial \boldsymbol{n}}{\partial \varphi}\right)\ \mathrm{d}\rho\ \mathrm{d}\varphi. \tag{2.47}$$

Here we immediately see that the form of Q does not depend on whether Cartesian or polar coordinates are used (considering that one has to include the Jacobian determinant ρ into the integral when using polar coordinates). From now on we use that Θ only depends on ρ and Φ only depends on φ, so that

$$\begin{aligned} \frac{\partial \boldsymbol{n}}{\partial \rho} &= \Theta'(\rho)\frac{\partial \boldsymbol{n}}{\partial \Theta}, \\ \frac{\partial \boldsymbol{n}}{\partial \varphi} &= m\frac{\partial \boldsymbol{n}}{\partial \Phi}. \end{aligned} \tag{2.48}$$

This leads to the following expression for the topological charge number

$$Q = \frac{m}{4\pi}\int_0^{\infty}\int_0^{2\pi}\Theta'(\rho)\ \sin\left[\Theta(\rho)\right]\mathrm{d}\varphi\ \mathrm{d}\rho. \tag{2.49}$$

Since the integrand does not depend on φ, the integration over φ results in a factor of 2π. Substitute the integration over ρ to an integration over $\Theta(\rho)$ Eq. (2.49) becomes

$$Q = \frac{m}{2}\int_{\Theta(0)}^{\Theta(\infty)}\sin(\Theta)\ \mathrm{d}\Theta. \tag{2.50}$$

Here we see that the magnetization direction of the Skyrmion, i.e., whether it goes from $\Theta = \pi$ to $\Theta = 0$ or vice versa, also determines the sign of Q. Assuming a ferromagnetic ground state pointing in $+\boldsymbol{z}$ direction as background, i.e., $\Theta(\infty) = 0$, the Skyrmion center has to point into the opposite direction, i.e., $\Theta(0) = \pi$. The topological quantum number is calculated to $Q = -m$ and, thus, $Q = \mp 1$. By convention the Skyrmion has the quantum number $Q = -1$ while the Anti-Skyrmion has $Q = 1$ [67]. There exists a variety of objects with higher quantum numbers as $|Q| > 1$, like Skyrmion bags (or -sacks) or Skyrmionium [74, 85], but they all fulfill $Q \in \mathbb{Z}$.

The ferromagnetic state, as well as other topological trivial states, have a quantum number of $Q = 0$. Therefore, it is not possible to *continuously* transform a topological trivial state into an (Anti-) Skyrmion or vice versa. Although this holds only in the theory of smooth vector fields (in reality Skyrmion can be created and annihilated [see e.g. 86]), the change of the topological quantum number in a real system comes with high energy (-density). It means that, for instance, the decay of a non-stable Skyrmion leads to an energy density which is highly concentrated on a small area in space [87]. Also creating Skyrmions is a non-trivial task. One efficient ansatz, made by Stier *et al.*, is to create pairs of Skyrmions and Anti-Skyrmions with a spin polarized electric current [45]. These pairs have opposite topological quantum numbers $Q = \pm 1$, so that the total quantum number $Q = 1 - 1$ of the originally topological trivial system would not change. Since the Anti-Skyrmions are unstable in this system, which we will show next, they eventually decay, leaving only Skyrmions on the lattice. Even such intuitive phenomena as the decaying of unstable Anti-Skyrmions indicate that the topological protection alone is not valid in real systems. This is due to the fact that the magnetization is, in reality, not a perfectly continuous vector field. As mentioned in the introduction the stability of a Skyrmion is more an issue of the energy.

Energy of a single skyrmion

In this part we investigate the energy of a single Skyrmion. Most of the properties of the ferromagnetic Skyrmion we derive in this Section can be found in Ref. [65], which is one of the fundamental works regarding magnetic Skyrmions. We consider the magnetization as a continuous vector field $\boldsymbol{n}$ with an energy, taken from Eq. (2.37),

$$E = \int \left\{ A(\boldsymbol{\nabla} \boldsymbol{n})^2 + \mathcal{E}_{\mathrm{DMI}} - \boldsymbol{B}_0 \cdot (\boldsymbol{n} - \boldsymbol{z}) - K(n_z^2 - 1) \right\} \mathrm{d}^2 \boldsymbol{r}, \tag{2.51}$$

where the energy of the homogeneous ferromagnetic state is already subtracted, so that the classical ferromagnetic ground state yields $E_{\mathrm{FM}} = 0$. As explained previously, the term $\mathcal{E}_{\mathrm{DMI}}$ refers to the DM energy density depending on whether we consider bulk DMI or interfacial DMI (see Eq. (2.38)). As for the calculations of the topological quantum number above, we consider the system in polar coordinates (ρ, φ) and assume a single Skyrmion. Again, due to the explicit formulation of Φ the integral over φ can be solved, while the integration over ρ has to persist. Following the typical convention that the Skyrmion has a quantum number $Q = -1$ and $m = 1$ and, respectively the Anti-Skyrmion $Q = 1$ and $m = -1$, the energy of an Anti-Skyrmion is

$$\begin{aligned} E_{\mathrm{ASk}} = \int_0^\infty \Big\{ & \pi J \rho \left[\Theta'(\rho) \right]^2 + \frac{\pi J \sin^2 \left[\Theta(\rho) \right]}{\rho} \\ & + 4\pi\rho \sin^2 \left[\frac{\Theta(\rho)}{2} \right] \left(B_0 + K \cos[\Theta(\rho)] + K \right) \Big\} \mathrm{d}\rho. \end{aligned} \tag{2.52}$$

We see that it neither depends on the DMI[3], nor on φ_0. Although we do not know the explicit form of $\Theta(\rho)$, it is possible to estimate the Anti-Skyrmion energy based on boundary conditions. The center spin of the Skyrmion aligns in $-z$ direction and it is, thus, $\Theta(0) = \pi$. Sufficiently far away from the Skyrmion the system is assumed to be in the ferromagnetic ground state. Therefore we conclude $\Theta(\rho \gg R) = 0$, where R is the Skyrmion radius. Based on simulations (see Appendix A) or numerical solutions of the condition in Eq. (2.45) (see Ref. [62]) we know that $\Theta(\rho)$ is monotonic and can, thus, only take values between π and 0. Consequently, nearly each single term in Eq. (2.52) is positive valued for $0 \leq \Theta \leq \pi$. The only exception is $K\cos[\Theta(\rho)]$ which is countered since it stands in the sum with K. Therefore, we conclude that the energy of an Anti-Skyrmion is, independent of the parameter choice, larger than the energy of the ferromagnetic homogeneous state. Next, we regard the Skyrmion energy considering interfacial and bulk DMI, respectively, i.e.,

$$E_{\mathrm{if}} = E_{\mathrm{ASk}} - \pi D\cos(\varphi_0)\int_0^\infty \left\{2\rho\Theta'(\rho) + \sin[2\Theta(\rho)]\right\}\mathrm{d}\rho, \tag{2.53}$$

$$E_{\mathrm{b}} = E_{\mathrm{ASk}} + \pi D\sin(\varphi_0)\int_0^\infty \left\{2\rho\Theta'(\rho) + \sin[2\Theta(\rho)]\right\}\mathrm{d}\rho. \tag{2.54}$$

The energy of a Skyrmion can be viewed as an oscillation based on φ_0 around the energy of the Anti-Skyrmion. The weight (or amplitude) of the oscillation is proportional to the DMI strength D and a constant which depends on the Skyrmion size and form. For the following considerations the sign of the integral $\int_0^\infty \{2\rho\Theta'(\rho) + \sin[2\Theta(\rho)]\}\,\mathrm{d}\rho$ plays a crucial role. It can be estimated by the rough approximation that the Skyrmion angle Θ goes linear from π to 0. The explicit form $\Theta(\rho) \approx \pi(1 - \frac{\rho}{2R})$, where R is the Skyrmion radius, is sometimes called triangular Skyrmion and has the integration boundaries 0 and R, see Refs. [66, 87]. By this we can conclude that the integrals in the Eqs. (2.53) and (2.54) are negative, even though we do not know the explicit value. Thus, the energy considering an interfacial DMI is minimized by $\varphi_0 = \pi$, while the energy considering a bulk DMI is minimal at $\varphi_0 = \pi/2$. The direct consequence is that interfacial DMI stabilizes Néel Skyrmions, $\varphi_0 = \pi$, and bulk DMI stabilizes Bloch Skyrmions $\varphi_0 = \pi/2$. Regarding Eqs. (2.53) and (2.54) there should always be a φ_0 with which the Skyrmion is favored over the Anti-Skyrmion. However, this is only true for the energy contributions considered here in addition with the restriction to what we call interfacial and bulk DMI. If one considers materials with D_{2d} symmetry, the DMI contributes to the energy of both, Skyrmions and Anti-Skyrmions (see Ref. [66]). This can lead to a stabilization of Anti-Skyrmions [88]. Furthermore, by including other energy contributions such as magnetic dipolar interaction one can, theoretically and practically, stabilize Anti-Skyrmions [89, 90]. Nevertheless, in this thesis we explicitly consider only bulk and interfacial DMI leading to Bloch- and Néel-type Skyrmions, respectively.

[3]We calculated the energies for bulk and interfacial DMI separately.

Bloch- and Néel-type skyrmions

Previously it was shown that the topological property $Q = \pm 1$ is independent of the parameter φ_0. Thus, the topological protection holds equally for Skyrmions, $m = 1$, and Anti-Skyrmions, $m = -1$, of the both types $\varphi_0 \in \{\frac{\pi}{2}, \pi\}$ considered here. A graphical representation of these two Skyrmion types (with $m = 1$) is shown in Fig. 2.3, where the arrows represent the vector field $\boldsymbol{n}$ and the color code indicates the z component of the vector field. These two graphics illustrate the difference that a simple phase shift of

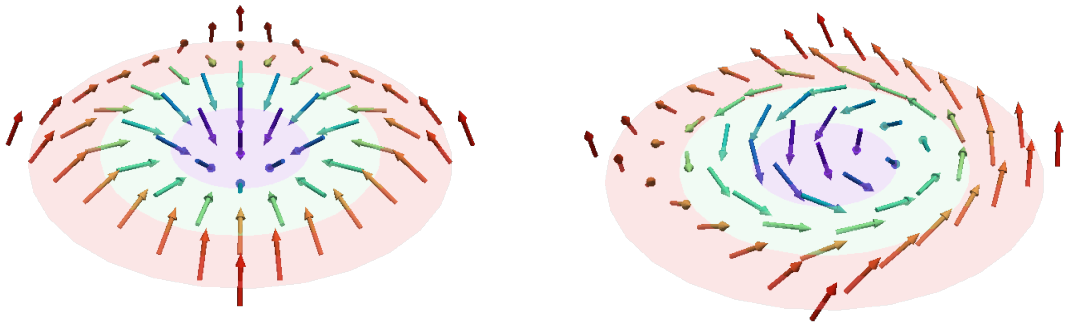

Figure 2.3.: Arrow representation of the vector field $\boldsymbol{n}$ of a Skyrmion. The color code indicates the z component of the vector field. Left: Néel-type Skyrmion. Right: Bloch-type Skyrmion.

$\Phi \to \Phi - \frac{\pi}{2}$ in the Skyrmion yields. The arrow representations enable us to graphically imagine the two Skyrmion types. However, to fully grasps the underlying symmetry of the Skyrmion types it is convenient to express the impact of φ_0 to the trigonometric forms

$$\cos(\varphi + \varphi_0) = \cos(\varphi)\cos(\varphi_0) - \sin(\varphi)\sin(\varphi_0), \tag{2.55}$$

$$\sin(\varphi + \varphi_0) = \sin(\varphi)\cos(\varphi_0) + \cos(\varphi)\sin(\varphi_0). \tag{2.56}$$

Since we only distinguish here between Néel- and Bloch-type Skyrmions, it is sufficient to regard the two cases $\varphi_0 = \pi$ (Néel) and $\varphi_0 = \pi/2$ (Bloch). A Néel-type Skyrmion can be continuously transformed into a Bloch-type Skyrmion, without changing the topological quantum number Q, by

$$\begin{pmatrix} -\cos(\varphi) \\ -\sin(\varphi) \end{pmatrix} \to \begin{pmatrix} -\sin(\varphi) \\ \cos(\varphi) \end{pmatrix}. \tag{2.57}$$

Thus, transforming a Néel- into a Bloch-type Skyrmion can be done by $(x, y) \to (y, -x)$ (and vice versa via back transform $(x, y) \to (-y, x)$). Next, we consider the Anti-Skyrmion of each type. Continuously transforming a Skyrmion into an Anti-Skyrmion is not possible since it changes the topological quantum number $Q = 1 \to Q = -1$ and, as explained above, the topological quantum number can only be an integer number $Q \in \mathbb{Z}$. The

transformation from Skyrmion to Anti-Skyrmion yields for each case

$$\begin{pmatrix} -\cos(\varphi) \\ -\sin(\varphi) \end{pmatrix} \rightarrow \begin{pmatrix} -\cos(\varphi) \\ \sin(\varphi) \end{pmatrix} \quad \text{and} \quad \begin{pmatrix} -\sin(\varphi) \\ \cos(\varphi) \end{pmatrix} \rightarrow \begin{pmatrix} \sin(\varphi) \\ \cos(\varphi) \end{pmatrix} . \tag{2.58}$$

The transformation from a Skyrmion to an Anti-Skyrmion is for the Néel Skyrmion $(x, y) \rightarrow (x, -y)$ and for the Bloch Skyrmion $(x, y) \rightarrow (-x, y)$. The crucial difference to the Néel $\leftrightarrow$ Bloch transformation here is that the sign of one component is changed but not the component itself (x stays at x and y at y). This prevents a continuous transformation. Note that the Néel $\leftrightarrow$ Bloch transformation is still the same for Anti-Skyrmions. Similar to Fig. 2.3 the two Anti-Skyrmions are shown in Fig. 2.4. The pictures are taken from a different perspective for a better visibility. In contrast to the Skyrmions in Fig. 2.3, the Anti-Skyrmions are equivalent on rotation in the x-y plane [see 67].

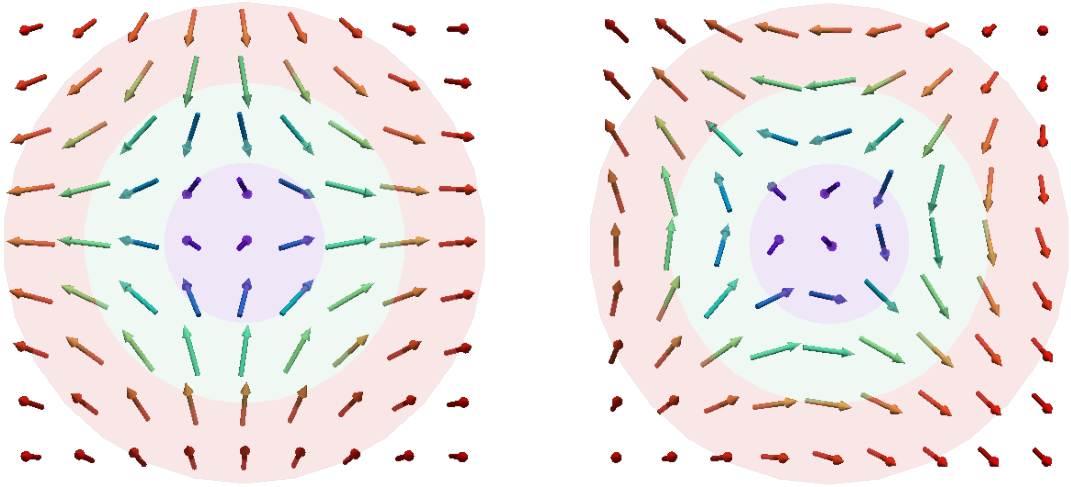

Figure 2.4.: Arrow representation of the vector field $\boldsymbol{n}$ of an Anti-Skyrmion. The color code indicates the z component of the vector field. Left: Néel-type Anti-Skyrmion. Right: Bloch-type Anti-Skyrmion.

2.5. Antiferromagnetic skyrmions

The focus of this thesis lies on antiferromagnetic Skyrmions. More precisely, antiferromagnetic systems that can be separated into two ferromagnetic sublattices (bipartite antiferromagnets). Consequently, we can rely on the knowledge about ferromagnetic Skyrmions, as discussed in this chapter, among other sources. For analytical calculations regarding Skyrmions, we mostly consider the (sublattice-) magnetization as continuous vector fields. We use an expression for the energy, inspired by Bogdanov *et al.* [31], where the choice of parameters determines which explicit system, or material, is considered. The energy is

given by [51]

$$\begin{aligned} W = \int \mathrm{d}^2\boldsymbol{r}\Big\{ & \frac{\lambda}{2}\boldsymbol{a}\boldsymbol{b} + \frac{A'}{2}\sum_{\mu\in\{x,y\}}\Big[(\partial_\mu \boldsymbol{a})^2 + (\partial_\mu \boldsymbol{b})^2\Big] \\ & + A\sum_{\mu\in\{x,y\}}\left[(\partial_\mu \boldsymbol{a})\,(\partial_\mu \boldsymbol{b})\right] + D\boldsymbol{a}\cdot(\boldsymbol{\nabla}\times\boldsymbol{b}) \\ & + \frac{D'}{2}\left[\boldsymbol{a}\cdot(\boldsymbol{\nabla}\times\boldsymbol{a}) + \boldsymbol{b}\cdot(\boldsymbol{\nabla}\times\boldsymbol{b})\right] - \frac{K'}{2}(a_z^2 + b_z^2) \\ & - K a_z b_z\Big\} \end{aligned} \tag{2.59}$$

where the homogeneous (λ) and inhomogeneous (A, A') parts of the exchange interaction are included, as well as the Dzyaloshinskii-Moriya interactions (D' and D) and the magnetocrystalline anisotropy (K' and K) in z-direction. The notation here is chosen in such a way that the non-primed parameters denote the interaction between the two sublattices, called *inter-sublattice* interaction, while the primed parameters mark the interactions within each sublattice, the *intra-sublattice* interaction [51]. All parameters can be adapted to model a specific system while the energy still fulfills the structure, e.g. symmetries, of Eq. (2.59). In Chapter 4 and for the simulation (Appendix A) we particularly consider a discrete lattice. In order to compare it to analytical calculations or other publications which consider continuous vector fields, we have to translate the lattice perspective to the a continuous vector field. In this thesis two specific models are considered for lattice representation. In the Chapter 4 we consider a two-dimensional bipartite monolayer square lattice for both, analytical calculations and simulations. In Chapter 3 the simulations are done for two different models, one of which is the same as in Ch. 4, while the other is a synthetic bilayer antiferromagnet. In contrast, the analytical calculations in Ch. 3 are based on the universal expression for the energy, Eq. (2.59). Therefore, we will explain these two explicit models.

Single layer antiferromagnetic square lattice

This particular system is a two-dimensional antiferromagnetic square lattice with equal distance between each lattice points in x and y direction, called the lattice constant d. It is based on the ferromagnetic lattice which is used in, e.g., Refs. [45, 91]. The essential lattice Hamiltonian without further assumptions reads the same for ferromagnetic and antiferromagnetic lattices

$$H = -\frac{J}{2}\sum_{\langle i,j\rangle}\boldsymbol{M}_i\boldsymbol{M}_j - D\sum_{\langle i,j\rangle}\boldsymbol{r}_{ij}\left[\boldsymbol{M}_i\times\boldsymbol{M}_j\right] - K\sum_i\left(M_i^z\right)^2, \tag{2.60}$$

for bulk DMI and

$$H = -\frac{J}{2}\sum_{\langle i,j\rangle}\boldsymbol{M}_i\boldsymbol{M}_j - D\sum_{\langle i,j\rangle}(\boldsymbol{r}_{ij}\times\boldsymbol{z})\left[\boldsymbol{M}_i\times\boldsymbol{M}_j\right] - K\sum_i\left(M_i^z\right)^2, \tag{2.61}$$

for interfacial DMI. Here $\boldsymbol{M}_i$ denotes the classical magnetic moment on each lattice site and $\boldsymbol{r}_{ij}$ is a position vector (yielding $\boldsymbol{r}_{ij} = -\boldsymbol{r}_{ji}$). It is convenient to eliminate the double sum notation and express the Hamiltonian as a single sum over the lattice explicitly denoting the nearest neighbors

$$\begin{aligned} H = &-\frac{J}{2}\sum_i \boldsymbol{M}_i(\boldsymbol{M}_{i+x} + \boldsymbol{M}_{i-x} + \boldsymbol{M}_{i+y} + \boldsymbol{M}_{i-y}) \\ &- D\sum_i \boldsymbol{M}_i\left([\boldsymbol{M}_{i+x} - \boldsymbol{M}_{i-x}] \times \boldsymbol{x} + [\boldsymbol{M}_{i+y} - \boldsymbol{M}_{i-y}] \times \boldsymbol{y}\right) \\ &- K\sum_i \left(M_i^z\right)^2, \end{aligned} \tag{2.62}$$

for bulk DMI and

$$\begin{aligned} H = &-\frac{J}{2}\sum_i \boldsymbol{M}_i(\boldsymbol{M}_{i+x} + \boldsymbol{M}_{i-x} + \boldsymbol{M}_{i+y} + \boldsymbol{M}_{i-y}) \\ &- D\sum_i \boldsymbol{M}_i\left([\boldsymbol{M}_{i+y} - \boldsymbol{M}_{i-y}] \times \boldsymbol{x} - [\boldsymbol{M}_{i+x} - \boldsymbol{M}_{i-x}] \times \boldsymbol{y}\right) \\ &- K\sum_i \left(M_i^z\right)^2, \end{aligned} \tag{2.63}$$

for interfacial DMI. The assumption is that with a negative exchange constant $J < 0$ spins on neighboring lattice sites would align roughly anti-parallel which leads to the rise of two approximately anti-parallel sublattices A and B. These are ordered checkerboard-like. For classical spins and neglecting the influence of the DMI the ground state of the (anti-) ferromagnet is a homogeneous co-linear orientation in the direction of the easy axis (here z direction) of all spins, as shown in Fig. 2.5. Any arbitrary stationary structure in the

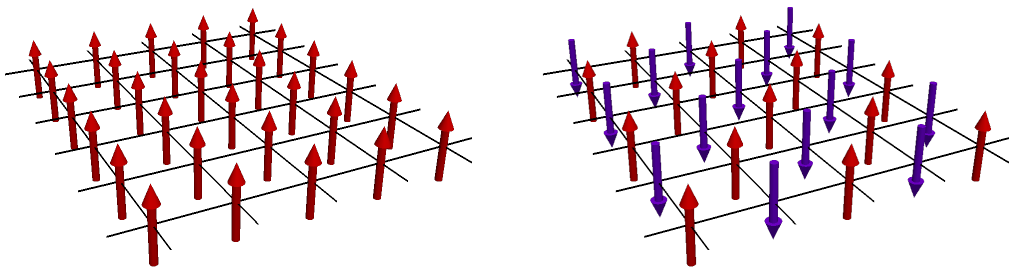

Figure 2.5.: Arrow representation of the classical ground state in a ferromagnetic lattice (left) and an antiferromagnetic lattice (right).

ferromagnetic lattice, such as a Skyrmion, can be precisely transformed to an analogous structure in the antiferromagnetic lattice within this model by switching the sign of each spin in one sublattice and changing the parameters from $J \to -J$ and $D \to -D$. In detail, the Hamiltonian in Eq. (2.60) consists of two nearest neighbor interaction terms and one

on-site interaction term. The on-site interaction term only depends on the absolute value of the z component of the magnetic moment. Thus, it is constant under a sign switch of the z component. The two other terms consist of essentially products of $\boldsymbol{M}_i$ and its neighbors $\boldsymbol{M}_{i\pm x}$ and $\boldsymbol{M}_{i\pm y}$. Since two neighboring lattice sites are, per definition, from different sublattices, changing the sign of one $\boldsymbol{M}_i \to -\boldsymbol{M}_i$ would only add a sign to the interaction, e.g., $\boldsymbol{M}_i \cdot \boldsymbol{M}_{i\pm x} \to -\boldsymbol{M}_i \cdot \boldsymbol{M}_{i\pm x}$. This sign can be countered by also changing the sign of the parameter $J \to -J$ and $D \to -D$. We also confirmed this by simulating a stationary Skyrmion in both cases, ferromagnetic and antiferromagnetic. Consequently, Skyrmion properties regarding the whole antiferromagnetic Skyrmion (not only a specific sublattice) are calculated by multiplying each second spin by -1 and handling the AFM Skyrmion as a ferromagnetic one.

In Chapter 3, we derive an analytical formalism where we consider the Skyrmion formed by a continuous vector field $\boldsymbol{n}(x, y)$. Since we still use the lattice representation of the Skyrmion in the simulation, both models should be comparable. In the following we derive the approximation of the antiferromagnetic lattice by two effectively coupled continuous sublattice vector fields A and B. For the sake of simplicity the concept will be explained in a one-dimensional example and can, for the square lattice, easily be adapted to the two-dimensional case assuming a one-dimensional arrangement of N lattice site spins $\boldsymbol{M}_i$ which are labeled by increasing numbers from $i = 0$ to $i = N - 1$. We use the convention that each lattice site denoted by an even number is of sublattice A and each odd labeled lattice site is of sublattice B. So we ensure that a lattice site has only neighbors from the respective other sublattice. Therefore, sublattice A consists of $\boldsymbol{M}_0, \boldsymbol{M}_2, \boldsymbol{M}_4, ...$ while sublattice B consists of $\boldsymbol{M}_1, \boldsymbol{M}_3, \boldsymbol{M}_5$ and so on. Since we separated the lattice into sublattices, we denote, as a convention, each spin from sublattice A as $\boldsymbol{a}_i$ and each spin of sublattice B as $\boldsymbol{b}_i$. By this we are able to express, for instance, the term $\boldsymbol{M}_i \cdot (\boldsymbol{M}_{i+1} + \boldsymbol{M}_{i-1})$, assuming i is in sublattice A, by $\boldsymbol{a}_i \cdot (\boldsymbol{b}_{i+1} + \boldsymbol{b}_{i-1})$. Note that using this convention, we can write the Hamiltonian from Eq. (2.62) as

$$\begin{aligned} H = &- \frac{J}{2} \sum_{i \in A} \boldsymbol{a}_i (\boldsymbol{b}_{i+x} + \boldsymbol{b}_{i-x} + \boldsymbol{b}_{i+y} + \boldsymbol{b}_{i-y}) \\ &- \frac{J}{2} \sum_{i \in B} \boldsymbol{b}_i (\boldsymbol{a}_{i+x} + \boldsymbol{a}_{i-x} + \boldsymbol{a}_{i+y} + \boldsymbol{a}_{i-y}) \\ &- D \sum_{i \in A} \boldsymbol{a}_i \left([\boldsymbol{b}_{i+x} - \boldsymbol{b}_{i-x}] \times \boldsymbol{x} + [\boldsymbol{b}_{i+y} - \boldsymbol{b}_{i-y}] \times \boldsymbol{y} \right) \\ &- D \sum_{i \in B} \boldsymbol{b}_i \left([\boldsymbol{a}_{i+x} - \boldsymbol{a}_{i-x}] \times \boldsymbol{x} + [\boldsymbol{a}_{i+y} - \boldsymbol{a}_{i-y}] \times \boldsymbol{y} \right) \\ &- K \sum_{i \in A} \left(a_i^z\right)^2 - K \sum_{i \in B} \left(b_i^z\right)^2 , \end{aligned} \tag{2.64}$$

and the respective other DMI for the interfacial symmetry case. Next, we return to the easier one-dimensional model for explanation. The same lattice indices for A and B allow

us to keep track of the position. We note that odd lattice sites do not exist in the sublattice A and even ones do not exist in B. Therefore, we will call those *virtual* lattice sites. For instance, the vector $\boldsymbol{b}_i$ for $i \in A$ will be on such a virtual lattice site. However, since the goal is to compare the discrete lattice model with the model of continuous vector fields, we interpolate between two magnetic moments which are neighbored on the *same* sublattice. This interpolation naturally also includes the virtual lattice sites[4]. By this we still regard two different sublattices and interpolate over each sublattice separately. To do so we transform the lattice site into a position information $\boldsymbol{M}_i \to \boldsymbol{M}(x)$ and introduce an equal spacing, the lattice constant d. This means that the lattice sites $\boldsymbol{M}_i$ and $\boldsymbol{M}_{i+1}$ have a distance of d. Consequently, the distance between two lattice sites in one sublattice is $2d$. The approximation into a continuous vector field is usually done by the Taylor expansion up to second order from a point between two lattice sites (see Ref. [87]). In our case this point is the virtual lattice site for each sublattice, i.e.,

$$\boldsymbol{a}_{i\pm1} \approx \boldsymbol{a} \pm d\partial_x \boldsymbol{a} + \frac{d^2}{2}\partial_x^2 \boldsymbol{a}, \tag{2.65}$$

$$\boldsymbol{b}_{j\pm1} \approx \boldsymbol{b} \pm d\partial_x \boldsymbol{b} + \frac{d^2}{2}\partial_x^2 \boldsymbol{b}, \tag{2.66}$$

where i is in sublattice B and j is in sublattice A. In Fig. 2.6, this method is illustrated for the purpose of visualization. In the left picture the one dimensional lattice is seen where the lattice sites are represented by black dots and the arrows indicate the projection of the spins onto the z axis. The arrows are color coded whether they belong to sublattice A (blue) or B (green). The right picture shows the idea of how the continuum approximation is applied in this case. The lattice was (only for visualization) separated into two sublattices and the dotted circles represent the virtual lattice sites. Neighbored spins of the two different sublattices are still connected which indicates the effective coupling between the sublattice fields. The solid curves going over the arrowheads represent the continuous vector field approximated by interpolating between the discrete sublattice sites. As one can see in Eq. (2.65) the continuum approximation gets better the smaller the lattice constant d is. This coincides with the intuition that a higher density of lattice sites in a structure is closer to a continuous vector field. It is also a topic of recent studies [see 87]. For the purpose of calculating the energy, we have to transform the summation over the lattice sites to an integral. Since we consider a two-dimensional lattice this is done by $\sum_i \to (1/d^2)\int \mathrm{d}x\mathrm{d}y$. At this point it is important to note that whenever the summation is only over one sublattice, e.g., $\sum_{i\in A}$ as in Eq. (2.64), it has to be considered in the integral. Since only half the lattice sites is counted, it transforms into $\sum_{i\in A} \to (1/2d^2)\int \mathrm{d}x\mathrm{d}y$. This

[4]For example we have the spins b_3 and b_5 on a discrete lattice. The interpolation creates a vector for each position between site 3 and 5. Thus b_4 comes into existence.

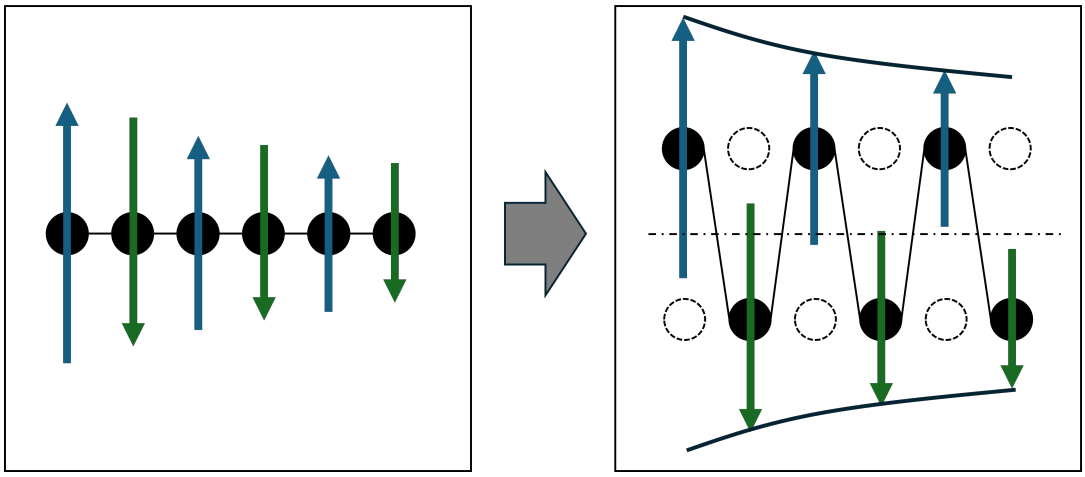

Figure 2.6.: Graphical representation of approximating the monolayer antiferromagnetic lattice to two continuous sublattice vector fields. The arrows represent the projection to the z component in order to keep the presentation simple for the eye. Black dots indicate the lattice sites. Left: Antiferromagnetic lattice without further assumptions. The different sublattices are of different color. Right: Two sublattices separated yet still connected by the lattice architecture (solid line). Full black dots indicate the actual lattice sites, while the hollow dots are virtual lattice sites. The curves over the arrow heads are the smooth interpolations $a_i^z \to a_z(x)$ and $b_i^z \to b_z(x)$.

is done similar for sublattice B. The energy from Eq. (2.64) then transforms to

$$\begin{aligned} H = &- \frac{J}{4d^2} \int 4\boldsymbol{a}\boldsymbol{b} + \boldsymbol{a}d^2(\partial_x^2 + \partial_y^2)\boldsymbol{b} \; \mathrm{d}x\mathrm{d}y \\ &- \frac{J}{4d^2} \int 4\boldsymbol{b}\boldsymbol{a} + \boldsymbol{b}d^2(\partial_x^2 + \partial_y^2)\boldsymbol{a} \; \mathrm{d}x\mathrm{d}y \\ &- \frac{D}{2d^2} \int \boldsymbol{a}\left(2d\partial_x\boldsymbol{b} \times \boldsymbol{x} + 2d\partial_y\boldsymbol{b} \times \boldsymbol{y}\right) \; \mathrm{d}x\mathrm{d}y \\ &- \frac{D}{2d^2} \int \boldsymbol{b}\left(2d\partial_x\boldsymbol{a} \times \boldsymbol{x} + 2d\partial_y\boldsymbol{a} \times \boldsymbol{y}\right) \; \mathrm{d}x\mathrm{d}y \\ &- \frac{K}{2d^2} \int \left(a_z^2 + b_z^2\right) \mathrm{d}x\mathrm{d}y. \end{aligned} \tag{2.67}$$

Integration by parts, for example $\int \boldsymbol{a}(\partial_x^2\boldsymbol{b}) \; \mathrm{d}x\mathrm{d}y = -\int(\partial_x\boldsymbol{a})(\partial_x\boldsymbol{b}) \; \mathrm{d}x\mathrm{d}y$ and $\int \boldsymbol{a}(\partial_x\boldsymbol{b} \times x) \; \mathrm{d}x\mathrm{d}y = \int \boldsymbol{b}(\partial_x\boldsymbol{a} \times x) \; \mathrm{d}x\mathrm{d}y$, allows us to symmetrize the energy to

$$\begin{aligned} H = \int \Bigg\{ &- \frac{2J}{d^2}\boldsymbol{a}\boldsymbol{b} + \frac{J}{2} \sum_{\mu \in \{x,y\}} (\partial_x\boldsymbol{a})(\partial_x\boldsymbol{b}) \\ &+ \frac{2D}{d}\boldsymbol{a} \cdot (\boldsymbol{\nabla} \times \boldsymbol{b}) - \frac{K}{2d^2}\left(a_z^2 + b_z^2\right) \Bigg\} \mathrm{d}x\mathrm{d}y. \end{aligned} \tag{2.68}$$

In summary, this is the energy in the continuum approximation we consider for the two-dimensional antiferromagnetic square lattice. Compared to the more universal AFM energy description inspired by Bogdanov *et al.* in Eq. (2.59) it turns out that both are

identical if we chose the parameter such that: $\lambda \to -\frac{4J}{d^2}$, $A \to \frac{J}{2}$, $D \to \frac{2D}{d}$, and $K' \to \frac{K}{d^2}$ as well as setting the parameter A', D', K to zero. A crucial parameter in this description is the lattice constant d. Throughout this thesis the lattice constant d is essentially a unit so that the results of this work can be compared to other theoretical models or experiments. Other works, however, rely on the same continuum approximation and tune the lattice constant d to show that the continuum description gets more realistic the lower d is. For example in Ref. [87] the decay of a single FM Skyrmion is studied in dependence of, among others, the lattice constant. It turns out that the smaller the lattice constant, the slower a Skyrmion decays. This coincides with the fact that the topological protection of a Skyrmion becomes more relevant the better a continuous vector field is resembled. While the continuum model presented here, based on the two-dimensional square lattice, yields promising results that align with numerical simulations (as discussed with examples below in Chapter 3), the experimental observation of a Skyrmion in a single-layer antiferromagnet continues to remain elusive. Therefore, an additional system is regarded in this thesis - the synthetic bilayer antiferromagnet.

Synthetic bilayer antiferromagnet

In principle, a synthetic antiferromagnet (SAF) consists of two, or an even number, of ultrathin antiferromagnetically coupled ferromagnetic layers which are separated by a nonmagnetic layer (spacer) [92]. The coupling of the layers are through a Ruderman-Kittel-Kasuya-Yosida (RKKY)–type interlayer interaction [29, 93]. In this thesis, we focus exclusively on two layers, referring to the system specifically as a bilayer antiferromagnet to emphasize this distinction. Currently, research is being conducted on synthetic AFM materials that can stabilize Skyrmions. In 2020 Legrand *et al.* showed that it is possible to stabilize Skyrmions in a SAF at room temperature compensate of Pt/Co/Ru [29]. In experiments the thickness of each material layer on the stack (especially the spacer) can be varied in order to adapt the parameter. It was demonstrated by Van Tuong Pham *et al.* that those AFM Skyrmions can be moved by an electric current with velocities up to $v = 900$ m/s [94]. To visually illustrate the modeling of the synthetic bilayer antiferromagnet in the simulations, the left image of Fig. 2.7 presents a three-dimensional arrow representation of the two antiferromagnetically coupled sublattices. The right image in this figure shows an exemplary material stack used in experiments. The depicted stack is used in Ref. [29] and can host Skyrmions at room temperature. As a model, we consider the synthetic bilayer AFM as two typical ferromagnetic layers which are antiferromagnetically coupled. Following Ref. [28] we assume the interlayer coupling to be Heisenberg-like and only acting between each two sublattice spins which are on the same lattice site i, while the strength of the coupling is scaled by a parameter J_{inter}. Concretely, the Hamiltonian is

$$H = H_A + H_B + J_{\text{inter}} \sum_i \boldsymbol{S}_i^A \cdot \boldsymbol{S}_i^B, \tag{2.69}$$

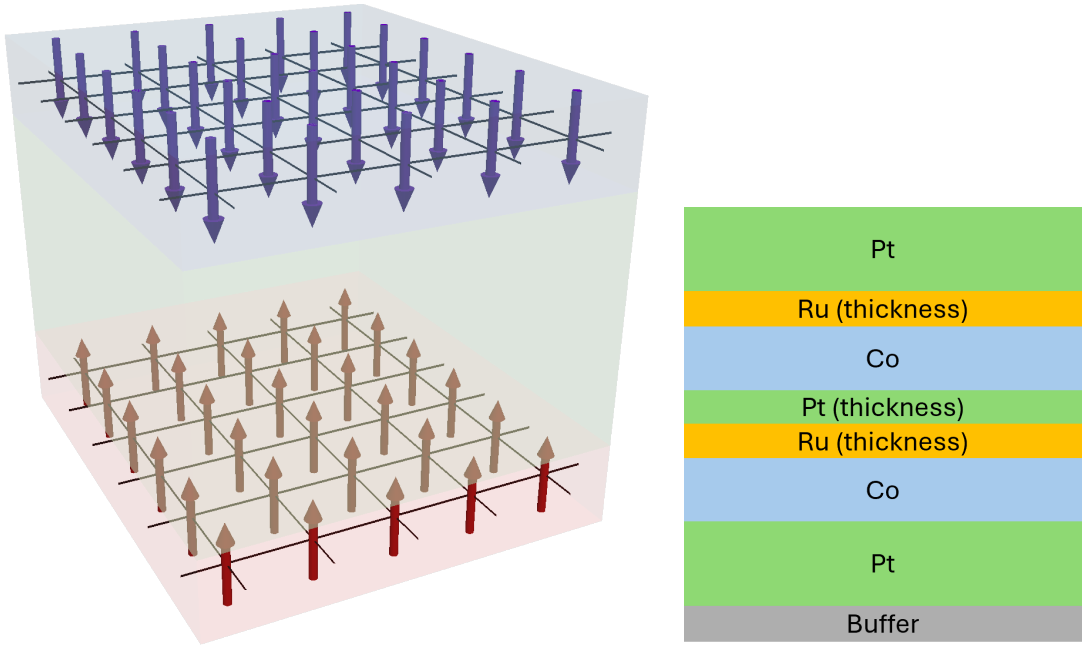

Figure 2.7.: Left: Arrow representation of the synthetic bilayer system as a model for the simulations. Right: Scheme of the material stack for a SAF in experiments, e.g. Ref. [29]. The arrows from the left picture are in the Cobalt layer.

where A and B denote the two sublattices. Regarding continuous vector fields we consider two ferromagnetic Hamiltonians, like those of Eq. (2.37), for each sublattice, $\mathcal{H}_A$ and $\mathcal{H}_B$, and an additional Heisenberg-like coupling as in Eq.(2.69). The resulting energy density is

$$\mathcal{H} = \mathcal{H}_A + \mathcal{H}_B + \frac{J_{\text{inter}}}{d^2}\boldsymbol{n}_A \cdot \boldsymbol{n}_B \tag{2.70}$$

where we scaled the interlayer coupling parameter with $1/d^2$ due to integration. This model can be resembled with the universal AFM energy from Eq. (2.59) by identifying the parameter $\lambda = 2J_{\text{inter}}/d^2$ as well as setting the parameter A, D and K to zero. Although it is the easiest realization of an AFM system, it is the most promising when it comes to comparison with experiments.

3. Antiferromagnetic skyrmion dynamics by sublattice displacement

Antiferromagnetic (AFM) Skyrmions attracted recently the focus of research. They can be seen as a compound of two ferromagnetic sublattice Skyrmions whose Skyrmion Hall effect cancels out when moving under the influence of an electric current. It has been theoretically predicted that AFM Skyrmions appear in many kinds of systems [26, 28], however, up to now they are experimentally detected only in synthetic AFM [29]. In numerical simulations it was found that AFM Skyrmions, in contrast to their ferromagnetic counterparts, exhibit an inertial mass and accelerate like classical massive particles [26, 27, 32]. An often-cited advantage of AFM Skyrmions in technological applications is the absence of a Skyrmion Hall effect (SHE) when driven by electric currents. It is intuitively asserted that the SHE of both sublattice Skyrmions cancels each other out, without addressing the underlying interactions between the two sublattice Skyrmions that are driven in opposing directions. Rather, the issue of current-driven AFM Skyrmions is often described in terms of staggered magnetization and magnetization dynamics. In this context, it is assumed that the magnetization is very small and that the Skyrmion can be effectively described by the staggered magnetization [27]. In this chapter we elucidate the role of the two sublattices and, in particular, their displacement in relation to the dynamics and the generation of the Skyrmion mass.

3.1. Skyrmion equation of motion

In 1972 A. A. Thiele derived an equation of forces which governs the steady-state motion of magnetic bubble domains [50]. A brief overview of the Thiele equation is found in Chapter 2. Since this topic is crucial for understanding the AFM Skyrmion dynamics induced by sublattice displacement, govern in this chapter, we will revisit Thiele's approach here with more detail. The main, and strong, approximation made by Thiele is to view the domain (for us: the Skyrmion) as a localized rigid structure without internal excitations. By this, the coordinates of the magnetic vector field can be simplified to the form of the magnetic structure and its position $\boldsymbol{M}_i = \boldsymbol{M}_i(x_j - X_j)$ [50]. While Thiele explicitly mentioned a steady-state motion in the original work $\boldsymbol{M}_i = \boldsymbol{M}_i(x_j - v_j t)$ [50], we assume an arbitrary time dependence for the position of the Skyrmion. Due to this we, strictly speaking, use a *collective coordinate* approach where we assume that the time dependence of the whole system can be described by a set of collective coordinates [95, 96]; which is an

appropriate method for antiferromagnetic systems [97]. In principle, the time evolution of any magnetic structure can approximately be described by a set of N time-dependent collective coordinates based on the desired topic of study. For instance, if one wants to describe the shrinking of a single Skyrmion, the radius and helicity would be a promising choice of collective coordinates while the Skyrmion position does not yield any additional insights (since the Skyrmion is stationary in this case) (cf. [87]). Intuitively, the more collective coordinates one chooses, the more degrees of freedom are allowed in the system which consequently leads to a better approximation. Nevertheless, in this chapter we use only the Skyrmion position as collective coordinates, $\boldsymbol{n}(\boldsymbol{r},t) = \boldsymbol{n}(\boldsymbol{r}-\boldsymbol{R}(t))$, leading to a generalized Thiele equation [95, 96]. This has the consequence that the time derivative of the magnetization is given by the velocity of the rigid structure as well as by a spatial derivative

$$\partial_t \boldsymbol{n} = -(\boldsymbol{v}\cdot\boldsymbol{\nabla})\boldsymbol{n}. \tag{3.1}$$

This is so because the structure is rigid and, thus, not time-dependent while the time derivative of the position is the velocity of the structure. The spatial derivative of the vector field is due to the chain rule of the derivative. We note that other literature, e.g. Ref. [97], describes antiferromagnetic dynamics in terms of the magnetization $\boldsymbol{m} = (\boldsymbol{a}+\boldsymbol{b})/2$ and the staggered magnetization $\boldsymbol{l} = (\boldsymbol{a}+\boldsymbol{b})/2$ which leads to second-order time derivatives in the given order parameters. They conclude that the collective coordinate approach leads to $\partial_t^2\boldsymbol{m} = \ddot{x}\partial_x\boldsymbol{m}+\mathcal{O}(\dot{x}^2)$, where the quadratic order terms $\mathcal{O}(\dot{x}^2)$ can be neglected [27, 97]. In contrast, in this thesis we stay in the sublattice picture so that the calculations are based on the Landau-Lifshitz-Gilbert (-Slonczewski) equation which contains only the first-order time derivative. Applying Eq. (3.1) in the equation of motion (2.11) yields

$$-(\boldsymbol{v}\cdot\boldsymbol{\nabla})\boldsymbol{n} = -\gamma\boldsymbol{n}\times\boldsymbol{H}_{\text{eff}} - \alpha\boldsymbol{n}\times(\boldsymbol{v}\cdot\boldsymbol{\nabla})\boldsymbol{n} + (\boldsymbol{j}\cdot\boldsymbol{\nabla})\,\boldsymbol{n} - \beta\boldsymbol{n}\times[(\boldsymbol{j}\cdot\boldsymbol{\nabla})\,\boldsymbol{n}]\,. \tag{3.2}$$

It is convenient to simplify this equation by combining terms of the same structure. Equation (3.2) then becomes

$$-[(\boldsymbol{v}+\boldsymbol{j})\cdot\boldsymbol{\nabla}]\boldsymbol{n} + \gamma\boldsymbol{n}\times\boldsymbol{H}_{\text{eff}} + \boldsymbol{n}\times[(\alpha\boldsymbol{v}+\beta\boldsymbol{j})\cdot\boldsymbol{\nabla}]\boldsymbol{n} = 0. \tag{3.3}$$

Next, we multiply the vector field $\boldsymbol{n}$ via vector product from the right-hand side to Eq. (3.3). We use the fact that $(\boldsymbol{a}\times\boldsymbol{b})\times\boldsymbol{c} = (\boldsymbol{a}\cdot\boldsymbol{c})\boldsymbol{b} - (\boldsymbol{b}\cdot\boldsymbol{c})\boldsymbol{a}$ as well as $\boldsymbol{n}\cdot\boldsymbol{n} = 1$ and that any derivative of the vector field is perpendicular to the vector field, i.e., $(\partial_i\boldsymbol{n})\cdot\boldsymbol{n} = 0$. This leads to

$$-[(\boldsymbol{v}+\boldsymbol{j})\cdot\boldsymbol{\nabla}]\boldsymbol{n}\times\boldsymbol{n} + \gamma\boldsymbol{H}_{\text{eff}} - \gamma\,(\boldsymbol{n}\cdot\boldsymbol{H}_{\text{eff}})\,\boldsymbol{n} + [(\alpha\boldsymbol{v}+\beta\boldsymbol{j})\cdot\boldsymbol{\nabla}]\boldsymbol{n} = 0. \tag{3.4}$$

As a last step we scalar multiply the equation by ∂_μ and integrate over the whole two-dimensional space. The derivative coordinate μ we use here represents either x or y. Therefore, both cases must be considered separately for the calculations in the following.

For this last step it is convenient to use component-wise notation. Equation (3.4) finally becomes

$$\begin{aligned} &-\sum_i (v_i + j_i) \int [(\partial_i \boldsymbol{n}) \times \boldsymbol{n}] \cdot (\partial_\mu \boldsymbol{n}) \, \mathrm{d}^2\boldsymbol{r} + \gamma \int \boldsymbol{H}_{\mathrm{eff}} \cdot (\partial_\mu \boldsymbol{n}) \, \mathrm{d}^2\boldsymbol{r} \\ &+ \sum_i (\alpha v_i + \beta j_i) \int (\partial_i \boldsymbol{n}) \cdot (\partial_\mu \boldsymbol{n}) \, \mathrm{d}^2\boldsymbol{r} = 0. \end{aligned} \tag{3.5}$$

By these few steps we, essentially, derived the Thiele equation. To understand Eq. (3.5) in a physical sense, we re-order the terms and write it in vector notation. In addition, we consider the vector field to form a rigid Skyrmion so that we can use the typical Skyrmion structure (see Sec. 2.4) to calculate the integrals. For the first integral in Eq. (3.5) it leads to

$$\int [(\partial_i \boldsymbol{n}) \times \boldsymbol{n}] \cdot (\partial_\mu \boldsymbol{n}) \, \mathrm{d}^2\boldsymbol{r} = \epsilon_{\mu i} Q, \tag{3.6}$$

with the anti-symmetric tensor $\epsilon_{\mu i} = -\epsilon_{i\mu} = -1$ and the topological quantum number Q as known from, e.g., Eq. (2.43). The other integral can be estimated using Skyrmion properties and yields

$$\int (\partial_i \boldsymbol{n}) \cdot (\partial_\mu \boldsymbol{n}) \, \mathrm{d}^2\boldsymbol{r} = \delta_{\mu,i} \mathcal{D}. \tag{3.7}$$

It vanishes for $\mu \neq i$ and is called the dissipation parameter $\mathcal{D}$ [see 71]. The resulting equation can, thus, be written as

$$\boldsymbol{G} \times \boldsymbol{v} + \alpha \mathcal{D} \boldsymbol{v} + \boldsymbol{F}_{\mathrm{int}} = \boldsymbol{F}_{\mathrm{ext}}, \tag{3.8}$$

with the gyrocoupling $\boldsymbol{G} = 4\pi Q \boldsymbol{z}$ [see 98], the previously mentioned dissipation strength $\mathcal{D}$ and the Skyrmion velocity $\boldsymbol{v}$. Equation (3.8) is our interpretation of the Thiele equation, which can be found in various publications (e.g., Refs. [50, 52, 67, 71, 98]). In this chapter we only consider the spin-polarized electric current as an external driving source, so that the external force is created by the current and reads

$$\boldsymbol{F}_{\mathrm{ext}} = -\boldsymbol{G} \times \boldsymbol{j} - \beta \mathcal{D} \boldsymbol{j}. \tag{3.9}$$

The force $\boldsymbol{F}_{\mathrm{int}}$ represents the internal force of the system and its components are due to the choice of μ,

$$\boldsymbol{F}_{\mathrm{int}} = \gamma \sum_{\mu=x,y} \int \boldsymbol{H}_{\mathrm{eff}} \cdot (\partial_\mu \boldsymbol{n}) \, \mathrm{d}^2\boldsymbol{r} \; \boldsymbol{e}_\mu. \tag{3.10}$$

This internal force would, in general, account for inner modes, deformation of the Skyrmion or coupling with excitations such as magnons. For rigid ferromagnetic Skyrmions, however, this force vanishes. It will play a role later when we consider antiferromagnetic Skyrmions. Therefore, in the rigid Skyrmion approximation ferromagnetic Skyrmions only move when an external force, for instance in the form of an electric current, is applied and stops moving when the external force is switched off. Because of this it is commonly assumed that ferromagnetic Skyrmions are mass-less [67]. We note that the vanishing mass of

a ferromagnetic Skyrmion is a controversial topic. While Komineas and Papanicolaou showed, using the topological charge density, that a ferromagnetic Skyrmion exhibits no mass [82], experiments suggest that Skyrmions exhibits a finite mass when excited [99]. In Ref. [100], the authors introduced the Skyrmion mass as a phenomenological term in the Thiele equation to account for deviations observed between the equation and their simulation results. They conclude that a Skyrmion bubble behaves as a massive object where the mass is accounted to small dynamical deformations of the Skyrmion bubble. Furthermore in Ref. [101] the authors have identified a dynamical mass for the ferromagnetic Skyrmion in motion by taking into account a direct coupling between Skyrmion motion and the correspondingly excited magnon. In this thesis, however, we approximate the Skyrmion as a rigid quasi-particle and neglect all inner modes and deformations so that we can assume a vanishing mass for ferromagnetic Skyrmions. Since we here only investigate traveling Skyrmions, it is valid to consider the ferromagnetic Skyrmion to be mass-less (cf. Ref. [102]).

In this thesis, we study Skyrmions formed in an antiferromagnetic system. Since we are focusing on antiferromagnets that can be separated into two ferromagnetic sublattices, it is reasonable to assume that a separate Thiele equation can be derived for each sublattice. Therefore, we consider two equations of the form of Eq. (3.8) assuming a common Gilbert damping parameter α [103]. The sublattice Thiele equations are

$$\begin{aligned} \boldsymbol{G}^A \times \boldsymbol{v}^A + \alpha \mathcal{D}^A \boldsymbol{v}^A + \boldsymbol{F}^A_{\text{int}} &= \boldsymbol{F}^A_{\text{ext}}, \\ \boldsymbol{G}^B \times \boldsymbol{v}^B + \alpha \mathcal{D}^B \boldsymbol{v}^B + \boldsymbol{F}^B_{\text{int}} &= \boldsymbol{F}^B_{\text{ext}}, \end{aligned} \tag{3.11}$$

where the superscript denotes the sublattice. The vector fields of both sublattices are considered to form a typical Skyrmion each. As explained in Sec. 2.5, the sublattice constituents of the AFM Skyrmion are, in the continuum approach, two identical anti-parallel FM sublattice Skyrmions. Therefore we assume, for the rigid Skyrmion approximation, two identical anti-parallel sublattice Skyrmions in the Thiele equations of Eq. (3.11). By this, it is possible to identify the relations $\boldsymbol{G}^A = -\boldsymbol{G}^B$, because $Q^A = -Q^B$ (see Sec. 2.4), and $\mathcal{D}^A = \mathcal{D}^B$. For studying the inner mechanics of antiferromagnetic Skyrmion dynamics, we consider no external driving force (we will return to this below) and regard sublattice A as reference, i.e., $Q = Q^A$. The sublattice Skyrmion Thiele equation becomes

$$\begin{aligned} \boldsymbol{G} \times \boldsymbol{v}^A + \alpha \mathcal{D} \boldsymbol{v}^A + \boldsymbol{F}^A_{\text{int}} &= 0, \\ -\boldsymbol{G} \times \boldsymbol{v}^B + \alpha \mathcal{D} \boldsymbol{v}^B + \boldsymbol{F}^B_{\text{int}} &= 0. \end{aligned} \tag{3.12}$$

As one can see here, the internal force in the sublattices $\boldsymbol{F}^{(A/B)}_{\text{int}}$ plays a crucial role for AFM Skyrmion dynamics. To investigate this force further, the energy of the antiferromagnetic system must be regarded. The energy considered in this chapter is inspired by Ref. [31]. It is expressed in terms of the continuous vector fields $\boldsymbol{a}$ and $\boldsymbol{b}$ of the two different sublattices

A and B, assuming unit length for both. This energy is a universal description and covers, depending on the choice of parameters, various kinds of antiferromagnetic systems. More details can be found in Sec. 2.5. The energy term reads

$$\begin{aligned} W = \int \mathrm{d}^2\boldsymbol{r}\big\{ & \frac{\lambda}{2}\boldsymbol{a}\boldsymbol{b} + \frac{A'}{2}\sum_{\mu\in\{x,y\}}\left[(\partial_\mu \boldsymbol{a})^2 + (\partial_\mu \boldsymbol{b})^2\right] \\ & + A\sum_{\mu\in\{x,y\}}\left[(\partial_\mu \boldsymbol{a})\,(\partial_\mu \boldsymbol{b})\right] + D\boldsymbol{a}\cdot(\boldsymbol{\nabla}\times\boldsymbol{b}) \\ & + \frac{D'}{2}\left[\boldsymbol{a}\cdot(\boldsymbol{\nabla}\times\boldsymbol{a}) + \boldsymbol{b}\cdot(\boldsymbol{\nabla}\times\boldsymbol{b})\right] - \frac{K'}{2}(a_z^2 + b_z^2) \\ & - K a_z b_z\big\}. \end{aligned} \tag{3.13}$$

The energy exhibits a specific structure. It consists of terms which are pair-wise coupled vector fields. These terms separate into pairs of the same sublattice, which we call *intra-sublattice* terms, and pairs of different sublattices which we call *inter-sublattice* terms. The former are of the same structure as the energy of a ferromagnet and thus could be denoted as $W_{\mathrm{FM}}[\boldsymbol{a},\boldsymbol{a}]$ and $W_{\mathrm{FM}}[\boldsymbol{b},\boldsymbol{b}]$. For those[1] it is obvious that commuting the entries does not alter the energy. The inter-sublattice terms can be interpreted as effective coupling between the sublattices. Therefore, we will denote them as antiferromagnetic coupling terms $W_c[\boldsymbol{a},\boldsymbol{b}]$. In Sec. 2.5 it is mentioned that the energy of Eq. (3.13) is invariant under sublattice exchange. Consequently, the coupling energy does not alter when commuting the sublattices $W_c[\boldsymbol{a},\boldsymbol{b}] = W_c[\boldsymbol{b},\boldsymbol{a}]$. The total energy, Eq. (3.13), consists of those three parts and can be written as

$$W = W_{\mathrm{FM}}[\boldsymbol{a},\boldsymbol{a}] + W_{\mathrm{FM}}[\boldsymbol{b},\boldsymbol{b}] + W_c[\boldsymbol{a},\boldsymbol{b}]. \tag{3.14}$$

This convention is shown here to illustrate the separation of energy into intra- and inter-sublattice terms. Additionally, it is employed in Ref. [51] to demonstrate the universality of the formalism of sublattice Skyrmion displacement, whereby the energy can be adapted as long as it fulfills certain conditions. Nevertheless, in this chapter, we will adhere to the notation of the effective field with an explicit energy given in Eq. (3.13). We assume that the effective field acting on one sublattice can be calculated using the energy, as it is done in the ferromagnetic case [51], according to Eq. (2.36). Setting $\hbar = 1$ and considering the lattice constant only as a unit, i.e., $d = 1$, the effective fields for the respective sublattices are, denoted by a superscript,

$$\begin{aligned} \boldsymbol{H}_{\mathrm{eff}}^{A} &= -\frac{1}{\gamma}\frac{\partial W}{\partial \boldsymbol{a}}, \\ \boldsymbol{H}_{\mathrm{eff}}^{B} &= -\frac{1}{\gamma}\frac{\partial W}{\partial \boldsymbol{b}}. \end{aligned} \tag{3.15}$$

[1] This notation includes all terms related to the vector field, such as a_z and $\partial_\mu \boldsymbol{a}$.

Regarding the energy from Eq. (3.13), the explicit expressions for the effective fields calculate to

$$\begin{aligned}\gamma \boldsymbol{H}^A_{\text{eff}} =& -\frac{\lambda}{2}\boldsymbol{b} + A\boldsymbol{\nabla}^2\boldsymbol{b} - D(\boldsymbol{\nabla}\times\boldsymbol{b}) + Kb_z\boldsymbol{z} \\ &+ A'\boldsymbol{\nabla}^2\boldsymbol{a} - D'(\boldsymbol{\nabla}\times\boldsymbol{a}) + K'a_z\boldsymbol{z}, \\ \gamma \boldsymbol{H}^B_{\text{eff}} =& -\frac{\lambda}{2}\boldsymbol{a} + A\boldsymbol{\nabla}^2\boldsymbol{a} - D(\boldsymbol{\nabla}\times\boldsymbol{a}) + Ka_z\boldsymbol{z} \\ &+ A'\boldsymbol{\nabla}^2\boldsymbol{b} - D'(\boldsymbol{\nabla}\times\boldsymbol{b}) + K'b_z\boldsymbol{z}.\end{aligned} \tag{3.16}$$

As a consequence of the structure of the energy, the effective fields is the sum of two types of terms. One type will be called the intra-sublattice field [51] since it consists only of terms from the same sublattice. It includes all terms regarding the vector field $\boldsymbol{a}$ in $\boldsymbol{H}^A_{\text{eff}}$ and the same for sublattice B. The other type is the inter-sublattice field [51]. This type only consists of terms stemming from the respective *other* sublattice, i.e., terms of $\boldsymbol{b}$ in $\boldsymbol{H}^A_{\text{eff}}$. That means concretely for, e.g., sublattice A

$$\begin{aligned}\gamma \boldsymbol{H}^A_{\text{inter}} &= -\frac{\lambda}{2}\boldsymbol{b} + A\boldsymbol{\nabla}^2\boldsymbol{b} - D(\boldsymbol{\nabla}\times\boldsymbol{b}) + Kb_z\boldsymbol{z}, \\ \gamma \boldsymbol{H}^A_{\text{intra}} &= A'\boldsymbol{\nabla}^2\boldsymbol{a} - D'(\boldsymbol{\nabla}\times\boldsymbol{a}) + K'a_z\boldsymbol{z}.\end{aligned} \tag{3.17}$$

The internal forces, see Eq. (3.10), are thus calculated by

$$\begin{aligned}\boldsymbol{F}^A_{\text{int}} &= \gamma \sum_{\mu=x,y} \int (\partial_\mu \boldsymbol{a}) \cdot \left(\boldsymbol{H}^A_{\text{intra}} + \boldsymbol{H}^A_{\text{inter}}\right)\, \mathrm{d}^2\boldsymbol{r}\; \boldsymbol{e}_\mu, \\ \boldsymbol{F}^B_{\text{int}} &= \gamma \sum_{\mu=x,y} \int (\partial_\mu \boldsymbol{b}) \cdot \left(\boldsymbol{H}^B_{\text{intra}} + \boldsymbol{H}^B_{\text{inter}}\right)\, \mathrm{d}^2\boldsymbol{r}\; \boldsymbol{e}_\mu.\end{aligned} \tag{3.18}$$

As it was mentioned previously and also shown in the Appendix B, a rigid FM Skyrmion does not exhibit an internal force. Since the intra-sublattice fields are essentially the inner ferromagnetic sublattice interaction, the terms $\int(\partial_\mu \boldsymbol{a})\cdot\boldsymbol{H}^A_{\text{intra}}\,\mathrm{d}^2\boldsymbol{r}$ and $\int(\partial_\mu \boldsymbol{b})\cdot\boldsymbol{H}^B_{\text{intra}}\,\mathrm{d}^2\boldsymbol{r}$ vanish. This leaves only the inter-sublattice effective field coupled with $(\partial_\mu \boldsymbol{a})$ or $(\partial_\mu \boldsymbol{b})$, respectively. Since the inter-sublattice field only depends on the respective other sublattice, the internal force consists of pairs of two sublattice fields. Considering explicitly the effective fields from Eq. (3.16), the force reads

$$\begin{aligned}\boldsymbol{F}^A_{\text{int}} &= \sum_{\mu} \int (\partial_\mu \boldsymbol{a}) \cdot \left(-\frac{\lambda}{2}\boldsymbol{b} + A\boldsymbol{\nabla}^2\boldsymbol{b} - D(\boldsymbol{\nabla}\times\boldsymbol{b}) + Kb_z\boldsymbol{z}\right)\, \mathrm{d}^2\boldsymbol{r}\; \boldsymbol{e}_\mu, \\ \boldsymbol{F}^B_{\text{int}} &= \sum_{\mu} \int (\partial_\mu \boldsymbol{b}) \cdot \left(-\frac{\lambda}{2}\boldsymbol{a} + A\boldsymbol{\nabla}^2\boldsymbol{a} - D(\boldsymbol{\nabla}\times\boldsymbol{a}) + Ka_z\boldsymbol{z}\right)\, \mathrm{d}^2\boldsymbol{r}\; \boldsymbol{e}_\mu.\end{aligned} \tag{3.19}$$

Integrating by parts one can show that $\boldsymbol{F}^A_{\text{int}} = -\boldsymbol{F}^B_{\text{int}}$. This result shows that one sublattice Skyrmion applies a force on the respective other sublattice Skyrmion. It also confirms the intuition that in a system of two effectively coupled sublattice skyrmions, the principle of *actio est reactio* still holds. While this principle for AFM Skyrmions is derived in this

thesis, in Ref. [104], it serves as a fundamental assumption for addressing Skyrmion motion in a bilayer synthetic antiferromagnet. Again, using sublattice A as reference, we will use the convention $\boldsymbol{F}_{\text{int}} = \boldsymbol{F}^A_{\text{int}}$, so that Eq. (3.12) then becomes

$$\begin{aligned} \boldsymbol{G} \times \boldsymbol{v}^A + \alpha \mathcal{D} \boldsymbol{v}^A + \boldsymbol{F}_{\text{int}} = 0, \\ -\boldsymbol{G} \times \boldsymbol{v}^B + \alpha \mathcal{D} \boldsymbol{v}^B - \boldsymbol{F}_{\text{int}} = 0. \end{aligned} \tag{3.20}$$

In the non-damped case ($\alpha = 0$) one can immediately see that the velocities of the two sublattice Skyrmions are equal $\boldsymbol{v}^A = \boldsymbol{v}^B$ and perpendicular to the internal force $\boldsymbol{v} \perp \boldsymbol{F}_{\text{int}}$. To investigate this further, especially for realistic scenarios, we focus on the interaction between the two sublattice Skyrmions.

3.2. Introducing sublattice skyrmion displacement

In this Section, we show that the taking the relative position of the two sublattice Skyrmions into account, leads to exciting results regarding the dynamics of the antiferromagnetic Skyrmion. We assume that a small displacement $\boldsymbol{\delta} = (\delta_x, \delta_y)$ between the sublattice Skyrmions creates the internal force $\boldsymbol{F}_{\text{int}}$. Displacing the sublattice constituents would, in reality, deform the Skyrmion. However, we treat each sublattice Skyrmion as rigid and maintain the typical FM Skyrmion form. Therefore, it is important to note that this is only an approximation. By assuming small displacements between the sublattice Skyrmions we can express $\boldsymbol{a}$ in terms of $\boldsymbol{b}$ and vice versa via Taylor expansion. Considering $\boldsymbol{\delta}$ as the displacement of B relative to A, it is also valid to consider $-\boldsymbol{\delta}$ as displacement of A relative to B. This yields

$$\begin{aligned} \boldsymbol{a}(\boldsymbol{r}) &\approx -\boldsymbol{b} + \sum_{\mu \in \{x,y\}} \delta_\mu (\partial_\mu \boldsymbol{b}) - \frac{1}{2} \sum_{\mu,\nu} \delta_\mu \delta_\nu (\partial_\mu \partial_\nu \boldsymbol{b}), \\ \boldsymbol{b}(\boldsymbol{r}) &\approx -\boldsymbol{a} - \sum_{\mu \in \{x,y\}} \delta_\mu (\partial_\mu \boldsymbol{a}) - \frac{1}{2} \sum_{\mu,\nu} \delta_\mu \delta_\nu (\partial_\mu \partial_\nu \boldsymbol{a}). \end{aligned} \tag{3.21}$$

These approximations enable us to determine the integrals where two different sublattice vector fields are coupled. The internal force, for instance, consists of terms which contain pairs of $\boldsymbol{a}$ and $\boldsymbol{b}$, see Eq. (3.19). Plugging the approximation Eq. (3.21) into this, it only depends on a single sublattice vector field. Since each sublattice vector field forms a FM Skyrmion, we can use the Skyrmion properties shown in Sec. 2.4 to estimate the force. The force $\boldsymbol{F}^A_{\text{int}}$ can be calculated as

$$\boldsymbol{F}^A_{\text{int}} = \gamma \sum_{i=x,y} \int \boldsymbol{H}^A_{\text{inter}} \cdot \partial_i \left(-\boldsymbol{b} + \sum_{\mu=x,y} \delta_\mu (\partial_\mu \boldsymbol{b}) - \frac{1}{2} \sum_{\mu,\nu} \delta_\mu \delta_\nu (\partial_\mu \partial_\nu \boldsymbol{b}) \right) \mathrm{d}^2\boldsymbol{r}\ \boldsymbol{e}_i, \tag{3.22}$$

where $\boldsymbol{H}^A_{\text{inter}}$ only consists of terms concerning $\boldsymbol{b}$. The explicit calculation of the integrals is outsourced to the Appendix B. There it is shown that the first and the third term vanish,

i.e.,

$$\int \boldsymbol{H}^A_{\text{inter}} \cdot \partial_i \boldsymbol{b} \, \mathrm{d}^2\boldsymbol{r} = 0 \;\text{ and }\; \int \boldsymbol{H}^A_{\text{inter}} \cdot \partial_i \partial_\mu \partial_\mu \boldsymbol{b} \, \mathrm{d}^2\boldsymbol{r} = 0. \tag{3.23}$$

Furthermore, it is shown that the second term vanishes if $i \neq \mu$, but shows equal results independent whether i is x or y as long as $i = \mu$. Therefore, we define a parameter Λ which absorbs the integral in such a form that

$$\gamma \int \boldsymbol{H}^A_{\text{inter}} \cdot \partial_i \partial_\mu \boldsymbol{b} \, \mathrm{d}^2\boldsymbol{r} = \delta_{i,\mu}\Lambda, \tag{3.24}$$

where $\delta_{i,\mu}$ is the Kronecker delta. Consequently, the internal force amounts to

$$\boldsymbol{F}^A_{\text{int}} = \boldsymbol{\delta}\Lambda, \tag{3.25}$$

where $\Lambda \in \mathbb{R}$ is a constant depending on the Skyrmion structure and system parameters. Regarding Eq. (3.20) the sublattice Thiele equations now become

$$\begin{aligned} \boldsymbol{G} \times \boldsymbol{v}^A + \alpha\mathcal{D}\boldsymbol{v}^A + \boldsymbol{\delta}\Lambda = 0 \\ -\boldsymbol{G} \times \boldsymbol{v}^B + \alpha\mathcal{D}\boldsymbol{v}^B - \boldsymbol{\delta}\Lambda = 0. \end{aligned} \tag{3.26}$$

Assuming that the sublattice Skyrmions are initially displaced by $\boldsymbol{\delta}_0$ as a result of a previous acceleration in a damping-free system ($\alpha = 0$), we can conclude that the Skyrmion velocity is

$$\boldsymbol{v} = \boldsymbol{z} \times \frac{\Lambda}{4\pi Q}\boldsymbol{\delta}_0. \tag{3.27}$$

Since the Skyrmion velocity is perpendicular to the displacement, the system is not able to alter the distance between the sublattice Skyrmions. Thus, the AFM Skyrmion travels with a constant velocity [51]. That means in a non-damped system an AFM Skyrmion remains in a steady motion once accelerated. Next, we consider an initially accelerated Skyrmion in a more realistic setting, namely with non-vanishing damping $\alpha > 0$. Equation (3.26) can then be re-written to

$$\begin{aligned} \boldsymbol{G} \times (\boldsymbol{v}^A - \boldsymbol{v}^B) + \alpha\mathcal{D}(\boldsymbol{v}^A + \boldsymbol{v}^B) = 0, \\ \boldsymbol{G} \times (\boldsymbol{v}^A + \boldsymbol{v}^B) + \alpha\mathcal{D}(\boldsymbol{v}^A - \boldsymbol{v}^B) + 2\boldsymbol{\delta}\Lambda = 0. \end{aligned} \tag{3.28}$$

Here it is convenient to use center-of-mass (c. o. m.) coordinates. The resulting velocity of the system $\boldsymbol{v} = (\boldsymbol{v}^A + \boldsymbol{v}^B)/2$ is the real velocity of the AFM Skyrmion, while the relative velocity can be seen as the change of displacement in time $\partial_t\boldsymbol{\delta} = \boldsymbol{v}^A - \boldsymbol{v}^B$. Applying these considerations, Eq. (3.28) can be re-written as

$$\begin{aligned} \boldsymbol{G} \times \partial_t\boldsymbol{\delta} + 2\alpha\mathcal{D}\boldsymbol{v} = 0, \\ \frac{(4\pi Q)^2}{\alpha\mathcal{D}}\partial_t\boldsymbol{\delta} + \alpha\mathcal{D}\partial_t\boldsymbol{\delta} + 2\Lambda\boldsymbol{\delta} = 0, \end{aligned} \tag{3.29}$$

where we used that the gyro-coupling vector is perpendicular to each possible displacement in the lattice since it points in z direction, $\boldsymbol{G} \perp \partial_t \boldsymbol{\delta}$. The second line of Eq. (3.29) is an ordinary differential equation (ODE) which can be easily solved considering an initial displacement $\boldsymbol{\delta}_0$. Additionally, using that we only consider Skyrmions of quantum number $Q = \pm 1$ the ODE is solved by

$$\boldsymbol{\delta}(t) = \boldsymbol{\delta}_0 \exp\left(-\frac{2\alpha\mathcal{D}\Lambda}{16\pi^2 + \alpha^2\mathcal{D}^2}t\right). \tag{3.30}$$

In the sense of the Landau-Lifshitz-Gilbert equation it is common to assume the damping parameter α small. Therefore, we will assume $16\pi^2 \gg \alpha^2\mathcal{D}^2$ and neglect the quadratic order damping. The AFM Skyrmion velocity in dependence of the time, calculated from the first line of Eq. (3.29), is

$$\boldsymbol{v}(t) = \boldsymbol{z} \times \frac{\Lambda}{4\pi Q}\boldsymbol{\delta}_0 \exp\left(-\frac{\alpha\mathcal{D}\Lambda}{8\pi^2}t\right), \tag{3.31}$$

where we consider $Q = \pm 1$. One can see that the initial Skyrmion velocity $\boldsymbol{v}_0 = \boldsymbol{z} \times \frac{\Lambda}{4\pi Q}\boldsymbol{\delta}_0$ can be identified using Eq. (3.27). Furthermore, Equation (3.31) is precisely the solution of the equation of motion of a damped classical particle $m\ddot{x} + \Gamma\dot{x} = 0$ with an initial velocity v_0 [51]. By this we can identify the ratio of mass and damping to $\frac{\Gamma}{m} = \frac{\alpha\mathcal{D}\Lambda}{8\pi^2}$. The mass and damping can not be determined separately using only this equation of motion, leaving the definition of the mass term ambiguous. However, Ref. [104] suggests[2] that the mass of an antiferromagnetic Skyrmion is

$$m = \frac{16\pi^2}{\Lambda}. \tag{3.32}$$

Consequently, the damping can be identified with $\Gamma = 2\alpha\mathcal{D}$ and is proportional to the Gilbert damping. To summarize, by assuming a slightly displaced rigid sublattice Skyrmion we are able to show that the antiferromagnetic Skyrmion, which is a localized deformation of the magnetic vector field, precisely moves as a classical particle with a finite mass m and damping Γ. The dynamics are only based on the LLG equation, which describe the precession of a vector around an effective field and the classical damping Γ is connected to the Gilbert damping α.

Influence on the energy

An intriguing question is how the displacement of the two sublattice Skyrmions influences the energy. To answer this it is convenient to write the energy in Eq. (3.13) in terms of vector fields and their respective effective fields. With Eqs. (3.16) and (3.17) the energy

[2] Indeed, if one identifies the displacement with the velocity, the first line of Eq. (3.29) looks essentially as the classical particle equation of motion with damping $2\alpha\mathcal{D}$.

can be written as

$$W = -\gamma \int \mathrm{d}^2\boldsymbol{r} \left(\frac{1}{2}\boldsymbol{a} \cdot \boldsymbol{H}^A_{\text{intra}} + \frac{1}{2}\boldsymbol{b} \cdot \boldsymbol{H}^B_{\text{intra}} + \boldsymbol{a} \cdot \boldsymbol{H}^A_{\text{inter}} \right). \tag{3.33}$$

The first two terms in the integral only consists of terms of the same sublattice. Since the energy excitation is only due to the displacement between the sublattice Skyrmions (while the Skyrmions itself remain rigid), it does not affect the energy of a single sublattice. Thus, the first two terms are the energy of a stationary FM Skyrmion W^0_{FM}. That means only the third term[3] is of interest. Applying the Taylor expansion from Eq. (3.21) to this term yields

$$\int \boldsymbol{a} \cdot \boldsymbol{H}^A_{\text{inter}} \, \mathrm{d}^2\boldsymbol{r} \approx \int \left(-\boldsymbol{b} + \sum_{\mu \in \{x,y\}} \delta_\mu(\partial_\mu \boldsymbol{b}) - \frac{1}{2} \sum_{\mu,\nu} \delta_\mu \delta_\nu (\partial_\mu \partial_\nu \boldsymbol{b}) \right) \cdot \boldsymbol{H}^A_{\text{inter}} \, \mathrm{d}^2\boldsymbol{r}. \tag{3.34}$$

The first term is the coupling of vector field $\boldsymbol{b}$ with the inter-sublattice effective field acting on sublattice A. This is simply the coupling energy of a stationary AFM Skyrmion since the two sublattice vector fields are perfectly anti-parallel in a resting AFM Skyrmion without external influence. Regarding Eq. (3.23), the second term in Eq. (3.34) vanishes. By this, the energy becomes

$$W = W^0_{\text{FM}} + W^0_{\text{FM}} + W^0_c + \gamma \int \frac{1}{2} \sum_{\mu,\nu} \delta_\mu \delta_\nu (\partial_\mu \partial_\nu \boldsymbol{b}) \cdot \boldsymbol{H}^A_{\text{inter}} \, \mathrm{d}^2\boldsymbol{r}. \tag{3.35}$$

The first three terms add to the energy of a resting AFM Skyrmion, which we consider in this scenario as the ground state energy W^0_{AFM}. The last term can be expressed by utilizing Eq. (3.24) which introduces the parameter Λ as it is used for the internal force. Viewing the displacement as a vector $\boldsymbol{\delta}$, the energy can be written as

$$W = W^0_{\text{AFM}} + \frac{1}{2}\Lambda |\boldsymbol{\delta}|^2. \tag{3.36}$$

It appears that the sublattice Skyrmion displacement creates a harmonic potential in the energy. That the sublattice Skyrmions are effectively coupled by a harmonic potential was only found recently [51, 104] and reminds of the potential energy of a linear spring with the spring constant Λ. Furthermore, by calculating the force one sublattice Skyrmion exerts onto the other assuming their coupling via the potential $\boldsymbol{F} = -\partial W / \partial \boldsymbol{\delta}$, it turns out that it is exactly the internal force from Eq. (3.25). Even though it seems trivial on the first glance, the force in Eq. (3.25) was identified by using Thiele's approach to the LLG equation while the very same force is the result of assuming two sublattice Skyrmions classically coupled by the previously derived potential. However, looking at the Skyrmion dynamics there is a fundamental difference to the dynamics of a harmonic oscillator. Due to the gyro-coupling,

[3] The choice of writing the energy as in Eq. (3.33) is convenient for the calculations. Due to symmetry it is also possible to write it in a symmetric form $W = -\gamma \int \left(\frac{1}{2}\boldsymbol{a} \cdot \boldsymbol{H}^A_{\text{eff}} + \frac{1}{2}\boldsymbol{b} \cdot \boldsymbol{H}^B_{\text{eff}} \right) \mathrm{d}^2\boldsymbol{r}$, where it becomes more clear how the energy is constructed.

see Eq. (3.26), the Skyrmion velocity is perpendicular to the acting force. That means the resulting Skyrmion motion is perpendicular to the displacement, so that the gap between the sublattice Skyrmions is not closed. Consequently, the displacement induces a constant velocity. If we relate the displacement with the Skyrmion velocity as in Eq. (3.27) and use the effective mass of the Skyrmion from Eq. (3.32), the energy from Eq. (3.36) yields

$$W = W^0_{\mathrm{AFM}} + \frac{1}{2} m |\boldsymbol{v}|^2. \tag{3.37}$$

Therefore, the excitation energy can be seen as the kinetic energy of the antiferromagnetic Skyrmion. This is yet another result showing how precisely the antiferromagnetic Skyrmion fits into the analogy of a classical particle.

3.3. Applying external electric current

A typical way of driving Skyrmions, both ferromagnetic [21] and antiferromagnetic [27] ones, is to apply spin polarized current. The possibility to move Skyrmions by electric current is a main argument for their technological relevance [105]. In contrast to the description of current driven antiferromagnetic structures in the sense of Néel- and magnetization vectors [27, 106], in this thesis we explicitly study the sublattice kinetics leading to the current-driven Skyrmion motion. To this end, we assume an effective spin-polarized current applied on each sublattice [103]. Without loss of generality regarding the physical realization, we assume the presence of independent currents $\boldsymbol{j}^A$ and $\boldsymbol{j}^B$. This assumption is based on the structure of the equation of motion and will be further discussed later. Consequently, each sublattice experiences an external force $\boldsymbol{F}^A_{\mathrm{ext}}$ and $\boldsymbol{F}^B_{\mathrm{ext}}$, respectively, in accordance with Eq. (3.9). The coupled Thiele equations for the sublattice Skyrmions, see Eq. (3.26), become

$$\begin{aligned} \boldsymbol{G} \times \boldsymbol{v}^A + \alpha \mathcal{D} \boldsymbol{v}^A + \boldsymbol{\delta}\Lambda &= -\boldsymbol{G} \times \boldsymbol{j}^A - \beta \mathcal{D} \boldsymbol{j}^A, \\ -\boldsymbol{G} \times \boldsymbol{v}^B + \alpha \mathcal{D} \boldsymbol{v}^B - \boldsymbol{\delta}\Lambda &= \boldsymbol{G} \times \boldsymbol{j}^B - \beta \mathcal{D} \boldsymbol{j}^B, \end{aligned} \tag{3.38}$$

where $\mp \boldsymbol{G} \times \boldsymbol{j}^{(A/B)} - \beta \mathcal{D} \boldsymbol{j}^{(A/B)} = \boldsymbol{F}^{(A/B)}_{\mathrm{extern}}$ is the external force applied to the corresponding sublattice created by the electric current. Regarding only one sublattice one can see that the external force, created by the electric current $\boldsymbol{j}$, consists of two parts. One of them is perpendicular to that current direction, $\boldsymbol{G} \times \boldsymbol{j}$, and the other is parallel to the current direction and scales with the non-adiabatic parameter β. This leads to the Skyrmion Hall effect for ferromagnetic current-driven Skyrmions which is well-studied in the theoretical framework (see, e.g., [21]) as well as in experiments (see, e.g., [53]). Note that the external forces can, in principle, also be created by other external sources (e.g., spin waves, magnetic fields, geometric confinements).

Next, we define two effective electric currents $\boldsymbol{j}^+ := \boldsymbol{j}^A + \boldsymbol{j}^B$ and $\boldsymbol{j}^- := \boldsymbol{j}^A - \boldsymbol{j}^B$ which describe the two sublattice currents in an efficient way. Note that with the introduction

of $\boldsymbol{j}^-$, we explicitly choose sublattice A as a reference. Using these effective currents Eq. (3.38) can be transformed to

$$\begin{aligned} \boldsymbol{G} \times \partial_t \boldsymbol{\delta} + 2\alpha\mathcal{D}\boldsymbol{v} &= \boldsymbol{F}^+_{\text{extern}}, \\ 2\boldsymbol{G} \times \boldsymbol{v} + \alpha\mathcal{D}\partial_t\boldsymbol{\delta} + 2\Lambda\boldsymbol{\delta} &= \boldsymbol{F}^-_{\text{extern}}, \end{aligned} \tag{3.39}$$

with the effective external forces

$$\begin{aligned} \boldsymbol{F}^+_{\text{extern}} &= -\boldsymbol{G} \times \boldsymbol{j}^- - \beta\mathcal{D}\boldsymbol{j}^+, \\ \boldsymbol{F}^-_{\text{extern}} &= -\boldsymbol{G} \times \boldsymbol{j}^+ - \beta\mathcal{D}\boldsymbol{j}^-. \end{aligned} \tag{3.40}$$

In order to get the time dependent behavior of the displacement $\boldsymbol{\delta}$, we plug $\boldsymbol{v} = (-\boldsymbol{G} \times \partial_t\boldsymbol{\delta} + \boldsymbol{F}^+_{\text{extern}})/(2\alpha\mathcal{D})$, derived from the first line of Eq. (3.39), into the second line. By this, we derive the inhomogeneous differential equation for $\boldsymbol{\delta}$, similar to Eq. (3.29), yielding

$$\frac{16\pi^2}{\alpha\mathcal{D}}\partial_t\boldsymbol{\delta} + 2\Lambda\boldsymbol{\delta} = \boldsymbol{F}^-_{\text{extern}} + \frac{1}{\alpha\mathcal{D}}\boldsymbol{F}^+_{\text{extern}} \times \boldsymbol{G}. \tag{3.41}$$

We assume constant external forces which act on an initially resting Skyrmion, i.e., the initial displacement is zero $\boldsymbol{\delta}(t=0) = 0$. Furthermore, we define an effective displacement force $\tilde{\boldsymbol{F}}$, so that the ODE can be solved by

$$\begin{aligned} \boldsymbol{\delta}(t) &= \frac{1}{2\Lambda}\tilde{\boldsymbol{F}}\left(\exp\left[-\frac{\Lambda\alpha\mathcal{D}}{8\pi^2}t\right] - 1\right), \\ \tilde{\boldsymbol{F}} &= \boldsymbol{F}^-_{\text{extern}} + \frac{1}{\alpha\mathcal{D}}\boldsymbol{F}^+_{\text{extern}} \times \boldsymbol{G}. \end{aligned} \tag{3.42}$$

At this point it is instructive to consider the implications of Eq. (3.42). This equation not only describes the time-dependent behavior of the sublattice Skyrmion displacement, but also plays an important role for understanding the underlying Skyrmion mechanics in our analysis. For the sake of simplicity we start with the assumptions of a vanishing damping $\alpha = 0$. To satisfy this assumption we have to apply the limit $\alpha \to 0$ to Eq. (3.42). Doing so leads to a displacement $\boldsymbol{\delta}(t) = \frac{t}{16\pi^2}\boldsymbol{G} \times \boldsymbol{F}^+_{\text{extern}}$ which is independent on $\boldsymbol{F}^-_{\text{extern}}$. To support the subsequent discussion, Fig. 3.1 presents a sketch of the two sublattice Skyrmions, highlighting the acting forces and their resulting velocities. The displacement $\boldsymbol{\delta}$ is displayed in a highly exaggerated manner to enhance visibility and the sketch also depicts the case of a vanishing damping $\alpha = 0$. The left picture shows the case where the two sublattice forces act in the same direction with equal intensity. Therefore, it depicts the case $\boldsymbol{F}^+_{\text{extern}} \neq 0$ and $\boldsymbol{F}^-_{\text{extern}} = 0$. The force $\boldsymbol{F}^+_{\text{extern}}$ is the total force of the sublattice forces acting on each sublattice. However, due to the gyro-coupling, $\boldsymbol{G} \times \boldsymbol{v}$, the resulting Skyrmion motion is rotated by 90 degrees around the z axis, see Eq. (3.8). Since the gyro-coupling vector of sublattice A is in the opposite direction of sublattice B, $\boldsymbol{G}_A = -\boldsymbol{G}_B$, the resulting Skyrmion motion in sublattice A is rotated in the other direction than the motion in sublattice B. Consequently, the resulting Skyrmion motion of

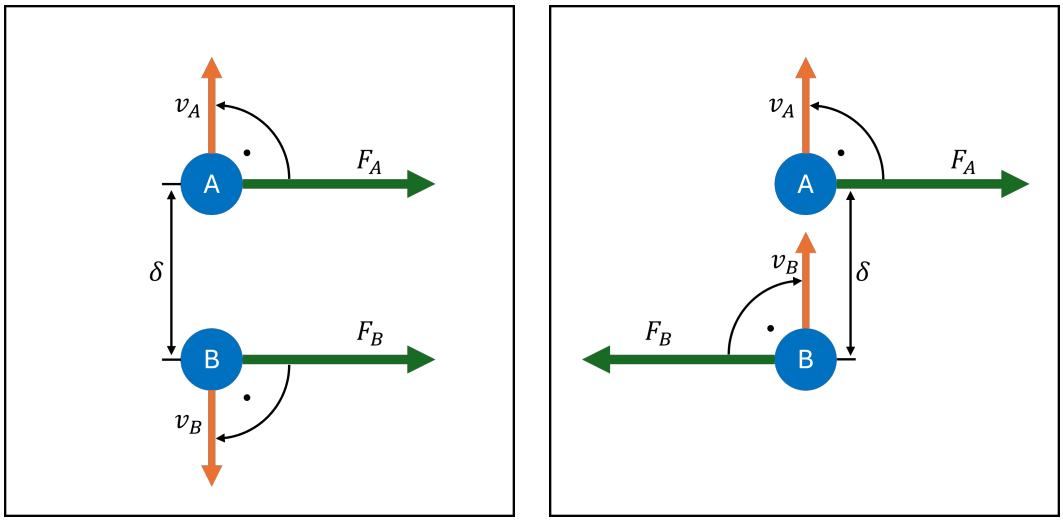

Figure 3.1.: Sketch of the two sublattice Skyrmions (blue filled circles), highlighting the acting forces (green arrows) and their resulting velocities (orange arrows). The displacement $\boldsymbol{\delta}$ is exaggerated for clarity, emphasizing the distance between the two filled circles. In reality, the sublattice Skyrmions are expected to largely overlap. Shown are the two cases discussed in the main text.
Left: Only aligning sublattice forces, i.e. $\boldsymbol{F}^{+}_{\text{extern}} \neq 0$ while $\boldsymbol{F}^{-}_{\text{extern}} = 0$ are considered. Right: Only counter-acting forces, i.e. $\boldsymbol{F}^{+}_{\text{extern}} = 0$ and $\boldsymbol{F}^{-}_{\text{extern}} \neq 0$ are considered.

the sublattice Skyrmion A is in the opposite direction of the resulting motion of sublattice Skyrmion B while both are perpendicular to the effective force $\boldsymbol{F}^{+}_{\text{extern}}$. Thus, the system of both sublattice Skyrmions (i.e. the AFM Skyrmion) exhibits no net motion resulting from the sublattice Skyrmion motion. However, the two sublattice Skyrmions are displaced, denoted as $\boldsymbol{\delta}$, perpendicular to the total force $\boldsymbol{F}^{+}_{\text{extern}}$. In contrast, as shown in the right sketch of Fig. 3.1, there is no displacement of the sublattice Skyrmions when the sublattice forces acts in opposite directions (meaning $\boldsymbol{F}^{+}_{\text{extern}} = 0$ and $\boldsymbol{F}^{-}_{\text{extern}} \neq 0$). Therefore, the displacement $\boldsymbol{\delta}$ does not depend on $\boldsymbol{F}^{-}_{\text{extern}}$ in the case of vanishing damping $\alpha = 0$. However, it is important to emphasize that the force $\boldsymbol{F}^{-}_{\text{extern}}$ induces a common motion of the two sublattice Skyrmions. Consequently, the entire system, i.e., the AFM Skyrmion, exhibits a net motion that resembles the motion of a ferromagnetic Skyrmion. The fact that in Eq. (3.42) the displacement force $\tilde{\boldsymbol{F}}$ also consists of $\boldsymbol{F}^{-}_{\text{extern}}$ is only due to non-vanishing damping $\alpha > 0$. This shows that the AFM Skyrmion acceleration impacts the sublattice Skyrmion displacement and vice versa.
Returning to the derivation, we use the explicit time resolved equation for the displacement Eq. (3.42) in Eq. (3.39). This yields the AFM Skyrmion velocity

$$\boldsymbol{v}(t) = \frac{1}{2\alpha\mathcal{D}}\left(1 - \exp\left[-\frac{\Lambda\alpha\mathcal{D}}{8\pi^2}t\right]\right)\boldsymbol{F}^{+}_{\text{extern}} - \frac{Q}{8\pi}\exp\left[-\frac{\Lambda\alpha\mathcal{D}}{8\pi^2}t\right]\boldsymbol{F}^{-}_{\text{extern}} \times \boldsymbol{z}. \tag{3.43}$$

This equation describes the resulting velocity of the AFM Skyrmion driven by external forces. Components of the sublattice forces aligned in the same direction,

$\boldsymbol{F}^{+}_{\text{extern}} = \boldsymbol{F}^{A}_{\text{extern}} + \boldsymbol{F}^{B}_{\text{extern}}$, drive the Skyrmion in that direction, while those in opposing directions, $\boldsymbol{F}^{-}_{\text{extern}} = \boldsymbol{F}^{A}_{\text{extern}} - \boldsymbol{F}^{B}_{\text{extern}}$, induce perpendicular motion. Regarding opposing sublattice forces ($\boldsymbol{F}^{+}_{\text{extern}} = 0$) we previously showed that the two sublattice Skyrmions move in the same direction, perpendicular to the force, in the manner of mass-less ferromagnetic Skyrmions. In addition, we showed that the displacement of the two sublattice Skyrmions is only affected by $\boldsymbol{F}^{-}_{\text{extern}}$ in the case of non-vanishing damping. This behavior is visible in Eq. (3.43). The velocity of the AFM Skyrmion is determined by the net motion of its ferromagnetic constituents damped over time. This damping scales with the Gilbert damping α and is connected to the fact that a displacement $\boldsymbol{\delta}$ is induced by $\boldsymbol{F}^{-}_{\text{extern}}$, see Eq. (3.42). Although $\boldsymbol{F}^{-}_{\text{extern}}$ induces a Skyrmion motion and, in the case of finite damping, Skyrmion displacement, it is connected to the typical FM Skyrmion motion and solely its damping is an outcome of the sublattice Skyrmion displacement mechanism[4]. Therefore, when we focus exclusively on the displacement of the sublattice Skyrmions as the sole source of motion, only the force $\boldsymbol{F}^{+}_{\text{extern}}$ acts as driving force for the AFM Skyrmion. While for the FM Skyrmion the gyro-coupling rotates the resulting motion 90 degree w.r.t. the force, this effect is countered by the sublattice displacement creating a motion which is, again, rotated by 90 degrees to the displacement. This has the consequence that the AFM Skyrmion is accelerated into the direction of the force $\boldsymbol{F}^{+}_{\text{extern}}$. Revisiting the classical particle picture, the velocity, Eq. (3.43), fulfills the equation of motion of an externally driven particle, $m\ddot{x} + \Gamma\dot{x} = F$, with a mass $m = 16\pi^2/\Lambda$, $\Gamma = 2\alpha\mathcal{D}$ (as assumed above) and an external driving force $F = F^{+}_{\text{extern}}$.

With a comprehensive understanding of the fundamental mechanisms established, we can now return to the scenario involving current-driven antiferromagnetic Skyrmions. To do so, we substitute the general formulation of the external forces $\boldsymbol{F}^{+}_{\text{extern}}$ and $\boldsymbol{F}^{-}_{\text{extern}}$ with the explicit formulation using the effective electric sublattice currents according to Eq. (3.40). Applying this to the calculation of the Skyrmion velocity in Eq. (3.43) leads to the time dependent velocity of an antiferromagnetic Skyrmion driven by an electric current in the form of

$$\boldsymbol{v}(t) = \left[\frac{4\pi}{\Gamma}\left(\exp\left[-\frac{\Gamma}{m}t\right] - 1\right)\right]\boldsymbol{z}\times\boldsymbol{j}^{-} - \frac{1}{2}\boldsymbol{j}^{+}\left(\frac{\beta}{\alpha} + \frac{(\alpha-\beta)}{\alpha}\exp\left[-\frac{\Gamma}{m}t\right]\right). \tag{3.44}$$

Evidently, the direction of the resulting AFM Skyrmion velocity is perpendicular to $\boldsymbol{j}^{-}$ and parallel to $\boldsymbol{j}^{+}$. In addition to the intriguing fact that the currents $\boldsymbol{j}^{+}$ and $\boldsymbol{j}^{-}$ separate the Skyrmion motion so clearly, Eq. (3.44) yields the possibility of an antiferromagnetic Skyrmion Hall effect. If in each sublattice the currents flow into the same direction, yet with different intensity, the Skyrmion would move along the current direction as well as perpendicular to the current direction and, thus, exhibit a Skyrmion Hall effect. However, we only consider currents of equal intensity with $\boldsymbol{j}^{A} = \pm\boldsymbol{j}^{B}$ in the following analytical investigations as well as in the simulations.

[4] This can be directly seen in Eq. (3.43) when we de-couple the sublattice Skyrmions, i.e. setting $\Lambda = 0$.

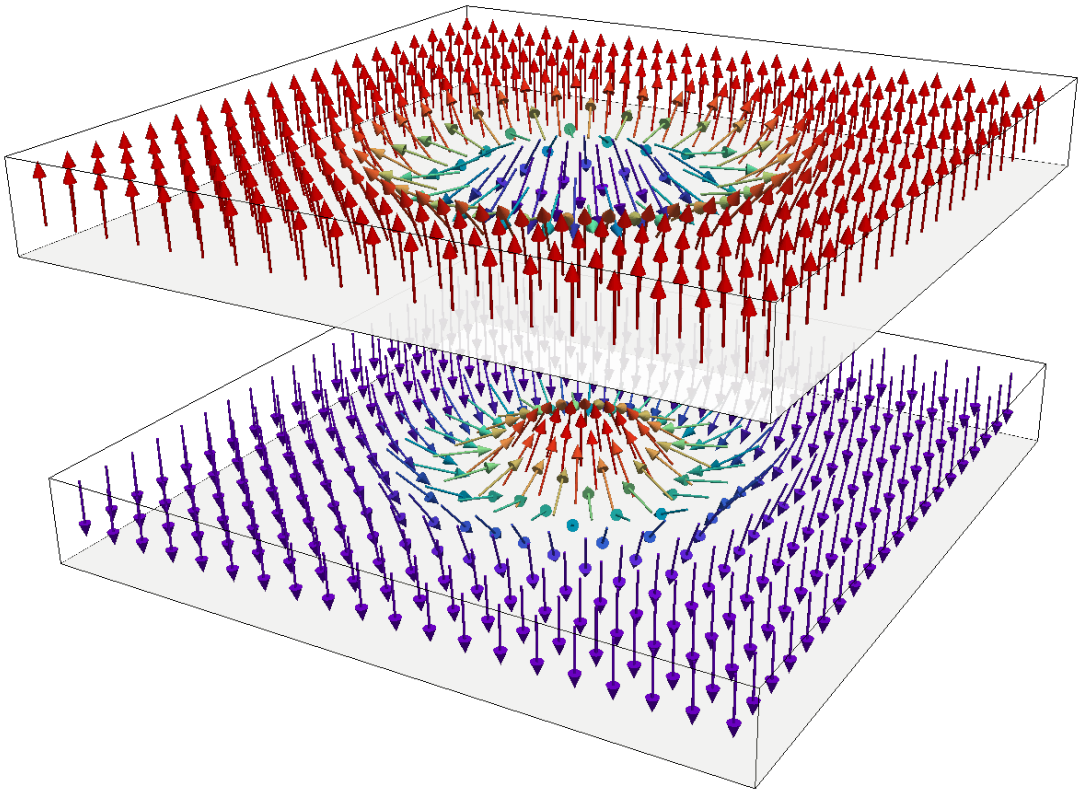

Figure 3.2.: Graphical representation of how the synthetic antiferromagnet is realized in the simulation. The arrows indicate the magnetic moments on each lattice site. Each site is coupled to its nearest neighbor on the same sublattice as well as to the magnetic moment on the same site in the respective other sublattice.

3.4. Numerical simulation

So far, we have used the general bipartite antiferromagnetic energy description of Eq. (3.13) in order to derive the AFM Skyrmion velocity induced by the displacement of the sublattice Skyrmions. As described in Sec. 2.5 this energy encompasses several models, two of which are specifically investigated in our simulations. The first is the single-layer antiferromagnetic square lattice (checkerboard), and the second is the bilayer synthetic antiferromagnet. As predicted by the analytical calculations, the resulting Skyrmion motions in both are equal except the quantitative value of the force constant Λ. For clarity, we focus only on the bilayer synthetic AFM here and provide the simulation results for the bipartite AFM in the Appendix D. In the sense of studying the effect of sublattice Skyrmion displacement the bilayer AFM is the best choice since here we explicitly use two separated sublattices whose coupling strength is immediately shown in the analytical calculations. To describe the synthetic antiferromagnets, we consider the usual model of two ferromagnetic layers which are coupled antiferromagnetically [28, 104]. A graphical representation of how the synthetic AFM is realized in the simulations is shown in Fig. 3.2. The simulations are performed on a discrete lattice. Additionally, the Landau-Lifshitz-

Gilbert (LLG) equation is solved numerically for the magnetic moment at each lattice site, capturing the complete spin dynamics, as opposed to the approximated dynamics provided by the Thiele equation used before. More details regarding the simulation method can be found in Appendix A. In order to simulate the synthetic bilayer AFM lattice, we consider the Hamiltonian

$$H = H_{\mathrm{FM}}^{A} + H_{\mathrm{FM}}^{B} - J_{\mathrm{inter}} \sum_{\boldsymbol{r}} \boldsymbol{a}_{\boldsymbol{r}} \cdot \boldsymbol{b}_{\boldsymbol{r}}. \tag{3.45}$$

It consists of two ferromagnetic Hamiltonians H_{FM} and the on-site coupling of each lattice site from one sublattice to the other. The ferromagnetic Hamiltonians were originally taken from Ref. [45], but have the same form as in Ref. [28]

$$\begin{aligned} H_{\mathrm{FM}} = &- J \sum_{\boldsymbol{r}} \boldsymbol{n}_{\boldsymbol{r}} \cdot (\boldsymbol{n}_{\boldsymbol{r}+\boldsymbol{x}} + \boldsymbol{n}_{\boldsymbol{r}+\boldsymbol{y}}) - K \sum_{\boldsymbol{r}} (n_{\boldsymbol{r}}^{z})^{2} \\ &+ D \sum_{\boldsymbol{r}} \left[(\boldsymbol{n}_{\boldsymbol{r}} \times \boldsymbol{n}_{\boldsymbol{r}+\boldsymbol{x}}) \cdot \boldsymbol{x} + (\boldsymbol{n}_{\boldsymbol{r}} \times \boldsymbol{n}_{\boldsymbol{r}+\boldsymbol{y}}) \cdot \boldsymbol{y} \right], \end{aligned} \tag{3.46}$$

where we choose for the simulations $D/J = 0.09$, $K/J = 0.013$ and $J_{\mathrm{inter}}/J = 1$. By setting the lattice constant $d = 1$ (i.e. only consider it as a unit) the Hamiltonian can be immediately compared with the continuum approach of the antiferromagnet, $H = H_{\mathrm{FM}}^{A} + H_{\mathrm{FM}}^{B} - J_{\mathrm{inter}} \boldsymbol{a} \cdot \boldsymbol{b}$. That means it coincides with the general antiferromagnetic energy from Eq. (3.13), when neglecting all inter-sublattice coupling constant except λ. In the following we will identify $\lambda/2 = J_{\mathrm{inter}}$, leading to an explicit expression of the force constant $\Lambda = J_{\mathrm{inter}} \mathcal{D}$ (for the calculation see Appendix B). Consequently, the AFM Skyrmion mass $m = 16\pi^2/\Lambda$, see Eq. (3.32), is inversely proportional to the interlayer coupling in such a case that

$$m = \frac{16\pi^2}{J_{\mathrm{inter}} \mathcal{D}}. \tag{3.47}$$

Regarding current-driven Skyrmions we consider two particular cases. The first is that both sublattice currents are of equal intensity and flow in the same direction $\boldsymbol{j}^{A} = \boldsymbol{j}^{B} = \boldsymbol{j}$, concretely $j = 0.05 \frac{d}{t_0}$. This scenario resembles the usual assumption for current driven Skyrmions in antiferromagnets [32, 103]. This means for the effective current $|\boldsymbol{j}^{+}| = 2j$. The resulting time dependent Skyrmion velocity is [see Eq. (3.44)]

$$v(t) = j \left(\frac{\beta}{\alpha} + \frac{\alpha - \beta}{\alpha} \exp\left[-\frac{\Gamma}{m} t \right] \right). \tag{3.48}$$

It appears that the Skyrmion moves parallel to the electric current. The resulting velocity is the same as a ferromagnetic Skyrmion would have, combined with the velocity induced by the displacement due to the Skyrmion Hall effect in each sublattice. This becomes clear if one considers the special case $\alpha = \beta$. For this parameter configuration, there exists no SHE for the FM sublattice Skyrmions and the resulting AFM Skyrmion velocity is the same as for FM Skyrmions. The final velocity in Eq. (3.48) is $j\beta/\alpha$ which coincides with the predicted velocity of Ref. [32]. This final velocity does not depend on the Skyrmion

parameters, however, its time constant Γ/m does. In Fig. 3.3 the Skyrmion velocity over time is plotted for different values of β using a damping parameter $\alpha = 0.01$. The colored dots mark the Skyrmion velocity from the simulation while the solid black lines are fitted to Eq. (3.48). The only fitting parameter which can be read from these fits is the time

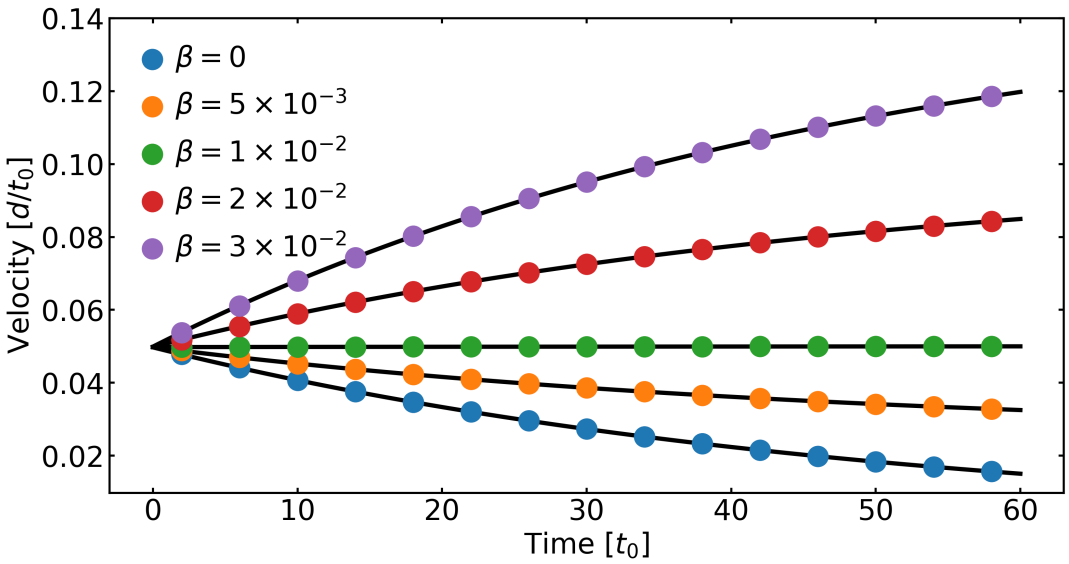

Figure 3.3.: Velocity of an antiferromagnetic Skyrmion driven by two uni-directional flowing electric currents over time for different values of the parameter β at $\alpha = 0.01$. While the dots represent the Skyrmion velocity obtained from the simulation, the solid lines are fits to Eq. (3.48).

constant $\Gamma/m = \alpha\mathcal{D}\Lambda/(8\pi^2)$. All fits shown in Fig. 3.3 yield $\mathcal{D}\Lambda \approx 158.5$, where we set $J = 1$ in all simulations. The magnitude of the dissipation parameter $\mathcal{D} = \int(\partial_x \boldsymbol{a})^2 \mathrm{d}^2\boldsymbol{r}$ can be approximated numerically and is for both sublattices $\mathcal{D} \approx 18.4$. Thus, the force constant $\Lambda \approx 8.6$ differs significantly from the previously assumed quantity $\Lambda = J_{\mathrm{inter}}\mathcal{D}$. However, before we further investigate this discrepancy, we examine the second scenario. For this, we assume anti-parallel currents with the same intensity $\boldsymbol{j} = \boldsymbol{j}^A = -\boldsymbol{j}^B$, concretely $j = 0.001$. Although this would be unrealistic for mono-layer systems, it is possible to be realized in synthetic AFM as proposed by Koshibae and Nagaosa in Ref. [28]. The opposing currents move the sublattice Skyrmions apart and, thus, induce a motion perpendicular to the current direction. The Skyrmion motion is so sensitive to a sublattice Skyrmion displacement, that the SHE in the sublattices plays a negligibly small role in this scenario. The resulting time dependent Skyrmion velocity [see Eq. (3.44)],

$$v(t) = \frac{8\pi j}{\Gamma}\left(1 - \exp\left[-\frac{\Gamma}{m}t\right]\right) \tag{3.49}$$

mainly depends on the damping $\Gamma = 2\alpha\mathcal{D}$ and evolves with the same time constant Γ/m as the first scenario. Since the impact of the parameter β is negligible, we simulated the Skyrmion motion for different magnitudes of the damping parameter α and fitted them to Eq. (3.49). This is shown in Fig. 3.4. In comparison with the scenario of parallel flowing

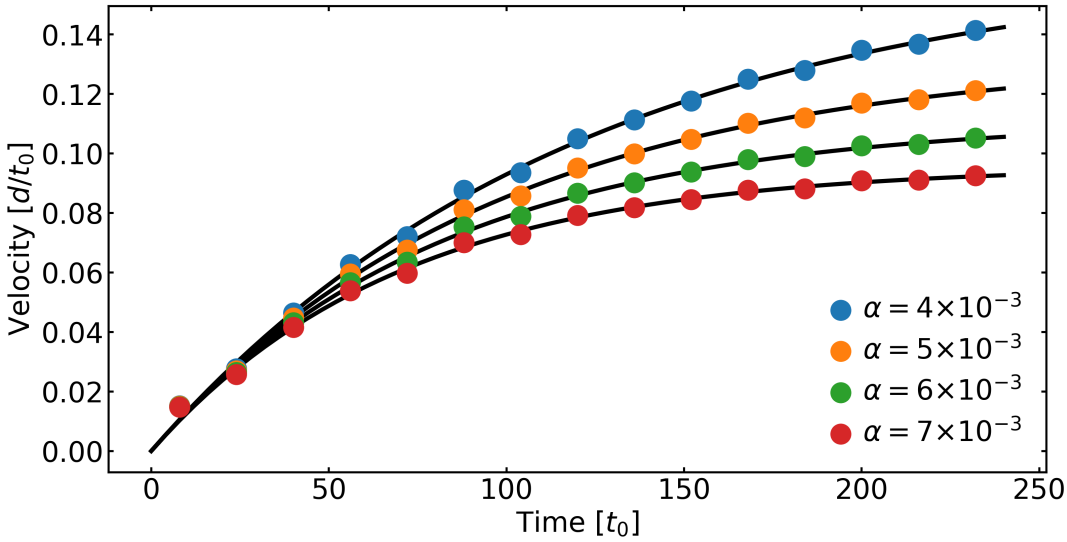

Figure 3.4.: Velocity of an antiferromagnetic Skyrmion driven by two anti-parallel flowing electric currents over time for different values of the Gilbert damping parameter α. While the dots represent the Skyrmion velocity obtained from the simulation, the solid lines are fits to Eq. (3.49).

electric currents, the Skyrmion velocity induced by anti-parallel flowing currents is in the same order of magnitude although the current densities are much lower (factor 50). This might be of particular interest for technical application where low current densities are preferable [105]. The fitted values of the dissipation constant $\mathcal{D} \approx 19$ and the force constant $\Lambda \approx 8.6$ are roughly the same as in the first scenario. To investigate the discrepancy of the parameter Λ between the simulations and the analytical derivation, we plotted the explicitly displacement-dependent equations $\int (\partial_y \boldsymbol{a}) \cdot \boldsymbol{b}\ \mathrm{d}^2\boldsymbol{r} = \Lambda\delta$ and $4\pi v = \Lambda\delta$ (or $4\pi(v+j) = \Lambda\delta$, respectively) for both scenarios, using a force constant of $\Lambda = 8.6$ for one example each. This is shown in Fig. 3.5. It confirms the validity of the previously derived

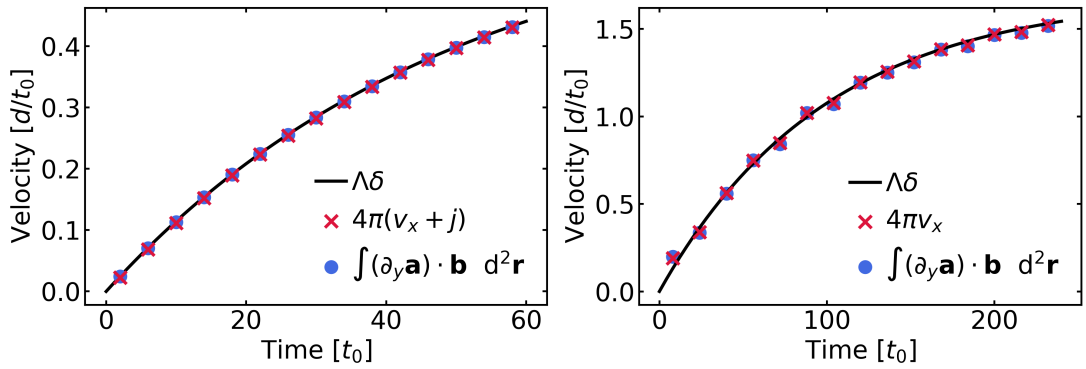

Figure 3.5.: Comparison of the internal force, velocity, and the value $\int (\partial_y \boldsymbol{a}) \cdot \boldsymbol{b}\ \mathrm{d}^2\boldsymbol{r} = \Lambda\delta$ of the current-driven antiferromagnetic Skyrmion, according to the Eqs. (3.27) and (3.22), for two different scenarios. In one scenario both sublattice currents flow in the same direction (left) while int the other scenario the two sublattice currents are anti-parallel to each other (right).

formalism of AFM Skyrmion motion even regarding the full dynamics in the simulations, provided that the parameter Λ is appropriately adjusted. Furthermore it indicates that both scenarios require the same adjustment of the parameter Λ.

Inconsistencies of the value of Λ

For the derivation of the formalism above in Sec. 3.1 we have considered the two sublattice Skyrmions to be rigid. This is a strong simplification of the complex behavior of magnetic structures. Typically, moving ferromagnetic and anti-ferromagnetic Skyrmions exhibit dynamical modes [102] and deformation [107], which will be covered by the numerical simulations solving the LLG for each lattice site. Since these excitations are not covered by the Thiele approximation used in the derivation of the sublattice Skyrmion displacement formalism, it is not surprising that the simulations differ from the analytical calculations [51]. However, the fact that only a single parameter, Λ, needs to be adjusted for the formalism to match the simulations warrants closer examination. To this end we plot the numerically calculated entries of the dissipation tensor $\mathcal{D}_{ij}^{A/B}$ (see [71] or Appendix B) for both scenarios of current-driven Skyrmions in Fig. 3.6. A non-disturbed, resting

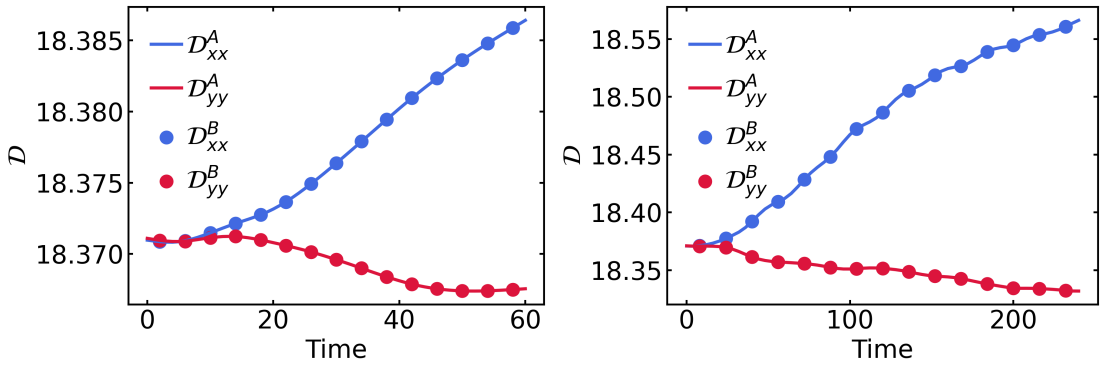

Figure 3.6.: Quantity of the diagonal entries of the dissipation tensor $\mathcal{D}_{ij}$ over time. The tensor entries are calculated for both sublattices, A (dots) and B (solid lines). Both show the motion of an initially resting AFM Skyrmion due to the application of electric current. While the left plot shows the results of the case of uni-directional electric current, the right plot shows the result for applying anti-parallel flowing current.

Skyrmion is radial symmetric and, thus, the entries of the tensor are the same for each direction, i.e. $\mathcal{D}_{ij} = \delta_{ij}\mathcal{D}$ and the same for each sublattice. As one can see in Fig. 3.6 this is indeed the case for the initially resting Skyrmion at $t = 0$. However, when the Skyrmion is accelerated ($t > 0$ in the plots) the entries in x direction increase while the entries in y direction decrease for both scenarios while the sublattice symmetry still holds. In addition, the mixing entries $\mathcal{D}_{xy} = 0$ still vanish (not shown here) over the whole time. This shows that there is, indeed, a non-isotropic deformation of both sublattice Skyrmions building up depending on the displacement direction (in this case y direction). Those deformations become even more relevant in the Skyrmion motion due to an artificial initial displacement.

3.5. Motion due to artificial displacement

In the beginning of the derivation in Sec. 3.2, we introduced a displacement between the sublattice Skyrmions. This displacement was intentionally not tied to a specific source, as it serves as a general formalism for describing displacement. Likewise to the current-induced motion, in the previous section 3.4, the analytically derived Skyrmion dynamics due to an artificial displacement will be compared to simulations. To do so we simulated the resulting motion of an antiferromagnetic Skyrmion after its sublattice constituents were displaced initially. The system was considered damping-less $\alpha = 0$ and without any external forces. To realize such a displacement in the simulation is not a trivial task since one sublattice Skyrmion must be shifted by less than one lattice site. This can only be done approximately by assuming an explicit Skyrmion profile. For this we followed Ref. [108] where the suggested Skyrmion profile is modeled by a 360° domain wall (originally proposed by Ref. [109]). The Skyrmion profile is, therefore, assumed to be

$$\Theta(\rho) = 2 \arctan\left(\frac{\sinh[R/w]}{\sinh[\rho/w]}\right) \tag{3.50}$$

with the Skyrmion radius R and the Skyrmion width w. We simulated a stationary antiferromagnetic Skyrmion and fitted the sublattice Skyrmions to the profile in Eq. (3.50) in order to get the parameter R and w. Indeed, each parameter is the same for sublattice A and B and the fitted Skyrmion profile matches the simulated Skyrmion profile (not shown here). Subsequently, we shifted the origin of one of both sublattice Skyrmions by a small distance $\boldsymbol{\delta}$ and reconstruct the Skyrmion by using Eq. (3.50) with the parameters obtained from the fits. By this, we are able to artificially displace the sublattice Skyrmions by an arbitrary displacement $\boldsymbol{\delta}$. In accordance with the analytical results from Sec. 3.2 the initial displacement induces a perpendicular Skyrmion motion. The distance the AFM Skyrmion traveled over time is shown in the left plot of Fig. 3.7. The dots mark the actual Skyrmion position while the solid line shows a linear function fitted to the Skyrmion position over time. It appears that in leading order the AFM Skyrmion travels with a constant velocity, as we derived earlier by using the Thiele approximation. However, the Skyrmion motion shows an additional oscillation around the linear motion over time. The right plot of Fig. 3.7 shows the resulting Skyrmion velocity induced by different displacements δ. To get the data we prepared the lattice with an AFM Skyrmion consisting of displaced sublattice Skyrmions and fitted the resulting motion over time to a linear function as shown in the left plot of Fig. 3.7. This was done for different values of δ to get the right plot of Fig. 3.7. The resulting Skyrmion velocity shows, indeed, a linear dependency of the displacement and, thus, qualitatively confirms Eq. (3.27). Fitting the Skymrion velocity in dependence on the initial displacement yields a force constant $\Lambda \approx 8.2$.

Regarding the oscillations visible in the left plot of Fig. 3.7, we assume that they are due to the way we have created the initial displacement. By applying Thiele's approximation we consider the sublattice Skyrmions as rigid and of the same form as in the stationary state

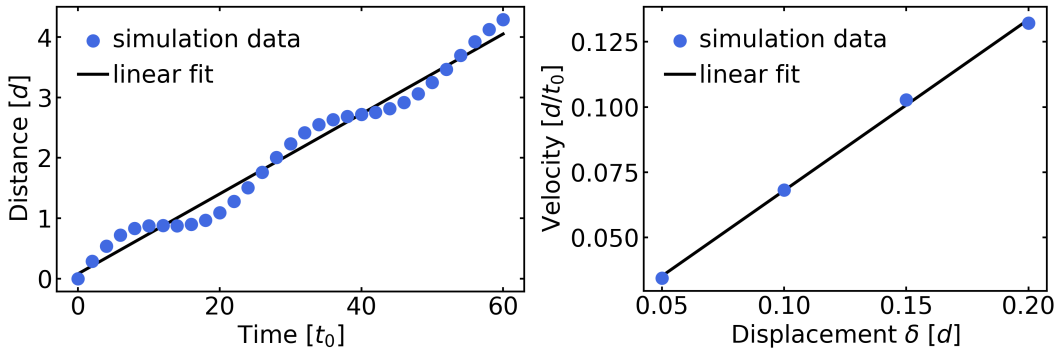

Figure 3.7.: Left: Distance traveled by a freely moving antiferromagnetic Skyrmion due to an initial sublattice Skyrmion displacement. The dots mark the distance the Skyrmion traveled in the simulation while the solid line is a linear fit to these distances. Right: Fitted Skyrmion velocity in dependence on the initial displacement. The dots mark the fitted velocities while the solid line is a linear fit according to Eq. (3.27).

while the excitation is solely due to the displacement. It turned out to be a (qualitatively) good approximation for understanding the ground laying mechanics, however it does not fully capture the realistic dynamical behavior of the two sublattice Skyrmions. To investigate this further, we compare two scenarios. In the first scenario we artificially displace the sublattices of a resting AFM Skyrmion (as explained previously) by $\delta/d = 0.04$ and in the second we accelerate the Skyrmion using parallel flowing electric currents (see the previous section 3.4) and instantly switching off the current when the Skyrmion reaches a particular velocity. The simulation results of both scenarios are shown in Fig. 3.8. The resulting Skyrmion velocities are depicted by the solid lines, illustrating the effects of an artificially created displacement (in blue) and a displacement induced by prior current-induced acceleration (in red). Additionally, the quantity $\int(\partial_y \boldsymbol{a}) \cdot \boldsymbol{b}\, \mathrm{d}^2\boldsymbol{r}$ is plotted as dots for both scenarios. While the previously (current-induced) accelerated Skyrmion moves with a constant velocity, the velocity of the artificially displaced Skyrmion oscillates. The agreement of the dots with the solid lines in Fig. 3.8 indicates that the simulations validate the equation $4\pi v = \int(\partial_y \boldsymbol{a}) \cdot \boldsymbol{b}\, \mathrm{d}^2\boldsymbol{r}$, as predicted by the formalism, for both cases. Furthermore, in both cases the sublattice Skyrmion displacement over time stays constant except some minor deviations (not shown here). Consequently, the oscillations exhibited in the first scenario are not due to an altering displacement. That means, on the other hand, the oscillation must be induced by an altering Λ. The starting velocity of the artificially displaced Skyrmion is $v_0 = 0.73\frac{d}{t_0}$ which leads, with the initial displacement $\delta/d = 0.04$, to a force constant of $\Lambda \approx 18.3$ and consequently to a dissipation parameter quantity of $\mathcal{D} \approx 18.3$ (since $\Lambda = J_{\mathrm{inter}}\mathcal{D}$ and we set $J_{\mathrm{inter}}/J = 1$). This resembles exactly the velocity according to the rigid sublattice Skyrmion approximation indicating that Eq. (3.27) is, indeed, correct for rigid sublattice Skyrmions. Since the Skyrmions exhibit oscillating velocities following an initial displacement but attain a constant velocity after undergoing prior acceleration, we conclude that the configuration of the sublattice Skyrmions must

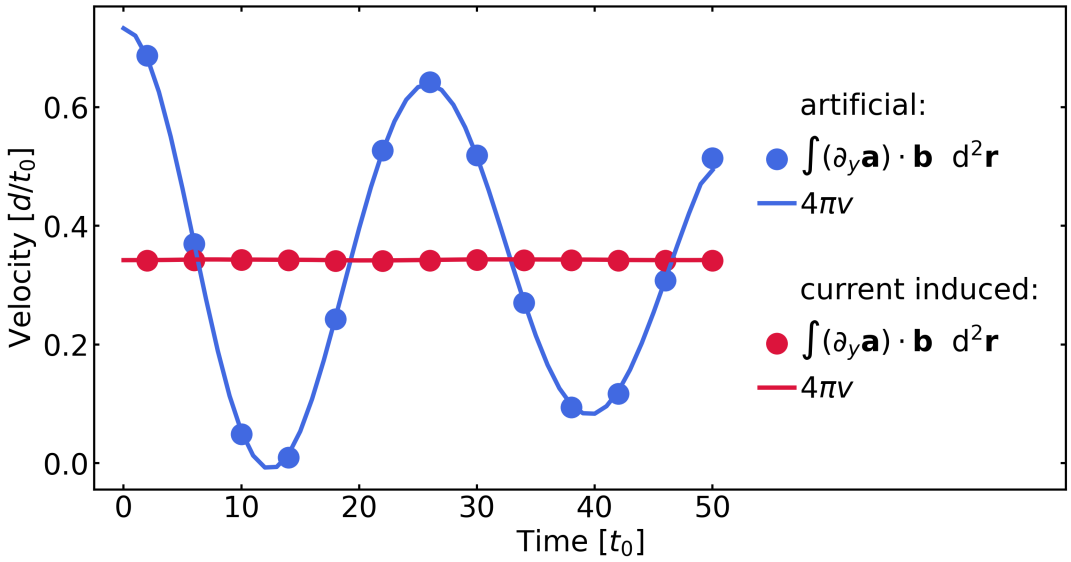

Figure 3.8.: Velocity (solid lines) and the quantity of $\int(\partial_y \boldsymbol{a})\cdot\boldsymbol{b}\,\mathrm{d}^2\boldsymbol{r}$ (dots) of a freely moving antiferromagnetic Skyrmion with two different causes of motion. One is an artificial initial sublattice Skyrmion displacement (depicted in blue), while the other is a previous acceleration induced by an electric current (depicted in red).

adapt (deform) during the acceleration process. To investigate this we compare in Fig. 3.9 the diagonal entries of the dissipation tensor $\mathcal{D}_{ij}$ for both sublattices. Conserving the sublattice symmetry, the quantity of each entry coincides for both sublattices A and B in any case. Apart from this, the time dependent quantities of the dissipation tensor from the artificially displaced Skyrmion (left plot) differ significantly from those of the accelerated Skyrmion (right plot). While the value of both $\mathcal{D}_{xx}$ and $\mathcal{D}_{yy}$ stays roughly constant for the latter, they oscillate for the former (note the scale of $\mathcal{D}$). Furthermore, the prior-accelerated Skyrmion exhibits a clear difference between the x and y direction at the start of the simulation ($t = 0$), stemming from the current-induced acceleration applied before, and keeps this difference over time. In contrast, the artificially displaced sublattice Skyrmions are, per construction, at $t = 0$ radially symmetric while the difference between the tensor entries in x and y direction alters over time. Comparing these two scenarios leads to the conclusion that the Skyrmion has to slowly build up the anisotropic deformation along the displacement axis during acceleration and stays anisotropic as long as it has a finite velocity. Instantaneously forcing the displacement to isotropic Skyrmions, however, results in oscillating motion as seen in Fig. 3.7.

3.6. Conclusions

In this chapter, we treated the antiferromagnetic Skyrmion as a composite of two effectively coupled ferromagnetic sublattice Skyrmions. By employing the rigid Skyrmion approximation, inspired by Thiele's approximation, we treated each sublattice Skyrmion

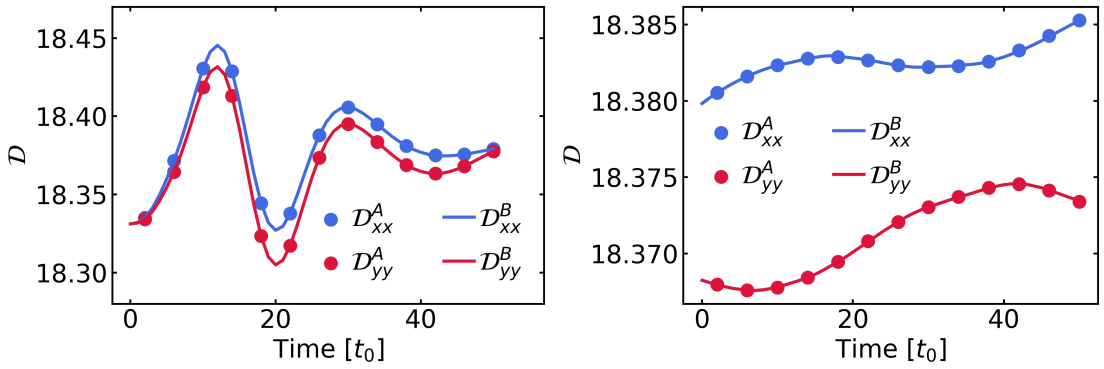

Figure 3.9.: Quantity of the diagonal entries of the dissipation tensor $\mathcal{D}_{ij}$ over time. The tensor entries are calculated for both sublattices, A (dots) and B (solid lines). Shown are two scenarios. Left: An antiferromagnetic Skyrmion moving due to an artificial sublattice Skyrmion displacement as starting state. Right: An antiferromagnetic Skyrmion moving due to a previous acceleration induced by an electric current.

as an individual ferromagnetic Skyrmion that interacts with its counterpart. We derived that a small displacement $\boldsymbol{\delta}$ between these two sublattice Skyrmions results in an overall motion of the antiferromagnetic Skyrmion, oriented perpendicularly to the displacement. Furthermore, we found that the resulting velocity is directly proportional to the displacement itself.

The underlying mechanism for this behavior is that each sublattice Skyrmion creates a harmonic potential for the other, inducing an attractive force between them. Due to the gyro-coupling $\boldsymbol{G} \times \boldsymbol{v}$ a force acting on a ferromagnetic Skyrmion leads to a motion perpendicular to this force. Thus, the attractive forces move the Skyrmion perpendicular to the force direction instead of pulling the sublattice Skyrmions together. Consequently, the two sublattice Skyrmions remain displaced while moving perpendicularly to their displacement $\boldsymbol{\delta}$. This finding illustrates that any displacement of a sublattice Skyrmion leads to a motion of the antiferromagnetic Skyrmion.

Building on this understanding, we are able to explain the inertia of an antiferromagnetic Skyrmion. By treating the compound of the sublattice Skyrmions as a single antiferromagnetic Skyrmion and considering the displacement as an internal degree of freedom, we can formulate a comprehensive equation of motion for the antiferromagnetic Skyrmion. We connected this equation of motion to classical Newtonian mechanics and found that the AFM Skyrmion can be interpreted as a classical quasi-particle exhibiting an effective mass. Additionally, we related the velocity of the AFM Skyrmion to the harmonic potential created by the sublattice Skyrmion displacement. We found that it resembles the kinetic energy of a classical particle with the same mass, completing the picture of the AFM Skyrmion as a classical particle.

We subsequently investigated the effects of external forces on the antiferromagnetic Skyrmion and have determined that its motion arises from two distinct contributions. One of these is the component of motion that both sublattice Skyrmions exhibit in unison. Since these

Skyrmions are governed by ferromagnetic sublattice dynamics, they will maintain this behavior while they contribute to the overall motion. The second contribution arises from the relative motion between the sublattice Skyrmions. This relative displacement of the sublattice Skyrmions leads to a displacement-induced motion, as described by our theoretical framework. Additionally, we examined current-driven Skyrmions as a significant example of external driving forces due to their technological relevance. To this end, we incorporated the spin transfer torques (see Ch. 2) into the equation of motion of each sublattice Skyrmion. Combining this with the effective sublattice coupling and the rigid Skyrmion approximation, we derived an analytical expression for the resulting velocity of a current-driven antiferromagnetic Skyrmion. To validate our findings, we simulated two scenarios: unidirectional and anti-parallel currents of equal magnitude. Our simulations align well with our analytical predictions, except for a particular parameter, Λ, related to the Skyrmion form, which requires adjustment.

To elucidate the discrepancy in Λ between our analytical calculations and the simulation results, we compared the Skyrmion configurations of a stationary Skyrmion versus one in motion, noting that the latter loses its radial symmetry. Additionally, we artificially induced an initial displacement to compare its resulting dynamics with that of a naturally occurring displacement from prior acceleration. The artificial displacement, which can be interpreted as an instantaneous excitation, led to oscillatory behavior in both the Skyrmion configuration and its velocity, whereas the naturally occurring displacement resulted in a constant velocity as predicted by our theory. We concluded that a slow acceleration of the resting Skyrmion allows each sublattice Skyrmion to continuously deform without exciting internal modes while the sublattice Skyrmions displace, likewise an adiabatic process. Thus, the observed difference in Λ (compared to the analytical derivation) stems from the deformation of the sublattice Skyrmions during the acceleration process, a dynamics not captured by Thiele's approximation. This insight paves the way for future research investigating the dynamics induced by sublattice Skyrmion displacement beyond Thiele.

Besides using electric currents as the driving force for the antiferromagnetic Skyrmion dynamics, there are other ways to drive them. One is the Skyrmion motion due to its interaction with spin waves. This will be investigated further in the next chapter.

4. Spin wave - skyrmion interaction

Ferromagnetic Skyrmions are known to be affected by various external influences, including electric currents [17], heat gradients [110], impurity clusters [111], and spin waves [112], with the latter being the focus of this chapter. Given that ferromagnetic Skyrmions interact with spin waves, it is reasonable to assume that antiferromagnetic Skyrmions do so as well. Moreover, due to their increased sensitivity to external driving sources, such as electric currents, compared to their ferromagnetic counterparts [see 26], antiferromagnetic Skyrmions are likely to exhibit a more intense reaction to spin waves. Investigating the behavior of antiferromagnetic Skyrmions in the presence of spin waves leads to several benefits. First, by understanding how Skyrmions respond to spin waves, one can predict their motion under the influence of these waves, which are inherently present at non-zero temperatures [113, 114]. This knowledge enhances the understanding of antiferromagnetic Skyrmion behavior in potential future experimental settings. Another benefit is the potential to exploit spin waves to drive antiferromagnetic Skyrmions. This is particularly intriguing in the context of Skyrmion racetrack technology [105], where effectively controlling the motion of Skyrmions can lead to advancements in data storage technologies.

4.1. Model

In this chapter we show how spin waves affect Skyrmions on an antiferromagnetic lattice. To this end, we focus on a particular system, namely, the two-dimensional square lattice. It does not perfectly resemble the crystal lattice of helimagnetical materials. However, it is a well established (e.g., Ref. [45]) model in which it is possible to explain and predict realistic Skyrmion behavior as, for instance, current-induced Skyrmion motion [45, 111], Skyrmion creation [115, 116], and Skyrmion decay [87]. Furthermore, it provides a simple, yet sufficiently complex basis to study the impact traveling spin waves have on Skyrmions. Because we deliberately aim to include the lattice effects[1], the model of choice is a discrete lattice Hamiltonian. It is the same Hamiltonian as used in the numerical simulations (see Appendix A) which makes the comparison to simulations more reliable. It is based on Ref. [45] and reads

$$H = -\frac{J}{2}\sum_{\langle i,j\rangle} \boldsymbol{n}_i \cdot \boldsymbol{n}_j - D\sum_{\langle i,j\rangle} \mathbf{d}_{ij} \cdot (\boldsymbol{n}_i \times \boldsymbol{n}_j) - K\sum_i \left(n_i^z\right)^2, \tag{4.1}$$

[1] This is rather rare in the Skyrmionics community. Indeed, Ref. [91] was the first considering lattice effects for spin wave driven antiferromagnetic Skyrmions.

where $\langle i,j\rangle$ means the sum over nearest neighbors and the exchange interaction J determines whether we consider a ferromagnet ($J>0$) or an antiferromagnet ($J<0$). The Dzyaloshinskii-Moriya interaction (DMI) is included here as a phenomenological term with the DMI parameter D in a rather general form. The vector $\boldsymbol{d}_{ij}$ defines whether we consider bulk DMI $\boldsymbol{d}_{ij}=\boldsymbol{r}_{ij}$ or interfacial DMI $\boldsymbol{d}_{ij}=\boldsymbol{r}_{ij}\times\boldsymbol{z}$, where $\boldsymbol{r}_{ij}$ is the distance vector between sites i and j. By that both Skyrmion types Bloch- and Néel are covered (see Sec. 2.4). As a representation of the magnetic moments we used vectors of unit length $|\boldsymbol{n}|=1$. Following Ref. [91] the unit of the actual magnetization, the magnetic saturation M_S, is absorbed into the system parameters, see Ch. 2 for more details. The corresponding effective field $\boldsymbol{H}_i^{\text{eff}}=-\partial H/\partial\boldsymbol{n}_i$ is, thus,

$$\boldsymbol{H}_i^{\text{eff}}=J\sum_{\boldsymbol{r}}\boldsymbol{n}_{i+\boldsymbol{r}}+2D\sum_{\boldsymbol{r}}(\boldsymbol{n}_{i+\boldsymbol{r}}\times\boldsymbol{d}_{i,i+\boldsymbol{r}})+2Kn_i^z\boldsymbol{z}. \tag{4.2}$$

The sum $\sum_{\boldsymbol{r}}$ denotes the sum over the four nearest neighbors $\boldsymbol{r}\in\{\pm\boldsymbol{x},\pm\boldsymbol{y}\}$ of the lattice site i. For all dynamical considerations we use the Landau Lifshitz Gilbert (LLG) equation

$$\partial_t\boldsymbol{n}_i=-\gamma\boldsymbol{n}_i\times\boldsymbol{H}_i^{\text{eff}}+\alpha\boldsymbol{n}_i\times\partial_t\boldsymbol{n}_i, \tag{4.3}$$

where α is the damping parameter and we set the gyromagnetic ratio γ in such a way that the unit of time is $t_0=1/J$ [91].
When we study an antiferromagnetic (AFM) lattice, we assume two effectively coupled ferromagnetic sublattices. Again, we will use the convention to name them $\boldsymbol{a}_i$ and $\boldsymbol{b}_i$ corresponding to whether the lattice site i is in the sublattice A or B. Therefore, we have to consider two equations of motion (EOM) of the same form as Eq. (4.3) where each sublattice is affected by its own effective field. Since each lattice site has only nearest neighbors of the respective other sublattice, the effective field for the sublattice A is

$$\boldsymbol{H}_{i,A}^{\text{eff}}=J\sum_{\boldsymbol{r}}\boldsymbol{b}_{i+\boldsymbol{r}}+2D\sum_{\boldsymbol{r}}(\boldsymbol{b}_{i+\boldsymbol{r}}\times\boldsymbol{d}_{i,i+\boldsymbol{r}})+2Ka_i^z\boldsymbol{z}, \tag{4.4}$$

and similar for $\boldsymbol{H}_{i,B}^{\text{eff}}$ [91]. We assume the same gyromagnetic ratio and damping for each sublattice.

4.2. Spin waves

Spin waves without damping

In order to understand how spin waves affect Skyrmions, we have to study classical magnetic spin waves in more detail. To this end we derive the spin wave behavior in this section. The underlying idea is that we assume the lattice to be in a classical (anti-) ferromagnetic ground state, $\boldsymbol{n}_0$, and the spin waves are only small perturbations $\delta\boldsymbol{n}$ of this state. Concretely, that means we assume that the whole time-dependent behavior can be

described by small perturbation of the time independent ground state, i.e.,

$$\boldsymbol{n}(t) \approx \boldsymbol{n}_0 + \delta\boldsymbol{n}(t). \tag{4.5}$$

Since the perturbations are assumed to be small, we neglect in the following quantities which are of order $\mathcal{O}(\delta\boldsymbol{n}^2)$ (linearization of the dynamics). Under this assumption the perturbation has to be perpendicular to the ground state because the length of the magnetic moment $|\boldsymbol{n}|^2 = 1$ should be conserved. That means $|\boldsymbol{n}_0|^2 + |\delta\boldsymbol{n}|^2 + 2\boldsymbol{n}_0 \cdot \delta\boldsymbol{n} = 1$ holds for all time t. Since the ground state fulfills the same properties, the scalar product vanishes $\boldsymbol{n}_0 \cdot \delta\boldsymbol{n} = 0$. We consider a model which has an easy-axis anisotropy along the z direction, $K(n_z)^2$, so that the ground state must align with this axis $\boldsymbol{n}_0 = \pm\boldsymbol{z}$. Therefore, it is only possible for the perturbations $\delta\boldsymbol{n}(t)$ to take place in the xy plane. Using the linearization, Eq. (4.5), for the equations of motion Eq. (4.3) yields

$$\partial_t \delta\boldsymbol{n}_i(t) = -\delta\boldsymbol{n}_i(t) \times \boldsymbol{H}_i^{\mathrm{eff},0} - \boldsymbol{n}_0 \times \delta\boldsymbol{H}_i^{\mathrm{eff}}(t), \tag{4.6}$$

where $\boldsymbol{H}_i^{\mathrm{eff},0}$ and $\delta\boldsymbol{H}_i^{\mathrm{eff}}(t)$ are the adapted versions of Eq. (4.4). Although this work is about antiferromagnetic lattices, we start with deriving ferromagnetic spin waves and expand that formalism to antiferromagnetic spin waves later. For the ferromagnetic case we consider the ground state to be in positive z direction, $\boldsymbol{n}_0 = \boldsymbol{z}$. This leads to a ground state effective field of $\boldsymbol{H}_i^{\mathrm{eff},0} = (4J + 2K)\boldsymbol{z}$. This is because each lattice site has four nearest neighbors and since all spins have the same direction the DMI part becomes zero. The value $4J + 2K$ is the homogeneous energy density of the ground state, which we will denote as $\rho := 4J + 2K$, following Ref. [91].
The DMI part of $\boldsymbol{H}_i^{\mathrm{eff},0}$, which is $2D\sum_{\boldsymbol{r}} \left(\boldsymbol{n}_{i+\boldsymbol{r}}^0 \times \boldsymbol{d}_{i,i+\boldsymbol{r}}\right)$, includes the ground state spins $\boldsymbol{n}_i^0$ which each align in z direction. Since they are independent of their lattice site (i.e., homogeneous ground state), the term can be rewritten as $2D\sum_{\boldsymbol{r}} (\boldsymbol{z} \times \boldsymbol{d}_{i,i+\boldsymbol{r}})$. Due to the anti-symmetry of the vector $\boldsymbol{d}_{ij} = -\boldsymbol{d}_{ji}$ the sum vanishes. In general, the sum would vanish for every homogeneous state, independent whether it is $\boldsymbol{n}_0$, $\boldsymbol{a}_0$ or $\boldsymbol{b}_0$. Regarding $\delta\boldsymbol{H}_i^{\mathrm{eff}}(t)$ it is important to consider that $\boldsymbol{n}_0$ (or $\boldsymbol{a}_0$ and $\boldsymbol{b}_0$ for the AFM) are parallel to the z axis. The reason is that $\delta\boldsymbol{H}_i^{\mathrm{eff}}(t)$ appears in a cross product together with $\boldsymbol{n}_0$ (see Eq. (4.5)), so that the crucial term here is $\boldsymbol{z} \times \sum_{\boldsymbol{r}} (\delta\boldsymbol{n}_{i+\boldsymbol{r}} \times \boldsymbol{d}_{i,i+\boldsymbol{r}})$. As explained above, the small perturbation of the ground state is perpendicular to it, i.e., $\delta\boldsymbol{n} \perp \boldsymbol{n}_0$, and, thus, perpendicular to the z axis. Since the vector $\boldsymbol{d}_{ij}$ also lies in the xy plane, the cross product $\delta\boldsymbol{n}_{i+\boldsymbol{r}} \times \boldsymbol{d}_{i,i+\boldsymbol{r}}$ is parallel to the z axis; independent of the lattice site i. This has the consequence that the term $\boldsymbol{z} \times \sum_{\boldsymbol{r}} (\delta\boldsymbol{n}_{i+\boldsymbol{r}} \times \boldsymbol{d}_{i,i+\boldsymbol{r}})$ vanishes, so that the term $\boldsymbol{n}_0 \times \delta\boldsymbol{H}_i^{\mathrm{eff}}(t)$ is independent of the DMI. In conclusion, both $\boldsymbol{H}_i^{\mathrm{eff},0}$ and $\delta\boldsymbol{H}_i^{\mathrm{eff}}(t)$ are independent of the DMI, indicating that the spin waves around the (anti-)ferromagnetic ground state are independent of the DMI as well [91]. However, one should keep in mind that the independence of the DMI is only due to the linearization of the equation of motion and the consideration of an out-of-plane ground state [91].

In conclusion, the linearized equation of motion becomes

$$\partial_t \delta \boldsymbol{n}_i = \rho \boldsymbol{z} \times \delta \boldsymbol{n}_i - \boldsymbol{z} \times \left[J \sum_{\boldsymbol{r}} \delta \boldsymbol{n}_{i+\boldsymbol{r}} \right]. \tag{4.7}$$

Recapping that the small deviations $\delta \boldsymbol{n}$ were introduced to describe spin waves, we consequently assume them to exhibit the wave form

$$\delta \boldsymbol{n}_i = A \begin{pmatrix} \cos\left(\boldsymbol{r}_i \cdot \boldsymbol{k} - \omega t\right) \\ \sin\left(\boldsymbol{r}_i \cdot \boldsymbol{k} - \omega t\right) \\ 0 \end{pmatrix}, \tag{4.8}$$

where A is the wave amplitude, $\boldsymbol{r}_i$ is the position on the lattice and $\boldsymbol{k}$ is the wave vector. For simplicity, we study here single-mode spin waves. In order to handle the sum over nearest neighbors in Eq. (4.7), we use the trigonometric equalities

$$\begin{aligned} \cos\left[(\boldsymbol{r}_i + \boldsymbol{r}) \cdot \boldsymbol{k}\right] + \cos\left[(\boldsymbol{r}_i - \boldsymbol{r}) \cdot \boldsymbol{k}\right] &= 2\cos\left(\boldsymbol{r}_i \cdot \boldsymbol{k}\right)\cos\left(\boldsymbol{r} \cdot \boldsymbol{k}\right), \\ \sin\left[(\boldsymbol{r}_i + \boldsymbol{r}) \cdot \boldsymbol{k}\right] + \sin\left[(\boldsymbol{r}_i - \boldsymbol{r}) \cdot \boldsymbol{k}\right] &= 2\sin\left(\boldsymbol{r}_i \cdot \boldsymbol{k}\right)\cos\left(\boldsymbol{r} \cdot \boldsymbol{k}\right), \end{aligned} \tag{4.9}$$

so that the sum can be written as $J\sum_{\boldsymbol{r}} \delta \boldsymbol{n}_{i+\boldsymbol{r}} = C_{\boldsymbol{k}} \delta \boldsymbol{n}$. Again, we follow Ref. [91] and define $C_{\boldsymbol{k}} := 2J\left[\cos\left(k_x d\right) + \cos\left(k_y d\right)\right]$, where d is the distance between two lattice sites. Plugging the assumption Eq. (4.8) into the linearized EOM Eq. (4.7) and considering the trigonometric equations Eq. (4.9) yields

$$-\omega A \begin{pmatrix} -\sin\left(\boldsymbol{r}_i \cdot \boldsymbol{k} - \omega t\right) \\ \cos\left(\boldsymbol{r}_i \cdot \boldsymbol{k} - \omega t\right) \\ 0 \end{pmatrix} = \left(\rho - C_{\boldsymbol{k}}\right) A \begin{pmatrix} -\sin\left(\boldsymbol{r}_i \cdot \boldsymbol{k} - \omega t\right) \\ \cos\left(\boldsymbol{r}_i \cdot \boldsymbol{k} - \omega t\right) \\ 0 \end{pmatrix}. \tag{4.10}$$

This equation directly leads to the ferromagnetic spin wave dispersion relation

$$\omega(k_x, k_y) = -2J\left[2 - \cos(k_x d) - \cos(k_y d)\right] + 2K, \tag{4.11}$$

which resembles the commonly known dispersion relation [63] when assuming a vanishing anisotropy term $K = 0$. If we also assume a continuous vector field, i.e., infinitesimal small lattice constant $d \to 0$, the dispersion relation can be approximated by $|\omega| \approx J|\boldsymbol{k}|^2$. By changing the considered oscillation direction to $(\cos, -\sin, 0)$, the equation of motion can still be solved. However, the resulting frequency, $\omega' = -\omega$, is the negative of the frequency presented in Eq. (4.11). Consequently, this implies that the classical ferromagnetic spin wave has the form

$$\delta \boldsymbol{n}_i = A \begin{pmatrix} \cos\left(\pm\boldsymbol{r}_i \cdot \boldsymbol{k} - \omega t\right) \\ \sin\left(\pm\boldsymbol{r}_i \cdot \boldsymbol{k} - \omega t\right) \\ 0 \end{pmatrix}, \tag{4.12}$$

which tells us that they only oscillate with $-\omega$ in time. Thus, ferromagnetic spin waves have only one mode. Next, we will focus on antiferromagnetic spin waves.
The main difference to the previous derivation is that we have to consider the two sublattices separately. The linearized equations of motion are

$$\begin{aligned} \partial_t \delta \boldsymbol{a}_i(t) &= -\delta \boldsymbol{a}_i(t) \times \boldsymbol{H}_{i,A}^{\mathrm{eff},0} - \boldsymbol{a}_0 \times \delta \boldsymbol{H}_{i,A}^{\mathrm{eff}}(t), \\ \partial_t \delta \boldsymbol{b}_i(t) &= -\delta \boldsymbol{b}_i(t) \times \boldsymbol{H}_{i,B}^{\mathrm{eff},0} - \boldsymbol{b}_0 \times \delta \boldsymbol{H}_{i,B}^{\mathrm{eff}}(t). \end{aligned} \tag{4.13}$$

For the following, we choose the ground state to be $\boldsymbol{a}_0 = \boldsymbol{z}$ and $\boldsymbol{b}_0 = -\boldsymbol{z}$. Now we can exploit the fact that each sublattice effective field separates nicely into terms consisting of either sublattice A or B, see Eq. (4.4). Since each sublattice can be seen as a ferromagnetic lattice, we can repeat the method from the ferromagnetic case. The linearized equations of motion for each sublattice become

$$\begin{aligned} \partial_t \delta \boldsymbol{a}_i &= \rho \boldsymbol{z} \times \delta \boldsymbol{a}_i - \boldsymbol{z} \times \left[J \sum_{\boldsymbol{r}} \delta \boldsymbol{b}_{i+\boldsymbol{r}} \right], \\ \partial_t \delta \boldsymbol{b}_i(t) &= -\rho \boldsymbol{z} \times \delta \boldsymbol{b}_i + \boldsymbol{z} \times \left[J \sum_{\boldsymbol{r}} \delta \boldsymbol{a}_{i+\boldsymbol{r}} \right], \end{aligned} \tag{4.14}$$

where the homogeneous energy density is now $\rho = 2K - 4J$. We note that it has still the same form as in the ferromagnetic case since $J_{\mathrm{AFM}} = -J_{\mathrm{FM}}$. The fact that in the underlying ground state each sublattice is ferromagnetic and that the antiferromagnetic dynamics separates into two effectively coupled ferromagnetic dynamics lead us to the assumption that each sublattice should host its own ferromagnetic spin wave. Furthermore, we assume that both sublattice waves have the same frequency and phase but not necessarily the same amplitude. Therefore, we use the form of Eq. (4.8) for both sublattices, where the spin wave of sublattice A has the amplitude a and the spin wave of sublattice B has the amplitude b. That enables us to write these as $\delta \boldsymbol{a} = a\boldsymbol{\psi}$ and $\delta \boldsymbol{b} = b\boldsymbol{\psi}$, where $\boldsymbol{\psi}$ is the normalized wave form $\psi = (\cos(\boldsymbol{r}_i \cdot \boldsymbol{k} - \omega t), \sin(\boldsymbol{r}_i \cdot \boldsymbol{k} - \omega t), 0)^T$. We can, again, use Eq. (4.9) to write $J \sum_{\boldsymbol{r}} \delta \boldsymbol{a}_{i+\boldsymbol{r}} = -C_{\boldsymbol{k}} \delta \boldsymbol{a}$, and for $\delta \boldsymbol{b}$, respectively. We now, in contrast to the ferromagnetic lattice, define $C_{\boldsymbol{k}} := -2J[\cos(k_x d) + \cos(k_y d)]$ due to the sign change of J. By this we get two coupled equations of motion

$$\begin{aligned} -\omega a [\boldsymbol{z} \times \boldsymbol{\psi}] &= \rho a [\boldsymbol{z} \times \boldsymbol{\psi}] + C_{\boldsymbol{k}} b [\boldsymbol{z} \times \boldsymbol{\psi}], \\ -\omega b [\boldsymbol{z} \times \boldsymbol{\psi}] &= -\rho b [\boldsymbol{z} \times \boldsymbol{\psi}] - C_{\boldsymbol{k}} a [\boldsymbol{z} \times \boldsymbol{\psi}], \end{aligned} \tag{4.15}$$

relating to the different amplitudes a and b of the two sublattice spin waves, as well as the frequency ω. To solve this, we construct a two-dimensional vector of the amplitudes $(a, b)^T$ so that Eq. (4.15) becomes a simple eigenvalue problem in the form

$$\omega \begin{pmatrix} a \\ b \end{pmatrix} = \begin{pmatrix} -\rho & -C_{\boldsymbol{k}} \\ C_{\boldsymbol{k}} & \rho \end{pmatrix} \begin{pmatrix} a \\ b \end{pmatrix}. \tag{4.16}$$

The eigenvalues of this equation are symmetric around zero and represent the dispersion relation. They are given by $\pm\omega$ with the antiferromagnetic dispersion relation

$$\omega = \sqrt{\rho^2 - 4J^2\left[\cos(k_x d) + \cos(k_y d)\right]^2}. \tag{4.17}$$

Again, with vanishing anisotropy $K = 0$ this resembles the dispersion relation of antiferromagnetic spin waves [117]. Furthermore, assuming infinitesimally small distances between the lattice sites, $d \to 0$, yields

$$\omega^2 \approx 8J^2|\boldsymbol{k}|^2 - J^2|\boldsymbol{k}|^4 \ , \tag{4.18}$$

which can be approximated by the well-known linear dispersion relation $\omega \propto |\boldsymbol{k}|$ for small enough $|\boldsymbol{k}|$. Nevertheless, here we consider a non-vanishing anisotropy term and spin waves on a lattice with a finite lattice constant d. The eigenvalues of Eq. (4.16) are $\lambda_1 = \omega$ and $\lambda_2 = -\omega$ with the dispersion relation of Eq. (4.17). The normalized eigenvectors of Eq. (4.16) bear the symmetry that the eigenvector of λ_1 consists of $\boldsymbol{\nu}(+\omega) = (\nu_1, \nu_2)^T$ while the eigenvector of λ_2 is $\boldsymbol{\nu}(-\omega) = (-\nu_2, -\nu_1)^T$. The explicit entries,

$$\begin{aligned} \nu_1 &= \frac{-C_{\boldsymbol{k}}}{\sqrt{2\rho\left(\rho + \sqrt{\rho^2 - C_{\boldsymbol{k}}^2}\right)}} \ , \\ \nu_2 &= \frac{C_{\boldsymbol{k}}}{\sqrt{2\rho\left(\rho - \sqrt{\rho^2 - C_{\boldsymbol{k}}^2}\right)}} \ , \end{aligned} \tag{4.19}$$

are the amplitudes of the sublattice spin waves. Hence, positively oscillating spin waves, i.e., those of the mode $+\omega$, exhibit the amplitude ν_1 in the sublattice A and ν_2 in the sublattice B, while this is exactly inverted for the other mode $-\omega$. Both sublattices indeed oscillate with different amplitudes (see also Ref. [118]) and that exchanging the sublattices $A \leftrightarrow B$ would have the same result as exchanging the mode $+\omega \leftrightarrow -\omega$. In addition, Eq. (4.19) shows that the oscillation amplitude depends on the wave vector $\boldsymbol{k}$. Thus, the difference of the sublattice wave amplitudes of A and B are directly dependent on the wave vector (and frequency). In summary, we derived antiferromagnetic spin waves which circularly oscillate (equal oscillation amplitude in x and y) with different amplitudes in each sublattice. We also found that the different amplitudes depend on the wave vector and are exchanged whether we consider the mode $+\omega$ or $-\omega$. Following the established naming [119] we will call them "left-handed" $(+\omega)$ and "right-handed" $(-\omega)$ circularly polarized spin waves.

In contrast to the ferromagnetic spin waves, the antiferromagnetic spin waves can exhibit two different modes. Naturally, the question arises how spin waves of these two different modes superpose. Above, we have assumed the wave form to be as in Eq. (4.8). This leads to the two modes $\pm\omega$ and the normalized amplitudes $(a, b) = (\nu_1, \nu_2)$ for the $+\omega$ mode and $(a, b) = (-\nu_2, -\nu_1)$ for the $-\omega$ mode. Assuming, as in the ferromagnetic case,

an oppositely oscillating spin wave form

$$\begin{aligned}\delta\boldsymbol{a}' &= a(\cos\left(\boldsymbol{r}_i\cdot\boldsymbol{k}-\omega t\right), -\sin\left(\boldsymbol{r}_i\cdot\boldsymbol{k}-\omega t\right))^T,\\ \delta\boldsymbol{b}' &= b(\cos\left(\boldsymbol{r}_i\cdot\boldsymbol{k}-\omega t\right), -\sin\left(\boldsymbol{r}_i\cdot\boldsymbol{k}-\omega t\right))^T,\end{aligned} \tag{4.20}$$

leads to the same two modes $\mp\omega$. For such a wave form, the normalized amplitudes (eigenvectors) are $(a,b)=(\nu_1,\nu_2)$ for the mode $\lambda_1=-\omega$ and $(a,b)=(-\nu_2,-\nu_1)$ for $\lambda_2=\omega$. Due to the symmetry of the two modes, $\pm\omega$ for $\delta\boldsymbol{a}$ and $\mp\omega$ for $\delta\boldsymbol{a}'$, we are able to superpose the positively oscillating waves, e.g. $\delta\boldsymbol{a}(\omega)\pm\delta\boldsymbol{a}'(\omega)$, and the negatively oscillating waves, respectively. The different amplitudes with which the sublattices oscillate, with respect to the mode, create new superposition waves

$$\begin{aligned}\delta\boldsymbol{a}(\omega)\pm\delta\boldsymbol{a}'(\omega) &= \nu_1\begin{pmatrix}\cos\left(\boldsymbol{r}_i\cdot\boldsymbol{k}-\omega t\right)\\ \sin\left(\boldsymbol{r}_i\cdot\boldsymbol{k}-\omega t\right)\end{pmatrix}\mp\nu_2\begin{pmatrix}\cos\left(\boldsymbol{r}_i\cdot\boldsymbol{k}-\omega t\right)\\ -\sin\left(\boldsymbol{r}_i\cdot\boldsymbol{k}-\omega t\right)\end{pmatrix},\\ \delta\boldsymbol{b}(\omega)\pm\delta\boldsymbol{b}'(\omega) &= \nu_2\begin{pmatrix}\cos\left(\boldsymbol{r}_i\cdot\boldsymbol{k}-\omega t\right)\\ \sin\left(\boldsymbol{r}_i\cdot\boldsymbol{k}-\omega t\right)\end{pmatrix}\mp\nu_1\begin{pmatrix}\cos\left(\boldsymbol{r}_i\cdot\boldsymbol{k}-\omega t\right)\\ -\sin\left(\boldsymbol{r}_i\cdot\boldsymbol{k}-\omega t\right)\end{pmatrix}.\end{aligned} \tag{4.21}$$

These superposition waves oscillate elliptically (with different amplitudes in the x and y component). For the sake of a better overview, we define two four-component vectors $\phi_\pm=(a_x,b_x,a_y,b_y)$ which show the oscillation amplitudes for each sublattice and each component. The amplitudes for the symmetric $(+)$ and anti-symmetric $(-)$ superposition are

$$\phi_+=\begin{pmatrix}\nu_1-\nu_2\\ -(\nu_1-\nu_2)\\ \nu_1+\nu_2\\ \nu_1+\nu_2\end{pmatrix}\text{ and }\phi_-=\begin{pmatrix}\nu_1+\nu_2\\ \nu_1+\nu_2\\ \nu_1-\nu_2\\ -(\nu_1-\nu_2)\end{pmatrix}, \tag{4.22}$$

while the oscillation in space and time of the wave is still of the form from Eq. (4.8). There are some peculiarities to notice. The absolute value of the amplitude is the same for both sublattices, A and B, however different for the two components. The change of the superposition sign (whether symmetric or anti-symmetric superposition) has the same effect as a component exchange $x\leftrightarrow y$. Therefore, it is sufficient to only regard ϕ_+ for the following explanations. From Eq. (4.22) we see that $a_x=-b_x$ while $a_y=b_y$. This has the consequence that the wave on the sublattice A oscillates in the opposite direction as compared to the wave of the sublattice B. This is the crucial difference to circularly polarized spin waves where both sublattices precess in the same direction.

To set this behavior in context, we regard, as a digression, the staggered magnetization $\boldsymbol{l}=(\boldsymbol{a}-\boldsymbol{b})/2$ and the magnetization $\boldsymbol{m}=(\boldsymbol{a}+\boldsymbol{b})/2$. The staggered magnetization $\boldsymbol{l}$ is an order parameter of the antiferromagnetic phase and $\boldsymbol{m}$ is the magnetization the lattice exhibits viewed from a sufficiently large distance. These two vectors are often used in the context of antiferromagnetic textures (see, e.g., Refs. [27, 31, 106, 120]). While the staggered magnetization is usually renormalized $\boldsymbol{n}=\boldsymbol{l}/|\boldsymbol{l}|$ [120] and defines the struc-

ture (e.g. Skyrmion, domain wall), the magnetization is assumed to be very small [31]. Regarding the superposed antiferromagnetic spin waves ϕ_+ and ϕ_-, see Eq. (4.22), in the sense of magnetization and staggered magnetization, it turns out that the staggered magnetization, as the order parameter, *exclusively* oscillates in x direction for ϕ_+. Thus, we will call the positively superposed waves "x linearly polarized" spin waves, following Ref. [119]. Consequently, we call negatively superposed waves "y linearly polarized" spin waves. The respective magnetization wave $\delta\boldsymbol{m}$ oscillates perpendicular to the staggered magnetization wave, i.e., only in the other component. This is the reason for naming them "linearly polarized", due to the analogy to electromagnetic waves [121]. Naturally, the circularly polarized spin waves can also be examined using $\delta\boldsymbol{l}$ and $\delta\boldsymbol{m}$. Both vectors oscillate circularly with the same frequency and direction, but with different amplitude. The staggered magnetization oscillates with an amplitude $\nu_1 - \nu_2$, while the magnetization oscillates with a lower amplitude $\nu_1 + \nu_2$.

Spin waves with non-vanishing damping

So far, we only considered spin waves in a dissipation free system. However, in real systems there would be a non-vanishing damping $\alpha > 0$. To derive how damping affects the spin waves, we add the damping term $\propto \alpha$ to the linearized equation of motion,

$$\partial_t \delta\boldsymbol{n}_i(t) = -\delta\boldsymbol{n}_i(t) \times \boldsymbol{H}_i^{\mathrm{eff},0} - \boldsymbol{n}_0 \times \delta\boldsymbol{H}_i^{\mathrm{eff}}(t) + \alpha \boldsymbol{n}_0 \times \partial_t \delta\boldsymbol{n}_i(t). \tag{4.23}$$

Additionally, we employ complex numbers, assuming that the actual spin wave corresponds to the real part of a complex wave, so that $\delta\boldsymbol{n} = A\Re(\boldsymbol{\psi})$. The complex wave is

$$\boldsymbol{\psi} = \begin{pmatrix} 1 \\ i \\ 0 \end{pmatrix} \exp\left(-i\left[\boldsymbol{k}\boldsymbol{r} - \omega t\right]\right). \tag{4.24}$$

As for the non-damped system, we start with ferromagnetic spin waves and expand this formalism to antiferromagnetic spin waves. Following the derivation from above, especially Eqs. (4.5) and (4.9), we get the equation of motion

$$i\omega\boldsymbol{\psi} = (\rho - C_{\boldsymbol{k}})\boldsymbol{z} \times \boldsymbol{\psi} + i\omega\alpha \boldsymbol{z} \times \boldsymbol{\psi}. \tag{4.25}$$

Regarding Eq. (4.24) we see that $\boldsymbol{z} \times \boldsymbol{\psi}$ is the same as $-i\boldsymbol{\psi}$. Using this in Eq. (4.25), we get an equation for the frequency

$$\omega = \frac{-1}{1 + i\alpha}\left(\rho - C_{\boldsymbol{k}}\right). \tag{4.26}$$

Applying the commonly used small-damping approximation $\alpha \ll 1$, we approximate the pre-factor $\frac{1}{1+i\alpha} \approx 1 - i\alpha$. Furthermore, we use the dispersion relation from the non-damped case, Eq. (4.11), and call it ω_0. This leads to a complex frequency of $\omega = -(1 - i\alpha)\omega_0$. If

we plug this back in the assumed wave form in Eq. (4.24), we find

$$\boldsymbol{\psi} = \begin{pmatrix} 1 \\ i \\ 0 \end{pmatrix} \exp\left(-i\left[\boldsymbol{k}\boldsymbol{r} + \omega_0 t - i\alpha\omega_0 t\right]\right). \tag{4.27}$$

Thus, the damped ferromagnetic spin wave is the same as the non-damped FM spin wave with an additional time dependent damping factor. Concretely it is

$$\delta\boldsymbol{n}_{\text{damped}}(t) = \delta\boldsymbol{n}_{\text{free}}(t)\exp(-\alpha\omega_0 t). \tag{4.28}$$

The strength of the damping over time depends on the frequency and, thus, on the wave vector $\boldsymbol{k}$. In conclusion, for ferromagnetic spin waves the Gilbert damping α affects the spin wave in a non-surprising way. An initially excited wave would be damped over time exponentially with a damping (or decay-) time constant $t_d = 1/(\alpha\omega_0)$. From this one can clearly see that a lower damping, as expected, increases the decay time t_d. Interestingly, the decay time is inversely proportional to the spin wave frequency, leading to faster decay of faster oscillating waves.
Next we derive the damped antiferromagnetic spin waves [91]. For this, we assume that both sublattices are governed by the LLG equation with the same damping parameter α [103]. Thus, we add the damping term to the previously derived equations of motion, Eq. (4.14), so that the EOM is now

$$\begin{aligned} \partial_t\delta\boldsymbol{a}_i &= \rho\boldsymbol{z}\times\delta\boldsymbol{a}_i - \boldsymbol{z}\times\left[J\sum_{\boldsymbol{r}}\delta\boldsymbol{b}_{i+\boldsymbol{r}}\right] + \alpha\boldsymbol{a}_0\times\partial_t\delta\boldsymbol{a}, \\ \partial_t\delta\boldsymbol{b}_i(t) &= -\rho\boldsymbol{z}\times\delta\boldsymbol{b}_i + \boldsymbol{z}\times\left[J\sum_{\boldsymbol{r}}\delta\boldsymbol{a}_{i+\boldsymbol{r}}\right] + \alpha\boldsymbol{b}_0\times\partial_t\delta\boldsymbol{b}\ . \end{aligned} \tag{4.29}$$

As in the ferromagnetic case, we assume that the sublattice waves have the form from Eq. (4.27), however with different amplitudes. Therefore, we write the sublattice waves, similar to the non-damped case, as $\delta\boldsymbol{a} \to a\boldsymbol{\psi}$ and $\delta\boldsymbol{b} \to b\boldsymbol{\psi}$. Plugging these forms into Eq. (4.29), we find the system of equations

$$\begin{aligned} i\omega a\boldsymbol{\psi} &= \left[\rho a + C_{\boldsymbol{k}} b + i\alpha\omega a\right]\boldsymbol{z}\times\boldsymbol{\psi}, \\ i\omega b\boldsymbol{\psi} &= \left[-\rho b - C_{\boldsymbol{k}} a - i\alpha\omega b\right]\boldsymbol{z}\times\boldsymbol{\psi}\ . \end{aligned} \tag{4.30}$$

Each row in Eq. (4.30) has the same structure as Eq. (4.25) from the derivation of ferromagnetic damped waves. Therefore, this leads to

$$\begin{aligned} \omega a(1 + i\alpha) &= -\rho a - C_{\boldsymbol{k}} b, \\ \omega b(1 - i\alpha) &= \rho b + C_{\boldsymbol{k}} a. \end{aligned} \tag{4.31}$$

By applying the approximations $\frac{1}{1+i\alpha} \approx (1 - i\alpha)$ and $\frac{1}{1-i\alpha} \approx (1 + i\alpha)$ (see explanation above), we can construct an eigenvalue problem,

$$\omega \begin{pmatrix} a \\ b \end{pmatrix} = \begin{pmatrix} -\rho(1 - i\alpha) & -C_{\boldsymbol{k}}(1 - i\alpha) \\ C_{\boldsymbol{k}}(1 + i\alpha) & \rho(1 + i\alpha) \end{pmatrix} \begin{pmatrix} a \\ b \end{pmatrix}, \tag{4.32}$$

which is similar to the non-damped eigenvalue problem of Eq. (4.16). Again, it is convenient to make use of the dispersion relation of the non-damped case ω_0 of Eq. (4.17). The eigenvalues of Eq. (4.32) are

$$\omega_\pm = i\alpha\rho \pm \omega_0. \tag{4.33}$$

Plugging this back into Eq. (4.24) shows that the non-vanishing Gilbert damping results in an exponentially damped spin wave $\propto \boldsymbol{\psi} \exp(-\alpha\rho t)$. In contrast to the ferromagnetic spin wave, the damping of the antiferromagnetic wave does *not* depend on the frequency but solely on the damping parameter and ρ. Additionally, there exists another peculiarity for the case of damped antiferromagnetic spin waves. The entries of the eigenvectors $\boldsymbol{\nu}(\omega_\pm)$ are real numbers in the case of non-damped spin waves, however, they are complex in the case of non-vanishing damping. Using Eq. (4.19), the normalized eigenvectors for damped antiferromagnetic spin waves are

$$\boldsymbol{\nu}(\omega_+) = \begin{pmatrix} \nu_1 \\ \nu_2(1 + i\alpha) \end{pmatrix} \text{ and } \boldsymbol{\nu}(\omega_-) = \begin{pmatrix} -\nu_2 \\ -\nu_1(1 + i\alpha) \end{pmatrix} . \tag{4.34}$$

Since the eigenvectors represent the normalized amplitudes of the spin waves, one would not expect them to be complex numbers. However if we regard, for instance, the mode ω_+, the spin wave amplitude in sublattice A is the same as in the non-damped case, namely ν_1. The complex entry refers to the amplitude of the sublattice B wave. Using this amplitude in combination with the assumed wave form Eq. (4.24) yields

$$b\boldsymbol{\psi} = \nu_2 \left[\begin{pmatrix} 1 \\ i \\ 0 \end{pmatrix} + \alpha \begin{pmatrix} i \\ -1 \\ 0 \end{pmatrix} \right] \exp[-i(\boldsymbol{kr} - \omega_+ t)]. \tag{4.35}$$

The spin waves are excitations created by classical dynamics of three dimensional vectors living in the real space. Thus, they can not consist of complex numbers. As explained above, using the complex number space was only for the calculation; while the spin wave is only the real part of the complex function $\delta\boldsymbol{b} = \Re(b\boldsymbol{\psi})$. Therefore, the real spin wave created by the ω_+ mode can be calculated from Eq. (4.35) and is

$$\delta\boldsymbol{b} = \nu_2 \begin{pmatrix} \cos(\boldsymbol{kr} - \omega t) + \alpha \sin(\boldsymbol{kr} - \omega t) \\ \sin(\boldsymbol{kr} - \omega t) - \alpha \cos(\boldsymbol{kr} - \omega t) \\ 0 \end{pmatrix} \exp[-\alpha\rho t)]. \tag{4.36}$$

In order to compare this to the other sublattice spin wave, we use

$$\begin{aligned}\cos x + \alpha \sin x &= \sqrt{1+\alpha^2}\cos(x + \arctan(-\alpha)),\\ \sin x - \alpha \cos x &= -\sqrt{1+\alpha^2}\cos(x + \arctan(1/\alpha)).\end{aligned} \tag{4.37}$$

Assuming realistically small damping $\alpha \ll 1$, we approximate $\sqrt{1+\alpha^2} \approx 1$ as well as $x + \arctan(-\alpha) \approx x - \alpha$ and $x + \arctan(1/\alpha) \approx x + \frac{\pi}{2} - \alpha$. In summary, this yields for the spin wave in the sublattice B

$$\delta \boldsymbol{b} = \nu_2 \begin{pmatrix} \cos(\boldsymbol{kr} - \omega t - \alpha) \\ \sin(\boldsymbol{kr} - \omega t - \alpha) \\ 0 \end{pmatrix} \exp[-\alpha\rho t)], \tag{4.38}$$

while the spin wave on sublattice A is the same as in the non-damped case with a damping factor. That means the damping creates a small phase shift of order the damping parameter α to one of the sublattice spin waves. Although this phase shift is marginal, one should note that at non-vanishing damping the two sublattice spin waves are off-phase.

4.3. Numerical simulation of spin waves

The simulations were done for a single layer square lattice and with the same Hamiltonian as in the analytical calculations of the previous sections. A detailed explanation of the simulation methods is given in the Appendix A. The advantage of simulating classical magnetic spin dynamics is that we have access to each lattice spin at each time point. We use that access to artificially induce spin waves into the lattice which is initially in the ground state. To this end, we drive the spins on the left edge into oscillations so that a spin wave will be created which travels into the lattice. More precisely, we prepared the lattice in the classical (anti-) ferromagnetic ground state and enforce closed boundary conditions $\partial_t \boldsymbol{n}_{\text{edge}} = 0$. To induce a spin wave into the lattice we manipulate the entries of the spins on the left lattice edge so that

$$\boldsymbol{n}_{\text{drive}}(t) = \begin{pmatrix} A_x \cos(\omega t) \\ A_y \sin(\omega t) \\ \sqrt{1 - A_x^2 \cos^2(\omega t) - A_y^2 \sin^2(\omega t)} \end{pmatrix}, \tag{4.39}$$

where the oscillation amplitudes A_x, A_y and the oscillation frequency ω are tunable parameters. To create circularly polarized spin waves, we chose the oscillation amplitude in x and y direction to be equal, $A_x = A_y$, and small ($A_x/M_S = 0.05$). To create linearly polarized spin waves, on the other hand, only one oscillation direction has to be non-zero, e.g., $A_x/M_S = 0.05$ and $A_y = 0$ for x-linearly polarized spin waves. The manipulation of edge spins is a common tool [115, 116] and done here so that we can inject mono-chromatic spin waves in a controlled manner.

The precession of the leftmost edge spin induces a precession of its neighboring spins, which in turn causes their respective neighbors to precess, continuing the effect throughout the system. Thus, a spin wave travels into the lattice along the x axis. The spin wave has two frequencies which we have to carefully distinguish. One is the frequency ω with which each single spin precesses in time. The other parameter is the wave number k (in this case $k = k_x$ and $k_y = 0$), which represents the periodicity in space that the spin wave exhibits over the lattice. In Fig. 4.1 plots of both cases for a circularly polarized spin wave are shown. The upper plot shows the x component of one magnetic moment from each sublattice over time, while the lower plot shows the x components of one row of magnetic moments along the lattice in x direction of each sublattice. The oscillation takes place in

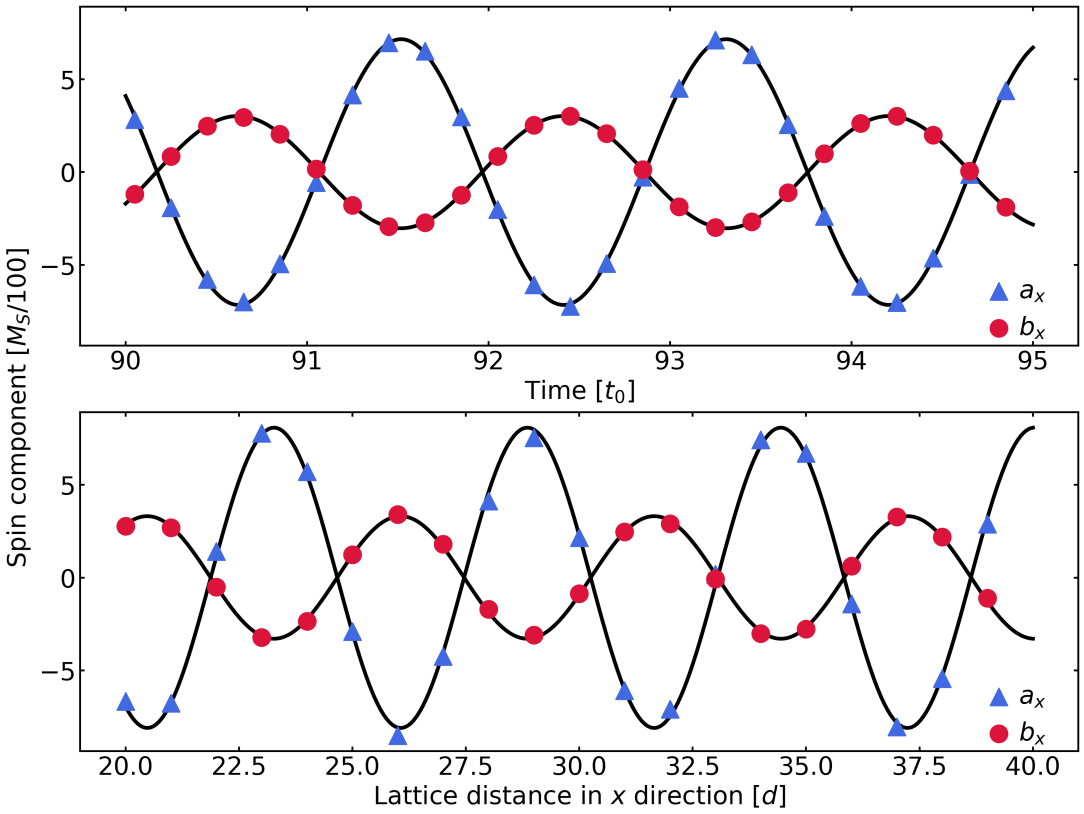

Figure 4.1.: The symbols show the x component of one magnetic moment from each sublattice (blue triangle A, red circle B) over time t (upper plot) and over the lattice in x direction (lower plot). The solid lines are sine fits to the respective symbols.

both time and space and with different amplitudes for each of the two sublattices. The dispersion relation, Eq. (4.17), of the classical spin wave connects the precession frequency ω and the wave number k. To verify Eq. (4.17) we simulated spin waves with different values for the parameter ω. After a sufficiently long simulation time we took a snap shot of the lattice, i.e., we have an $L_x \times L_y$ data array with a three-dimensional vector in each entry. In order to get the spin wave of each single sublattice we took the n^{th} row and the $(n+1)^{\text{th}}$ row of the lattice along x direction. The former starts with a vector of the sub-

lattice A while the latter starts with a vector of the sublattice B since neighboring lattice sites are from different sublattices. Subsequently, we eliminate each second entry of each of both rows, so that they only have entries of one respective sublattice. The resulting waves are the waves which live on the respective sublattice and can be compared to a ferromagnetic spin wave. For each driving frequency ω we fitted the resulting sublattice waves to a sine function. The fitted function, $A\sin(kx + \varphi_0)$, can be described by three parameters; the amplitude A, the wave vector k and the phase φ_0. Therefore, for each simulation we can assign a wave vector k stemming from a driving amplitude ω, so that there are data tuples (ω, k). These data tuples are plotted as blue dots in Fig. 4.2 for ferromagnetic and antiferromagnetic spin waves. Because these are essentially the classical dispersion relation, the analytically derived dispersion relation is also plotted as a solid line. The left plot shows the simulation results and the dispersion relation Eq. (4.11) of a

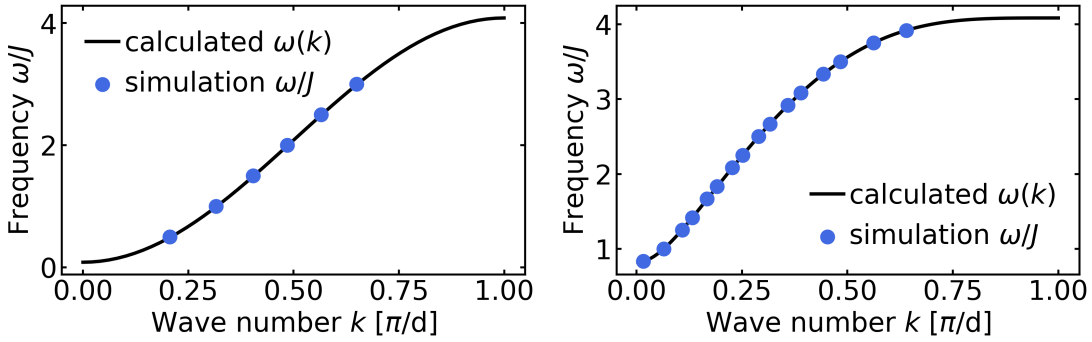

Figure 4.2.: Dispersion relation $\omega(k)$ of a classical ferromagnetic (left) and antiferromagnetic (right) spin wave. The dots are data tuples (ω, k) derived from simulations while the solid lines are the dispersion relation from Eqs. (4.11) and (4.17), respectively.

ferromagnetic lattice while the right plot shows the simulation results and the dispersion relation Eq. (4.17) of an antiferromagnetic lattice. It is clearly visible that the analytical calculations match the simulations perfectly.

As explained above the antiferromagnetic spin waves can be differently polarized. We recover these properties in the simulations as well. Choosing the same value for the oscillation of the x and y component of the edge spins leads to circularly polarized spin waves. Although we drove the edge spins of each sublattice with the same driving amplitude, the resulting circularly polarized spin wave shows different amplitudes in the sublattices A and B (see Fig. 4.1). The fact that the different sublattices oscillate with different amplitudes is known in the literature [118] and we derived an explicit expression for this in Eq. (4.19). Not shown here, but tested in the simulations, is that changing the oscillation direction $\omega \to -\omega$ leads to an interchange in the sublattice amplitudes $(a, b) \to (b, a)$. The sine function fitted to the wave from the simulation yields an amplitude for each sublattice, $a_x = a_y$ and $b_x = b_y$. Following the analytical derivation of circularly polarized spin waves above, the normalized amplitude $\tilde{a}_x = a_x/\sqrt{a_x^2 + b_x^2}$ should be the same as the normalized component ν_1 of the eigenvector from Eq. (4.19), while $\tilde{b}_x = b_x/\sqrt{a_x^2 + b_x^2}$ should be

ν_2, respectively. To validate this, we plot the normalized amplitudes, extracted from the simulation, and the components of the eigenvector from Eq. (4.19) in dependence of k in Fig. 4.3 (left). One can see that the amplitudes from the simulated wave (symbols) match with the calculated eigenvector components (solid lines). For all wave numbers the two

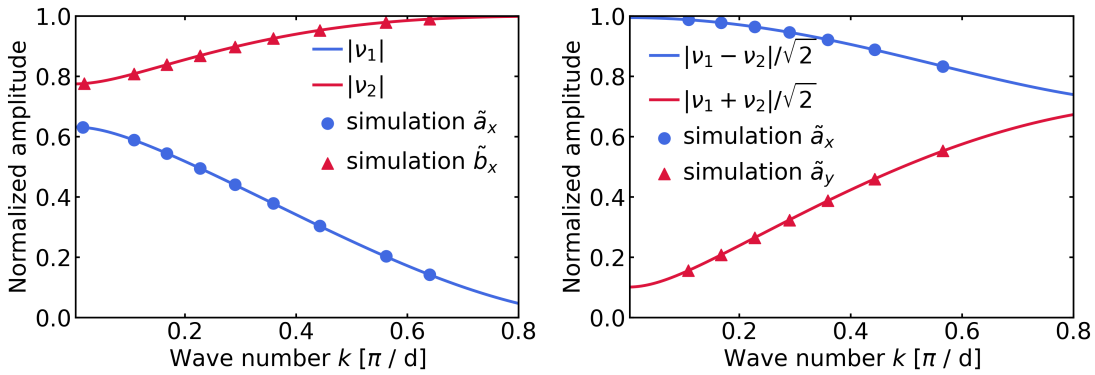

Figure 4.3.: Normalized amplitudes of a circularly polarized (left) and a linearly polarized (right) AFM spin wave. The symbols show the fitted wave amplitudes from the simulations adapted to $\tilde{a}_x = a_x/\sqrt{a_x^2 + b_x^2}$ (left) and $\tilde{a}_x = a_x/\sqrt{a_x^2 + a_y^2}$ (right), respectively. The solid lines are calculated with the eigenvector components of Eq. (4.19).

sublattice amplitudes are different from each other. Furthermore, which sublattice hosts the more intense wave, i.e., the wave with the larger amplitude, remains the same for each value of $k \in [0, \pi]$. This is a crucial fact to be considered when it comes to spin wave - Skyrmion interaction since both sublattices differ only in the spin wave amplitude.

In order to create linearly polarized spin waves in the simulation, we drive the edge spins only in one component - the x component for x linearly polarized spin waves or the y component for y linearly polarized spin waves. Even though we did not drive spins in the suppressed component, the spin wave naturally forms in this component along the lattice. Furthermore, the resulting spin wave exhibits all properties of linearly polarized spin waves derived in the analytical calculations in Sec. 4.2. While the oscillation direction in sublattice A is opposite of sublattice B, the amplitudes have the same magnitude. Therefore, it is sufficient to only regard sublattice A for the following analysis. Of interest here are the amplitudes of the two components x and y. The value of both (normalized) amplitudes, $\tilde{a}_x = a_x/\sqrt{a_x^2 + a_y^2}$ and $\tilde{a}_y = a_y/\sqrt{a_x^2 + a_y^2}$, is a measure of the ellipticity of the oscillation and is derived above in Eq. (4.22). In Fig. 4.3 (right) it is shown that the simulated wave amplitudes (symbols) coincide with the analytically calculated amplitudes from Eq. (4.22). Not shown here, but tested, is that the simulations also have the symmetry implied by Eq. (4.22).

Finally, we aim to simulate the case of spin waves at non-vanishing damping $\alpha > 0$ for both ferromagnetic and antiferromagnetic lattices. At this point we have to take the creation of the spin waves in our simulations into account. Typically, the origin of the spin wave would relax when it is not longer driven. Due to the artificial edge spin driving we have a

permanently driven initial spin of the waves. This means a constant driving at the edge position $x = 0$ with the consequence of a permanent stream of a spin wave into the lattice which is damped along it propagation path. In Fig. 4.4 a snapshot of the two sublattice spin waves of a circularly polarized antiferromagnetic spin wave along the x direction of the lattice is shown. The symbols represent the x component of each spin along the x

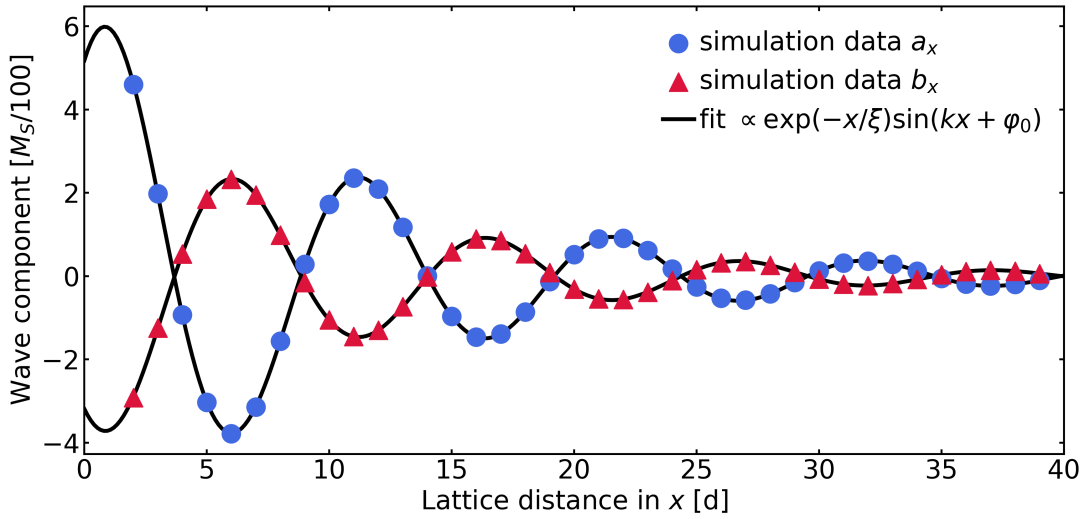

Figure 4.4.: Propagation of a damped circularly polarized AFM spin wave along the lattice. The symbols represent the x component of the wave in each sublattice (blue circles A, red triangles B). The solid lines are fits to a damped wave function.

direction while the solid lines are fits to the damped wave function $\exp(-x/\xi)\sin(kx+\varphi_0)$. The parameter k is the wave vector of the spin wave and coincides with the wave vector from the non-damped cases. The parameter ξ specifies the length at which the wave is damped by the factor $1/e$ and is therefore referred to as the decay length. In the derivation of the classical spin wave formalism in Sec. 4.2, we calculated the damping over time. To compare it with the simulation, we have to calculate the course over the lattice of the spin wave. We assume the spin waves traveling with constant velocity $v_g = \partial\omega/\partial k$. Regarding the Eqs. (4.11) and (4.17) the velocities are

$$v_{\mathrm{FM}} = 2dJ\sin(kd), \tag{4.40}$$

$$v_{\mathrm{AFM}} = \frac{4dJ^2\sin(dk)\left[\cos(dk)+1\right]}{\sqrt{(2K-4J)^2-4J^2(\cos(dk)+1)^2}}\,. \tag{4.41}$$

Note that these velocities are already adapted to the simulations where $\boldsymbol{k} = k\boldsymbol{x}$ and $k_y = 0$. With these equations we calculate the traveling time of the wave front $t = x/v$ and can plug it into the derived damped wave form $\psi\exp(-\Gamma t)$. Thus, we can calculate the decay length $\xi = v/\Gamma$ from the corresponding damping over time, see Eqs. (4.28) and (4.38), and the corresponding group velocity from Eqs. (4.40) and (4.41). In the ferromagnetic lattice, the damping over time $\Gamma_{\mathrm{FM}} = \alpha\omega_0$ depends on the dispersion relation and leads

to a decay length of

$$\xi_{\mathrm{FM}} = \frac{Jd\sin(kd)}{\alpha\left(J - J\cos(kd) + K\right)}, \tag{4.42}$$

which depends on the wave number k. The damping over time for antiferromagnetic spin waves, $\Gamma_{\mathrm{AFM}} = \alpha\rho$, does not depend on the oscillation frequency ω, so that it is essentially a re-scaled group velocity. Since the velocity of the antiferromagnetic spin wave depends on the wave number k, the decay length

$$\xi_{\mathrm{AFM}} = \frac{2dJ^2\sin(kd)\ [\cos(kd)+1]}{\alpha(K-2J)\sqrt{(4J-2K)^2 - 4J^2(\cos(kd)+1)^2}} \tag{4.43}$$

also does. As shown exemplary in Fig. (4.4), the simulated waves can be fitted to a damped wave. Thereby, we were able to extract the decay length ξ and the wave number k from the fits and plot these parameters against each other. In Fig. 4.5 the decay length of ferromagnetic spin waves (left) and antiferromagnetic spin waves (right) are plotted against the wave number k. The dots are the data taken from the fits while the solid lines are the decay length calculated with Eq. (4.42) and Eq. (4.43), respectively. The

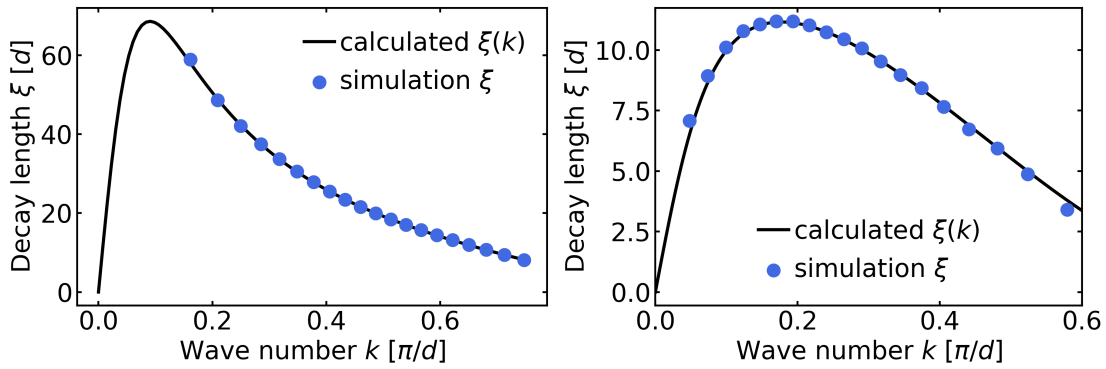

Figure 4.5.: Decay length ξ of a ferromagnetic (left) and an antiferromagnetic (right) spin wave. The dots are the fitting parameters k and ξ plotted against each other while the solid line is the decay length calculated by Eqs. (4.42) and (4.42), respectively.

simulations verify the analytical calculations. Interestingly, the decay length for both FM and AFM strongly depends on the wave number k and, thus, on the frequency ω. In the case of ferromagnetic spin waves we were not able to simulate spin waves with $k < 0.2\pi$ due to the low slope of the dispersion relation (see Fig. 4.2 left). Therefore, we were not able to verify the sudden drop of the decay length for wave numbers lower than 0.2π. Despite this, ferromagnetic spin waves have a significant shorter reach the higher the wave number k is. From this we could derive a rule of thumb that waves with lower frequency (or longer wave length) will travel farther than those with higher frequency (or shorter wave length). This is in contrast to technical applications where high-frequency spin waves with low decay are favored [122]. Unlike ferromagnetic spin waves, the decay length of the antiferromagnetic spin waves does not follow this rule. Antiferromagnetic spin waves

seem to have a range of wave numbers around $k \approx 0.2\pi$ where the decay length is at its max and roughly constant. If the wave number is too far away from this sweet spot, the decay length decreases. This consideration is important in the context of long-range spin waves observed in experiments.

4.4. Spin wave - skyrmion interaction: circularly polarized spin waves

In chiral magnets, which are known to support the formation of Skyrmions [5], there exist intricate magnon-Skyrmion bound states alongside a continuous spectrum of free magnons [123]. This fact suggests that Skyrmions interact with spin waves and, indeed, it was found that magnons scatter at Skyrmions [62, 112]. Since Skyrmions move at non-zero temperature [110], it is intriguing to know how magnons, which will be created at non-zero temperatures [cf. 124], influence the Skyrmion motion. The ferromagnetic magnon-induced Skyrmion motion is studied in detail using the continuum approach in Refs. [62, 112, 123]. A detailed study on a discrete lattice focusing on the impact of the lattice constant remains elusive. The impact of magnons on Skyrmions in an antiferromagnetic system has been studied using the continuum approach in Ref. [125] as well as using a discrete bipartite lattice in Ref. [91].

In this thesis, we simulate how a continuous spin wave impacts an isolated Skyrmion. The model is the same as in the previous sections and technical details of the simulation can be found in Appendix A. To study the magnon-Skyrmion interaction, we create a stationary single Skyrmion in the lattice. Subsequently, we inject a continuous stream of a mono-chromatic spin wave from the left lattice edge as explained in Sec. 4.3. This spin wave travels into the lattice and scatters at the Skyrmion. An example of the procedure can be found in Fig. 4.6. It depicts two snapshots of one of the sublattices at two different time points. The color represents the x components of each lattice spin n_i^x cut off at 0.4 for the sake of visibility. The left picture shows how the spin wave travels from the left to the right edge along the x direction while the Skyrmion is resting near the left lattice side. The right picture shows the lattice at a later time where the spin wave has already passed the Skyrmion. It can be seen that the spin wave scatters at the Skyrmion and also moves it. The two snap shots in Fig. 4.6 serve only as examples for the general procedure. A video of how a spin wave moves a Skyrmion can be found in the supplemental material of Ref. [91]. In the following we will focus on the resulting Skyrmion motion. To this end, we focus on the path traveled by the Skyrmion over time.

Circularly polarized antiferromagnetic spin waves drive the Skyrmion along both the x and the y direction. The resulting Skyrmion motion is depicted in Fig. 4.7 (left plot) showing the traveled distance in the x and y direction. In both directions the traveled distance over time depicts a parabola resembling an accelerated motion $s(t) = \frac{a}{2}t^2 + v_0 t + s_0$ with a constant acceleration a. This acceleration acts as a quantifier of the force acting on

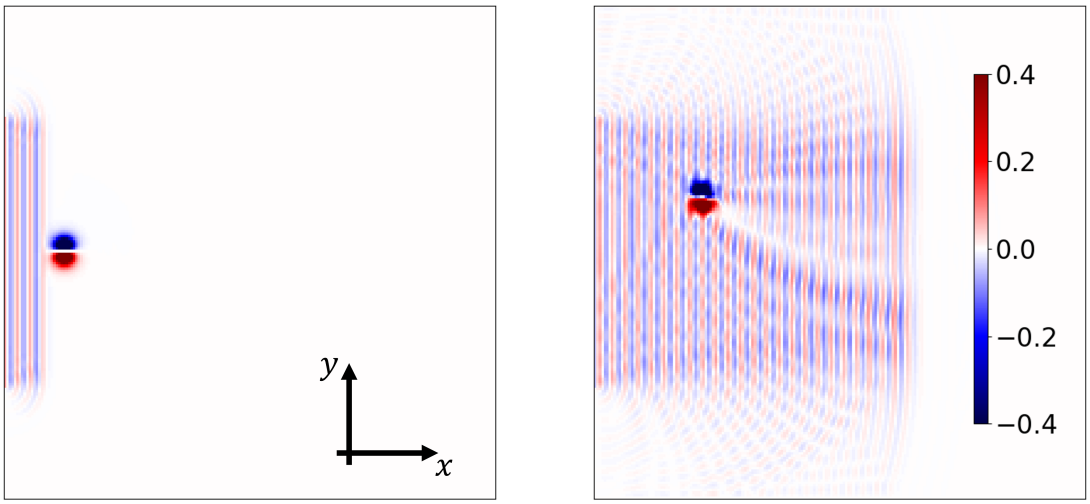

Figure 4.6.: Snapshots of the x component of each spin n_x on one sublattice at two different times $t_1 < t_2$. The left plot, at time t_1, shows a single resting Skyrmion and the spin wave which travels into the lattice along the x direction. The right plot, at time t_2, shows a situation where the spin wave already scattered at the Skyrmion and moved it along the lattice.

the Skyrmion [91]. Since we create the spin waves as explained in Sec. 4.3, we can tune the driving frequency ω as well as the driving amplitude A_0 of the spin wave. In Fig. 4.7 (right plot) the resulting Skyrmion acceleration in dependency of the driving amplitude is shown. It confirms the intuition that spin waves with higher amplitudes accelerate the Skyrmion faster. The Skyrmion motion also depends on the wave number k of its driving

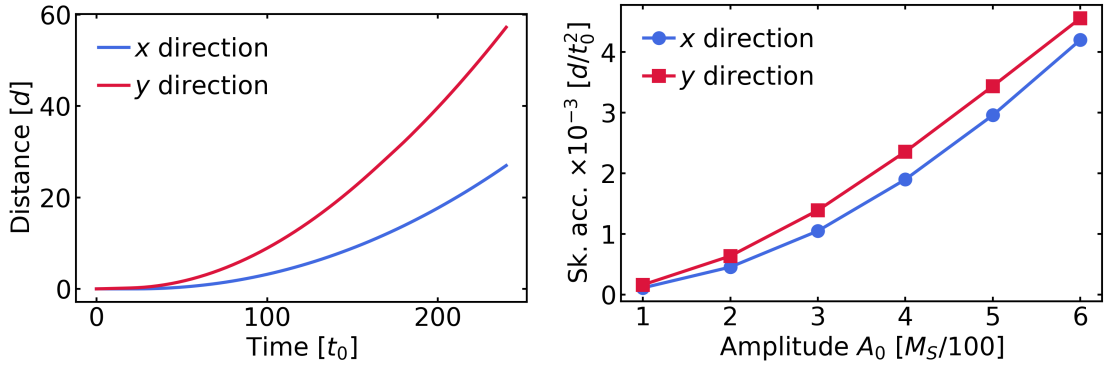

Figure 4.7.: Left: Distance the Skyrmion traveled over time in x (blue) and y direction (red) of the lattice. Right: The fitted acceleration of the Skyrmion motion in x (blue) and y (red) direction in dependence of the applied spin wave amplitude A_0.

wave. To study this we tune the driving frequency ω while keeping the driving amplitude fix at $0.02M_S$. The respective wave number is calculated from the dispersion relation in Eq. (4.17). The resulting Skyrmion acceleration in x and y direction in dependence of the wave number is shown in Fig. 4.8 (left plot). It turns out that higher wave numbers, i.e. shorter wave lengths, lead to faster Skyrmion acceleration as long as $k \leq 0.4\pi$. Regarding

Fig. 4.7, we note that at larger Skyrmion velocities it is not possible to fit the traveled distance over time to a square function. This deviation suggests that the acceleration ceases to be constant after some time. That is due to the emergence of other effects. For instance, due to the Doppler effect the moving Skyrmion can experience a spin wave with an effectively larger wave length. This lowers the acceleration of the Skyrmion depending on its velocity. Since analyzing this more complicated motion is outside the scope of this thesis, we only examined scenarios where the resulting Skyrmion motion is slow enough to be fitted against a constant acceleration. The left plot of Fig. 4.8 shows that the Skyrmion

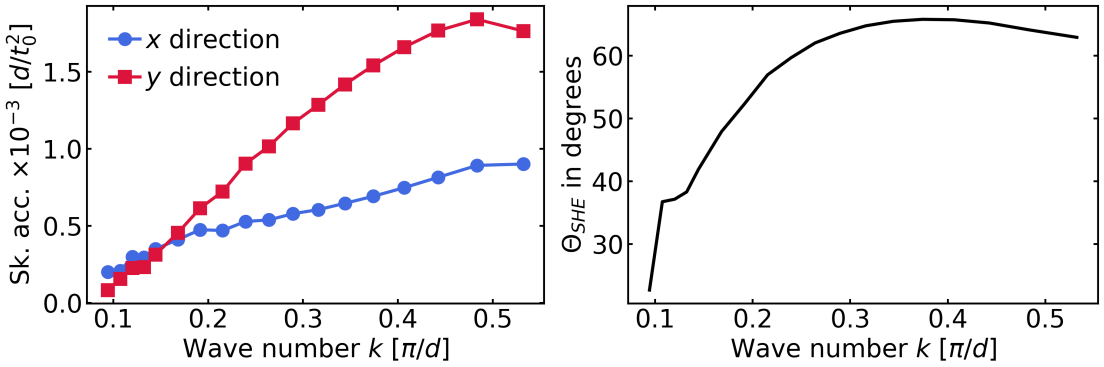

Figure 4.8.: Left: The resulting Skyrmion acceleration, extracted by fitting the simulation data, is shown as a function of the applied spin wave number k for the x (blue circles) and y (red squares) directions. Right: Skyrmion Hall angle in dependence on the wave number k.

acceleration in x and y direction individually depends on k. It has the consequence that the Skyrmion will be accelerated with a non-zero angle to the spin wave propagation direction, with the actual angle depending on the wave number k or the frequency ω, respectively. This effect is called the Skyrmion Hall effect[2] (SHE) for spin wave driven Skyrmions [91, 125]. In the right plot of Fig. 4.8 the quantity of the SH angle is shown in degree and in dependence on the wave number k. Its dependence of the spin wave frequency ω can be seen in Ref. [91] (or similar Ref. [125]). For wave numbers up to $k \approx 0.5\pi$ the SH angle increases monotonously with the wave number, except in the low-frequency range. Although the small "hump" [91] in the low frequency regime can not be traced back to numerical errors, one should keep in mind that the absolute acceleration of the Skyrmion there is rather small. We found that changing the oscillation direction $\omega \to -\omega$ only influences the resulting Skyrmion motion in y direction and only in such a manner that it reverses its direction. Concretely, the force reverses with handedness $F_\perp(\omega) = -F_\perp(\omega)$ while $F_\parallel(\omega) = F_\parallel(\omega)$. Thus, the sign of the Skyrmion Hall angle depends on the sign of the driving spin wave frequency ω.

[2]The term Skyrmion Hall effect is not well-defined. Since the field of spin wave driven Skyrmions is relatively young, there is no particular term for the spin wave induced Skyrmion Hall effect.

4.5. Technical application

Due to their small sizes, relatively high stability and the ability to be moved at high velocities, magnetic Skyrmions are often advertised as useful for technological application [84]. For example, they can be used as information carriers with one Skyrmion representing one bit. A promising architecture to transport Skyrmions is a so-called Skyrmion racetrack. Originally, it was proposed Parkin *et al.* in Ref. [8] as an architecture for domain walls as information carriers, but with the increasing popularity of Skyrmions the idea of a Skyrmion racetrack arose [105]. Therefore, the field of studying magnetic Skyrmions was inspired by their potential practical uses, in addition to purely academic interests. Topics of how to create [17, 115, 116, 126] and annihilate (delete) Skyrmions [17, 115, 116], as well as how to efficiently move Skyrmions [98], emerged. A typical Ansatz is to move Skyrmions by electric current (see Sec. 2.1) with the drawback that FM Skyrmions experience a Skyrmion Hall effect when they are driven by an electric current [45]. A solution to overcome the current-induced SHE is to use antiferromagnetic systems [27] since the current induced SHE is a ferromagnetic phenomenon [53]. For spin wave driven Skyrmions, however, the Skyrmion Hall effect is present in ferromagnetic and antiferromagnetic systems. In the following, a concept will be explained in which we exploit the non-vanishing SHE in order to move an antiferromagnetic Skyrmion along a racetrack using spin waves. This concept is also explained in Ref. [91].

Realistic systems exhibit a non-vanishing damping, which has to be considered in concepts regarding possible technological application. Figure 4.4 shows the impact of damping on a spin wave propagating through a lattice. Since the Skyrmion acceleration highly depends on the spin wave amplitude (see Fig. 4.7), the Skyrmion will be less and less accelerated the farther it moves from the spin wave source. At some point the Skyrmion travels without external driving and will, because the Skyrmion motion itself is damped too, finally come to rest [91]. Thus, even without the SHE it would not be feasible to move a Skyrmion along the racetrack by pushing it with a spin wave from the starting edge. Our concept makes use of the damping of spin waves and the Skyrmion Hall angle. The idea is depicted in the left plot of Fig. 4.9. A positively oscillating spin wave $\psi(+\omega)$ travels in the direction of $+y$ and induces a Skyrmion motion in $+y$ direction and also, due to the Skyrmion Hall effect, in $+x$ direction. Meanwhile, a negatively oscillating spin wave $\psi(-\omega)$ travels in the direction of $-y$ and induces Skyrmion motion in both the $-y$ and $+x$ directions (also due to the SHE). In total, the Skyrmion is thus pushed in the $+x$ direction. As depicted in the right plot of Fig. 4.9 the amplitude of each spin wave is smaller the farther away it is from its source. Thus, the opposite spin wave forces in the y direction create a potential holding the Skyrmion in the center lane of the track. The remaining force in x direction moves the Skyrmion along the racetrack. Since this concept of moving the Skyrmion perpendicular to the spin wave direction solely depends on the opposite direction of the SH angle of the opposing waves, it is robust against inaccuracies in the spin wave amplitude and frequency. This concept can, in theory, be applied to a racetrack as depicted in Fig. 4.10. It shows

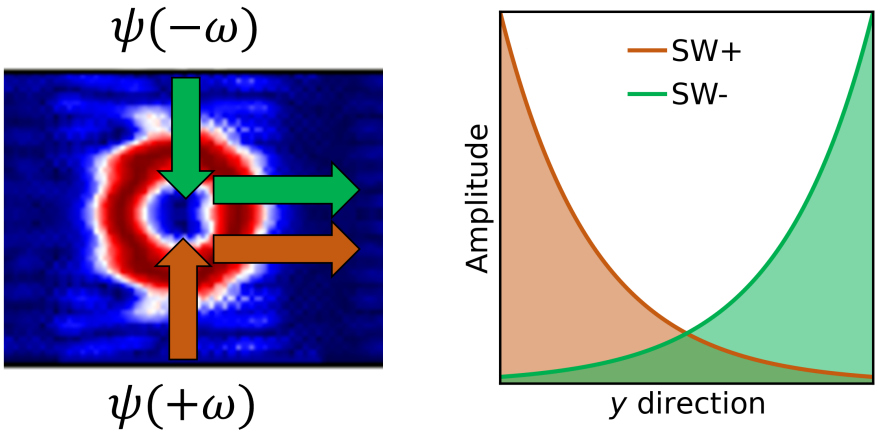

Figure 4.9.: Left: AFM Skyrmion on the racetrack under the influence of the two opposing spin waves. The two differently circularly polarized spin waves, $\psi(+\omega)$ and $\psi(-\omega)$, are injected from the upper and lower edge, respectively. The green and orange arrows indicate the forces acting on the Skyrmion induced by the respective spin wave. Right: Visualization of how the amplitude damping of the two opposing spin waves forms an effective potential in the middle lane of the racetrack. Both pictures are similar to those in Ref. [91].

snapshots from the simulation of our concept of a spin wave driven Skyrmion racetrack. The Skyrmion will be accelerated along the racetrack at each spin wave injection source, denoted by SW, and travels the small spaces between these points on its own due to inertia until it reaches the subsequent region of the driving spin waves. Then it will, again, be accelerated. This process is repeated until the Skyrmion reaches its destination[3]. At least in the simulation this concept makes the transportation of Skyrmions by spin waves along a racetrack possible.

4.6. Spin wave - skyrmion interaction: linearly polarized spin waves

In Sec. 4.2 the existence of linearly polarized spin waves was derived and we were able to simulate those waves as described in Sec. 4.3. These waves have the peculiarity that both sublattice waves precess elliptically with the same amplitude, however in opposite directions. Simulations where linearly polarized spin waves scatter at a single Skyrmion show that they accelerate the Skyrmion in the spin wave propagation direction. In contrast to the circularly polarized spin waves, the linearly polarized spin waves move the Skyrmion exclusively into their propagation direction and, thus, do not induce the Skyrmion Hall effect onto the Skyrmion, see also Refs. [91, 125]. The elliptical oscillation of the spin waves breaks the symmetry between the x and y components since one component oscillates with a significantly larger amplitude. Therefore, we examined the impact from the spin waves on Bloch- and Néel-type Skyrmions separately. The different types of Skyrmions were explained in Sec. 2.4. The crucial information here is that Bloch- and Néel-type Skyrmions

[3] A video can be found in the supplemental material of Ref. [91].

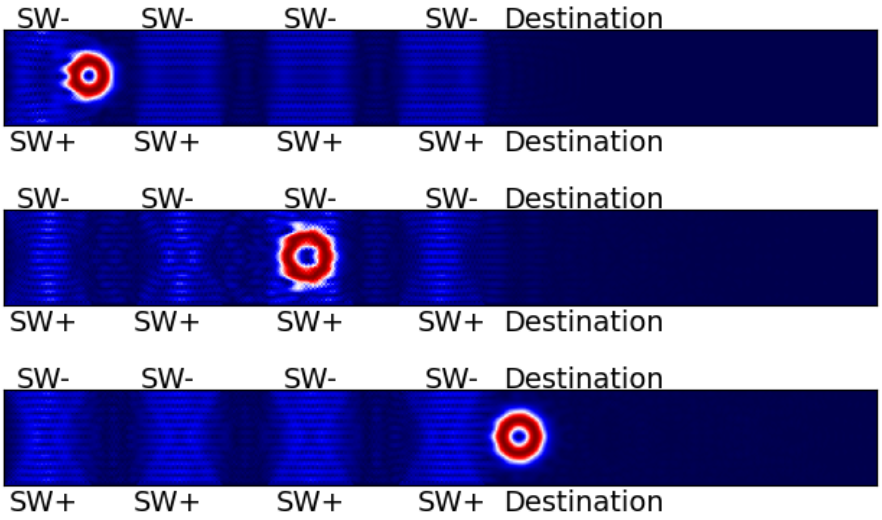

Figure 4.10.: Top to bottom: Position of the Skyrmion in the conceptual racetrack. The opposing spin wave sources for left- and right handed circularly polarized spin waves are denoted as SW+ and SW-. A similar picture, as well as a video, can be found in Ref. [91].

can be converted into one another by transforming the non-z components according to $n_x \to n_y$ and $n_y \to -n_x$. In Fig. 4.11 the acceleration of Bloch- and Néel-type Skyrmions

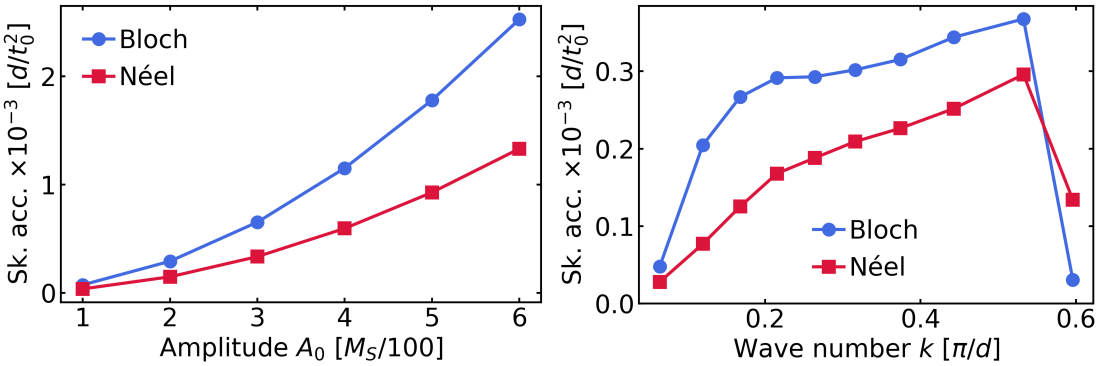

Figure 4.11.: The resulting acceleration of a Bloch type (blue circles) and a Néel type (red squares) Skyrmion, extracted by fitting the simulation data. The acceleration was induced by spin waves of different driving amplitudes A_0 (left) and wave numbers k (right).

induced by the x linearly polarized spin waves is shown. The left plot shows the acceleration based on the amplitude of the driving spin wave while the right plot shows the acceleration based on the wave number of the driving spin wave. The x linearly polarized spin waves acts stronger on the Bloch-type Skyrmion than on the Néel-type Skyrmion. This stands in contrast to circularly polarized spin waves which accelerate Bloch- and Néel-type Skyrmions in the same way. Moreover, simulating the Skyrmion acceleration induced by y linearly polarized spin waves (not shown here), we found the same results as in Fig. 4.11, however with "Bloch" and "Néel" interchanged. This is a consequence of

the x - y component symmetry of these two Skyrmion types and the linearly polarized spin waves. Apart from this, the induced Skyrmion motion shows similar behavior as the Skyrmion motion induced by circularly polarized spin waves. Increasing the amplitude of the driving wave leads to a non-linear increase of the Skyrmion acceleration. Also higher wave numbers up to $k \approx 0.5\pi$ accelerate the Skyrmions faster. Again, at wave numbers larger than $\frac{\pi}{2}$ the acceleration of the Skyrmion rapidly drops. Comparing the absolute values of the Skyrmion acceleration due to linearly polarized spin waves (Fig. 4.11) to those driven by circularly polarized spin waves (Fig. 4.8) it turns out that circularly polarized spin waves drive Skyrmions faster.

4.7. Intuitive insight based on FM behavior

Since we can simulate ferromagnetic and antiferromagnetic systems on the same model (by simply switching $J \to -J$), we were able to simulate both cases, ferromagnetic and antiferromagnetic, under the same conditions. In the simulations on a square lattice we chose all parameters to be identical for ferromagnetic and antiferromagnetic Skyrmions, with the aforementioned exception $J_{\mathrm{AFM}} = -J_{\mathrm{FM}}$. Figure 4.12 shows the traveled distance of a ferromagnetic (left) and an antiferromagnetic (right) Skyrmion, driven by the respective spin wave. The left plot shows the distance in x direction (solid lines) and y direction

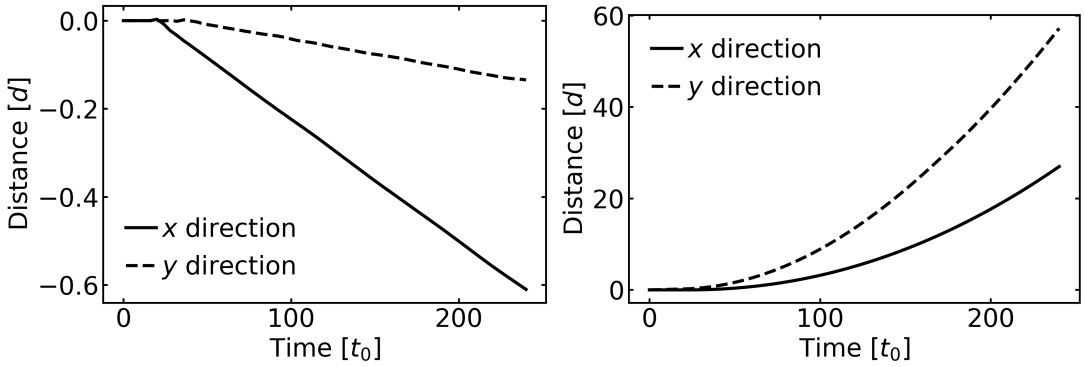

Figure 4.12.: Resulting motion in x and y direction over time of a Skyrmion affected by a spin wave for the ferromagnetic (left) and the antiferromagnetic (right) lattice.

(dashed lines) of the Skyrmion in a ferromagnetic system for an exemplary driving frequency $\omega/J = 2.5$. The right plot shows the same for a Skyrmion in an antiferromagnetic system. In both cases the spin wave was injected as a circularly polarized spin wave (the only ones possible in FM) with an amplitude of $0.05M_S$ in the ferromagnetic case and $0.02M_S$ in the antiferromagnetic case. It is clearly visible that in ferromagnetic systems Skyrmions move completely different when driven by spin waves than in antiferromagnetic ones. The ferromagnetic Skyrmion moves with a constant velocity and against the spin wave propagation direction. This matches the common knowledge of ferromagnetic spin wave - Skyrmion interaction [127]. It also fits into the picture that ferromagnetic

Skyrmions, as massless quasi-particles, move with a constant velocity when an external force is applied [62]. Here, this external force is the continuous stream of spin waves. In contrast, in the antiferromagnetic system the spin wave accelerates the Skyrmion over time in its propagation direction. This behavior reflects the description of the antiferromagnetic Skyrmion as a quasi-particle with finite mass [32, 51]. Comparing the order of magnitude of the traveled distance in both cases we see that the antiferromagnetic Skyrmion traveled a remarkably larger distance than the ferromagnetic one. This is a major point to consider when working with antiferromagnetic Skyrmions. While spin waves would only have a minor effect on FM Skyrmion motion, they heavily impact AFM Skyrmion motion.
The differences between the spin wave induced motion of Skyrmions in ferromagnetic and antiferromagnetic systems are intriguing. The mechanics of the spin waves and Skyrmions are similar in both systems with the exception of a different dispersion relation and the separation into two sublattices. Although the difference in the dispersion relation might play a role, the interaction of the two effectively coupled sublattices is the main reason for the significant difference between the two systems. We assume, as a rough approximation, that on the antiferromagnetic lattice each sublattice spin wave impacts its corresponding sublattice Skyrmion as it is the case for the ferromagnetic lattice. That means we also assume that each sublattice Skyrmion behaves like the FM Skyrmion in Fig. 4.12 (left). A peculiarity of the ferromagnetic lattice is that it only exhibits one spin wave mode. Concretely, for the stationary state $\boldsymbol{n}_0 = +\boldsymbol{z}$ only spin waves with $\omega < 0$ are possible while the stationary state $\boldsymbol{n}_0 = -\boldsymbol{z}$ exhibits solely spin waves where $\omega > 0$. We also found this behavior in the simulations. Furthermore, the spin wave mode determines the direction of the Skyrmion motion. While the $\omega < 0$ mode moves the Skyrmion as in Fig. 4.12 (left), the $\omega > 0$ mode moves the Skyrmion in negative x and positive y direction. The quantity of the resulting velocity is equal in both cases. As expected, spin waves with larger amplitudes also drive the Skyrmion faster. This is shown in Fig. 4.13 (left) where the resulting velocity of FM Skyrmions driven by spin waves with different amplitudes are shown. The Skyrmion velocity non-monotonically depends on the wave number of the

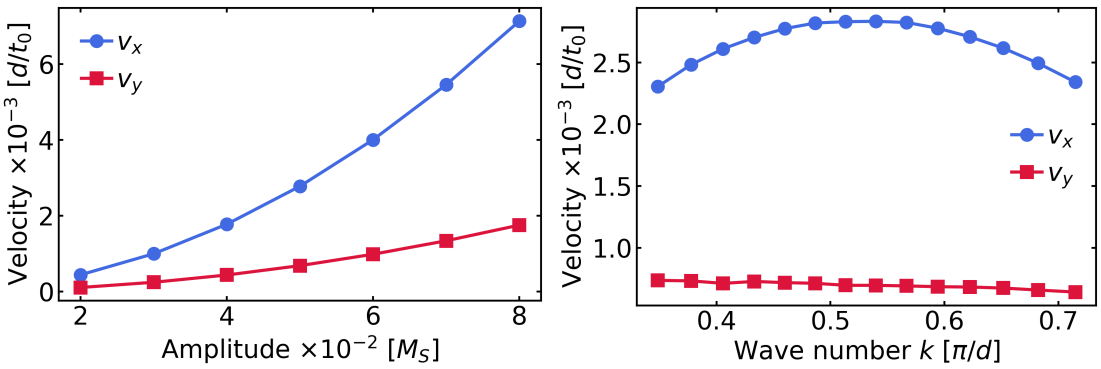

Figure 4.13.: Velocity of the FM Skyrmion motion in x (blue circles) and y (red squares) direction driven by spin waves with different amplitudes (left) and wave numbers (right).

driving spin wave. This is shown in Fig. 4.13 (right). Interestingly, the wave number only impacts the velocity in x direction.
Since the sublattice spin waves in the antiferromagnetic lattice oscillate in the same direction, we assume that both sublattice Skyrmions are driven in the same direction as well. As shown in Fig. 4.3 in Sec. 4.3, the amplitudes of the different sublattice waves in the circularly polarized antiferromagnetic spin wave are different. This has the consequence that the sublattice Skyrmions are driven with different velocities (see Fig. 4.13 left plot). For the sake of clarity, this is sketched in Fig. 4.14. The dotted circle in the middle rep-

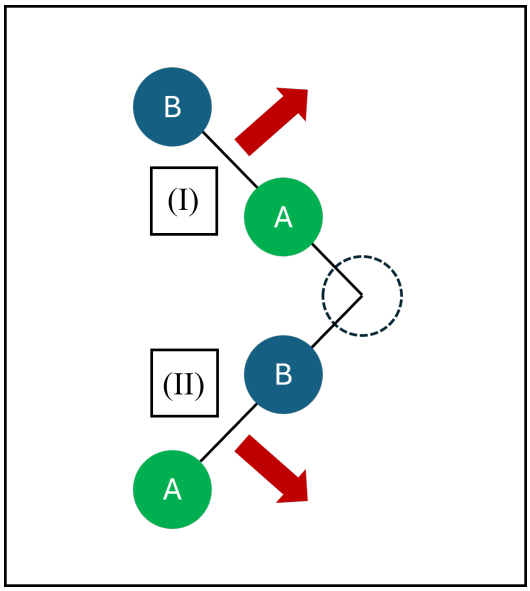

Figure 4.14.: Sketch of the displacement of the two sublattice Skyrmions, A and B, induced by a circularly polarized spin wave. The dotted circle is the initial position of the AFM Skyrmion, while the full circles represents the sublattice Skyrmions A (green) and B (blue). The red arrows indicate the resulting AFM Skyrmion motion direction of each scenario (I) or (II).

resents the initial position of the Skyrmion. The circles in different colors represent the two sublattice Skyrmions and how they are displaced from their initial position (highly exaggerated). The sketch shows two possible scenarios. First, both sublattice Skyrmions are driven into $-x$ and $-y$ direction. For the spin wave mode which causes the Skyrmion to move in this direction, the sublattice wave amplitude of A is larger than of B and, thus, sublattice Skyrmion A is moved faster. The second scenario is that both sublattice Skyrmions are moved into $-x$ and $+y$ direction. Since this motion can only be caused by the other mode, sublattice B now hosts the spin wave with the larger amplitude (see Sec. 4.2). In both scenarios the relative position of both sublattice Skyrmions $\boldsymbol{r}_A - \boldsymbol{r}_B$ increases with a constant velocity $\boldsymbol{v}_{\text{rel}} = \boldsymbol{v}_A - \boldsymbol{v}_B$. It was recently shown [51] that a displacement between the two sublattice Skyrmions moves the whole antiferromagnetic Skyrmion perpendicular to this displacement.
As derived in Chapter 3, a sublattice Skyrmion displacement $\boldsymbol{\delta}$ leads to the Skyrmion velocity $4\pi\boldsymbol{v} = \Lambda\boldsymbol{z} \times \boldsymbol{\delta}$, where Λ is a constant. A constant relative velocity between

the sublattice Skyrmions leads to a linearly increasing displacement over time and, consequently, to a constant acceleration of the whole antiferromagnetic Skyrmion perpendicular to said relative velocity. The red arrows in the sketch in Fig. 4.14 indicate the direction of this acceleration. Regarding the antiferromagnetic Skyrmion driven by circularly polarized spin waves, see Fig. 4.7 (left), this is indeed the expected behavior. Although this explanation neglects the impact of the different dispersion relation between ferromagnetic and antiferromagnetic spin waves, it gives an idea of why the AFM Skyrmion is accelerated into the spin wave propagation direction while the FM Skyrmion moves with a constant velocity against the spin wave direction. It also explains the connection that a sublattice exchange $A \leftrightarrow B$ (or the change of the AFM spin wave mode $\omega \leftrightarrow -\omega$) results in a change of the Skyrmion Hall angle direction. Furthermore, it illustrates how the linearly polarized spin waves can drive the AFM Skyrmion solely into their propagation direction, whereas the ferromagnetic spin wave driven Skyrmions always exhibits a Skyrmion Hall effect. This is due to the fact that both sublattice spin waves oscillate with the same amplitude, however in different directions. Thus, both sublattice Skyrmions are moved with the same velocity. A more extensive study on that explanation is beyond the scope of this thesis. However, combining the theory of spin wave driven ferromagnetic Skyrmions (e.g., Ref. [62]) with the formalism of sublattice displacement, Ref. [51], should provide a good starting point for future research.

4.8. Conclusion

In this chapter, we derived a classical spin wave theory tailored to the discrete two-dimensional square lattice with an easy axis in the z direction. Furthermore, we assumed the spin waves to be small excitations of the classical ground state. We found the dispersion relation for the ferromagnetic and antiferromagnetic lattice and it turned out that both do not depend on the DMI. While the ferromagnetic spin waves exhibit only a single mode, the antiferromagnetic spin waves have two modes symmetric around zero, $\pm\omega$. The two modes are called left-handed or right-handed circularly polarized spin waves. Furthermore, the antiferromagnetic spin waves consist of two ferromagnetic waves in each sublattice which have different amplitudes. The difference of these amplitudes depends on the wave number k and is connected to the mode in such a way that changing the mode interchanges the sublattice amplitudes. We continued by assuming a superposition of spin waves of different modes and, by this, analytically derived linearly polarized spin waves. Those spin waves oscillate with the same amplitude in both sublattices, but with different orientation. Another peculiarity is that these waves oscillate elliptically, i.e., with different amplitudes in the x and y component. Thus, they are called either x- or y- linearly polarized spin waves, depending on which component oscillates with the larger amplitude. In addition, the analytical description of both ferro- and antiferromagnetic spin waves includes non-vanishing damping. This damping results in an exponential decay scaled by

the Gilbert damping and therefore defines a decay time or a decay length, respectively. All analytical results were verified by numerical simulations.
Subsequently, we studied how spin waves affect a Skyrmion on an antiferromagnetic lattice. To this end, we artificially injected a continuous stream of a mono-chromatic spin wave at the left lattice edge and let it scatter at an isolated Skyrmion. The spin wave accelerates the Skyrmion into its propagation direction. While linearly polarized spin waves move the Skyrmion solely into the spin wave propagation direction, circularly polarized spin waves induce an additional motion perpendicular to the spin wave propagation direction. The latter has the consequence that the Skyrmion moves at an angle to the spin wave propagation direction. This effect is, in reference to the current-induced Skyrmion motion, called the Skyrmion Hall effect where the aforementioned angle is the Skyrmion Hall angle. The magnitude of the Skyrmion Hall angle depends on the wave frequency while its direction depends on whether it stems from left- or right handed circularly polarized spin waves. Based on these findings we proposed a racetrack concept for spin wave driven AFM Skyrmions in Sec. 4.5. The concept takes damping into account and is robust against technical uncertainties in the spin wave frequency. While there is currently no real-world application for this concept, it holds the potential for future implementation regarding AFM Skyrmion racetracks.
In contrast to the circularly polarized spin waves, the linearly polarized spin waves do not cause a Skyrmion Hall effect, but they move Néel-type and Bloch-type Skyrmions differently. This is a peculiarity of linearly polarized spin waves and the resulting Skyrmion motion is perfectly symmetric: x linearly polarized spin waves move Néel-type Skyrmions the same way as y linearly polarized spin waves move Bloch-type Skyrmions; and vice versa. It is consistent with the fact that one can transform a Néel-type Skyrmion to a Bloch-type Skyrmion by rotating the coordinates system around the z axis (see Sec. 2.4) and in a similar way one transforms x linearly polarized spin waves to y linearly polarized spin waves. Furthermore, in Sec. 4.7 the previously derived AFM Skyrmion behavior induced by spin waves is compared to simulations of spin wave driven FM Skyrmions which are known to move with a constant velocity against the spin wave propagation direction. This fact was confirmed by our simulations and it was also found that spin wave driven FM Skyrmions move much slower than their AFM relatives and always exhibit a Skyrmion Hall effect. The simulated FM and AFM Skyrmion motions were combined with the knowledge from Chapter 3 to give an idea of the underlying mechanics of spin wave driven AFM Skyrmion based on what is already known about FM spin wave driven Skyrmions.
In a wider context, the details of how spin waves affect antiferromagnetic Skyrmions are useful for real systems. Spin waves appear, among other reasons, due to thermal fluctuations. Since AFM Skyrmion react much stronger to spin waves than FM Skyrmions, the impact of spin waves in temperature induced AFM Skyrmion motion should be more prominent regarding antiferromagnets. For ferromagnetic Skyrmions it is known that

there is a competition between the forces which are induced by temperature gradients. While the force induced by magnon scattering drive the FM Skyrmion into hotter regions (against the magnon propagation direction), the entropy force of the Skyrmion is directed to colder regions [128–130]. Consequently, the ferromagnetic Skyrmion flows in a certain direction depending on which effect dominates. In contrast, such a competition of forces should not exist for AFM Skyrmions since the magnon induced force also drives them into colder regions (into the magnon propagation direction). Furthermore, AFM Skyrmions are expected to be more sensitive to temperature, and indeed, an increased thermal mobility of AFM Skyrmions was observed in Ref. [32].

5. Summary and conclusion

In this thesis, we investigate the dynamics of antiferromagnetic Skyrmions and, especially, the effects of external forces on their motion. We focus on the fundamental mechanism which causes the antiferromagnetic Skyrmion motion, regarding the antiferromagnetic Skyrmion as a composition of two effectively coupled ferromagnetic sublattice Skyrmions. By assuming these sublattice Skyrmions as rigid, we demonstrate that the coupling leads to an effective mass for the antiferromagnetic Skyrmion and that its dynamics can be understood through the relative displacements of the two sublattice components. This displacement induces a Skyrmion velocity that is proportional in magnitude to the length of the displacement and directed perpendicular to it. Therefore, any displacement results in motion of the antiferromagnetic Skyrmion. Employing this we are able to essentially transform the equation of motion of classical spin dynamics, i.e., the Landau-Lifshitz-Gilbert (LLG) equation, into the equations of motion for a classical particle with finite mass and dissipation. This shows that the antiferromagnetic Skyrmion behaves like a classical particle with a finite mass. It answers the question how a configuration of classical spins can exhibit inertial properties.
The energy of a moving antiferromagnetic Skyrmion can be expressed as the sum of the energy of a resting antiferromagnetic Skyrmion and an excitation energy term. The excitation energy is of quadratic order of the displacement length and can, therefore, be viewed as a harmonic potential. By associating the displacement with the velocity, as suggested by our dynamic calculations, we show that the excitation energy of a moving antiferromagnetic Skyrmion resembles the kinetic energy of a classical particle. This observation reinforces the earlier consideration of the antiferromagnetic Skyrmion as a classical particle.
By considering external driving forces, particularly electric currents, we predict the driven motion of an antiferromagnetic Skyrmion while accounting for sublattice Skyrmion displacement. We assumed two independent sublattice currents with identical current density and focused on two specific scenarios. In the first scenario, where both currents flow in the same direction, the antiferromagnetic Skyrmion is effectively driven parallel to the current. In contrast, when the two currents flow in opposite directions, the Skyrmion exhibits a highly sensitive motion perpendicular to the applied currents. Thus, the formalism established in Chapter 3 enables the expression of the time-resolved velocity of antiferromagnetic Skyrmions driven by electric currents across different scenarios.

An additional method for driving antiferromagnetic Skyrmions involves their interaction

with spin waves. To further investigate the Skyrmion - spin wave interaction, we first derived a classical spin wave formalism specifically tailored for the antiferromagnetic two-dimensional square lattice. This formalism resembles the established antiferromagnetic dispersion relation and demonstrates that antiferromagnetic spin waves consist of two ferromagnetic sublattice waves oscillating with different amplitudes. These are known as circularly polarized spin waves. The ratio of the sublattice amplitudes depends on the wave number k. Additionally, the superposition of two circularly polarized spin waves of the same wave number results in the formation of elliptically oscillating waves, referred to as linearly polarized spin waves. These waves oscillate with equal amplitude in both sublattices, however with different amplitudes in their components, x and y. The ratio of these amplitudes also dependents on the wave number. In the presence of non-vanishing damping, the spin waves exhibit exponential decay as they propagate through the lattice. This decay is characterized by a decay length which depends, among other factors, on the spin wave velocity and Gilbert damping.
We demonstrate through numerical simulations how antiferromagnetic Skyrmions interact with spin waves, focusing on the resulting dynamics of the Skyrmions driven by an externally injected spin wave. We observe that a continuous stream of monochromatic spin waves leads to a constant acceleration of the Skyrmion in the direction of spin wave propagation. Given the fact, established earlier in this thesis, that antiferromagnetic Skyrmions behave like classical particles, we conclude that the spin wave exerts a force on the Skyrmion. The Skyrmion acceleration is directly related to the amplitude of the driving spin wave, with higher amplitudes leading to faster acceleration. Regarding spin wave polarization, we found that linearly polarized spin waves move the Skyrmion solely in the same direction as the wave propagation, with the magnitude of acceleration depending on whether they drive Néel- or Bloch-type Skyrmions. In contrast, circularly polarized spin waves affect both Néel- and Bloch-type Skyrmions equally and induce an additional motion perpendicular to the wave propagation direction. Therefore, the induced Skyrmion motion results in an effect akin to the Skyrmion Hall effect observed in current-driven ferromagnetic Skyrmions. Although these effects have different causes, they share a similar appearance and are thus referred to by the same name. Taking this into account, and acknowledging that real systems exhibit damping, we propose a novel realization of an antiferromagnetic Skyrmion racetrack that incorporates the Skyrmion Hall effect induced by spin waves.

Future research

We found that various types of driving antiferromagnetic Skyrmions can be attributed to a small displacement between the sublattice Skyrmions. Although our focus is primarily on antiferromagnetic Skyrmions driven by electric currents (in Ch. 3) and spin waves (in Ch. 4), this approach has the potential to explain a wider range of antiferromagnetic phenomena. For instance, the curvature-induced motion of Skyrmions discussed in Ref.

[131] illustrates that ferromagnetic and antiferromagnetic Skyrmions are driven in different directions by being on a curved surface. The authors demonstrated that the path of the FM Skyrmion is mostly perpendicular to that of the AFM Skyrmion. This is in agreement with the fact that the AFM Skyrmion motion is perpendicular to the displacement of their sublattice constituents. Another area of research that could benefit from the sublattice Skyrmion displacement formalism is ferrimagnetic (FiM) systems, which are also characterized by two distinct sublattices [132, 133]. This property makes them suitable candidates for the application of the formalism derived in this thesis, naturally with necessary adaptations to the new circumstances. Especially as ferrimagnetic systems have gained prominence in recent years [25, 132–135], the work of this thesis could be particularly relevant for future studies. Furthermore, the insights gained from this thesis, especially the dynamics due to sublattice Skyrmion displacement, may lead to exciting discoveries outside the field of magnetism. Although the framework presented here is rooted in classical spin dynamics through the Landau-Lifshitz-Gilbert (LLG) formalism, it could be adapted to similar systems consisting of two coupled continuous vector fields that form skyrmion-like structures and exhibit gyro-coupling. With the recent theoretical predictions [136] and experimental realizations [137] of optical Skyrmions, we eagerly anticipate future discoveries in this vibrant field.

A. Numerical simulation of the spin dynamics

Studies on magnetic Skyrmions usually validate their results by simulations performed with established micromagnetic simulation programs. For instance, the micromagnetic simulation software *mumax* [138] is used frequently, e.g., in Ref. [116]. Another one is the object oriented micromagnetic framework *OOMMF* [139], e.g., in Ref. [26]. The simulations performed in the present work, however, were executed using a simulation program tailored to the requirements of each research topic. The model used in the simulations is a square lattice of classical magnetic moments. This model has the advantage each magnetic moment can be fully described by simply a three dimensional vector with real valued entries. Therefore, we have before, during and after the simulation direct access to each single magnetic moment on the lattice.

Preparation of the simulation – The simulations were done in *C++*. The lattice can be seen as a multidimensional data array with the shape $N_x \times N_y \times 3$ where N_x and N_y are the number of lattice sites in x and y direction, respectively. Because handling lists is more convenient for the program, the data were flatten into a list. That means the whole lattice is represented by a list with $3N_xN_y$ entries containing each a real number. For the bilayer system we created two of those lists, one for each layer. The simulation program was only responsible for the time evolution, the initial lattice already had to be defined. Therefore, we could construct any initial state necessary to verify analytical results. For instance, we were able to create an antiferromagnetic Skyrmion consisting of two artificially displaced sublattice Skyrmions (see Chapter 3) which would never occur naturally.

The time evolution of the lattice is determined by the generalized Landau-Lifshitz-Gilbert equation (LLG), as in Ref. [111],

$$\begin{aligned}\partial_t \boldsymbol{n}_i = \frac{1}{1+\alpha^2}\Big\{ &-\gamma \boldsymbol{n}_i \times \boldsymbol{H}_i^{\text{eff}} - \alpha\gamma \boldsymbol{n}_i \times \left[\boldsymbol{n}_i \times \boldsymbol{H}_i^{\text{eff}}\right] \\ &+ (\alpha-\beta)\boldsymbol{n}_i \times \left[(\boldsymbol{v}_s \cdot \boldsymbol{\nabla})\, \boldsymbol{n}_i\right] + (\alpha\beta+1)\,(\boldsymbol{v}_s \cdot \boldsymbol{\nabla})\, \boldsymbol{n}_i \Big\}.\end{aligned} \tag{A.1}$$

The values of the gyromagnetic ratio γ, the Gilbert damping parameter α, and the nonadiabaticity parameter β are kept fix and were defined at the start of the simulation. The velocity $\boldsymbol{v}_s$ is a measure of the impact of the applied electric current [47, 111]

$$\boldsymbol{v}_s = \frac{pa^3}{2e}\boldsymbol{j}_c. \tag{A.2}$$

The parameters given to the simulation are the velocities v_s^x and v_s^y instead of the current. The term $(\boldsymbol{v}_s \cdot \boldsymbol{\nabla})\boldsymbol{n}_i$ is the short-hand notation for $v_s^x \partial_x \boldsymbol{n}_i + v_s^y \partial_y \boldsymbol{n}_i$. In the simulation the spatial derivatives is approximated by $\partial_x \boldsymbol{n}_i \approx (\boldsymbol{n}_{i+x} - \boldsymbol{n}_{i-x})/2$. The effective field used in the simulations is

$$\begin{aligned} \boldsymbol{H}_i^{\text{eff}} &= J\left(\boldsymbol{n}_{i+\boldsymbol{x}} + \boldsymbol{n}_{i+\boldsymbol{x}} - \boldsymbol{n}_{i+\boldsymbol{y}} + \boldsymbol{n}_{i-\boldsymbol{y}}\right) \\ &\quad + 2D\left[(\boldsymbol{n}_{i+\boldsymbol{x}} - \boldsymbol{n}_{i-\boldsymbol{x}}) \times \boldsymbol{x} + (\boldsymbol{n}_{i+\boldsymbol{y}} - \boldsymbol{n}_{i-\boldsymbol{y}}) \times \boldsymbol{y}\right] + 2Kn_i^z \boldsymbol{z} \ , \end{aligned} \tag{A.3}$$

where the DMI term shown in Eq. (A.3) represents the bulk DMI. The interfacial DMI would be represented by $\boldsymbol{H}_i^{\text{DMI}} = 2D\left[(\boldsymbol{n}_{i+\boldsymbol{x}} - \boldsymbol{n}_{i-\boldsymbol{x}}) \times \boldsymbol{y} - (\boldsymbol{n}_{i+\boldsymbol{y}} - \boldsymbol{n}_{i-\boldsymbol{y}}) \times \boldsymbol{x}\right]$. This is explained in Chapter 2. For simulating bilayer systems we added the term $-J_{\text{inter}}\boldsymbol{n}_i^B$ to the effective field of sublattice A and $-J_{\text{inter}}\boldsymbol{n}_i^A$ to the effective field of sublattice B, respectively [28]. The model parameter J, D, B_0, K and $-J_{\text{inter}}$ are fix and defined before the start of the simulation.

Computing the dynamics – The fact that the time evolution of each spin ($\partial_t \boldsymbol{n}_i$) can be calculated separately is a huge computational advantage because it enabled us to highly parallelize the computation of the LLG. To do so the simulations were done on a GPU using *Cuda* [140], especially the *thurst* library[1] combined with the *boost* library [141]. How to use *boost* with *thrust* vectors to numerically solve differential equations is explained in detail in Ref. [142]. The fundamental procedure is to define a differential equation (e.g. the LLG) that simultaneously applies to each individual lattice site. This function takes the current state of the lattice site at point $n(t)$ and other time dependent data as input and has the time derivative as an output. An integrated solver from the *boost* library can calculate the state at the later time point $n(t + \Delta t)$ from the initial state $n(t)$ regarding to the rules embedded in the previously mentioned function. We choose, for this work, the "Runge-Kutta-4" solver[2] implemented in the boost library [141]. In principle, it calculates small time steps $n(t + \delta t)$ from $n(t)$ and $\partial_t n(t)$ and repeats this until it reaches $n(t + \Delta t)$. Thus, it is called an iterative solver and gives only an approximation of the result. The actual solving process of the Runge-Kutta method is similar to the Euler method, calculating $n(t + \delta t) \approx n(t) + \partial_t n(t) \cdot \delta t$. However, it includes higher orders of the approximation making it more complex and accurate. A more detailed explanation can be found in Ref. [143]. Concretely, in the simulations done in this work, the state we want to evolve in time is the lattice. The function with which the time derivative is calculated is Eq. (A.1). In addition to the lattice and the fix parameters (J, D, K, B_0, J_{inter}, α, β, v_s^x, v_s^y) the time evolution depends, through the effective field and the spatial derivatives, on the nearest neighbors. Due to the parallelization each lattice site is handled individually and the position information is omitted. Technically speaking, the solver takes the current state as a list and handles each entry separately. To consider the neighboring spins, we copied the lattice and shifted on the copied lattice each lattice site one position into $+x$

[1] See `https://nvidia.github.io/cccl/thrust/`

[2] See `https://www.boost.org/doc/libs/1_85_0/libs/numeric/odeint/doc/html/boost_numeric_odeint/odeint_in_detail/steppers.html`

direction. The same was done for the $-x$, $+y$ and $-y$ neighbors, so that there are four additional lattices. In consequence, each additionally considered neighboring lattice site would increase the data stream, and thus costs, by one whole lattice. The edges were treated separately. We realized closed boundary conditions, i.e., the time derivative of the edge spins were set to zero, and we also realized periodic boundary conditions. In the case of edge spin manipulation (see Chapter 4) we used closed boundary conditions and set the values of the left edge spins manually. In summary, the parameter and the current state of the lattice is given into the simulation and the state of the lattice at a later time point $t + \Delta t$, evolved by the rules of LLG, is taken from the simulation.

Data processing – The data taken from the simulations were processed using *python*. The simulation program returns an ordered list of $N_x \times N_y \times 3$ data-arrays where each array represents the current state of the lattice at the time $\boldsymbol{n}(t_i)$. Therefore, we had full knowledge about the magnetic moment of each lattice site at each time point $\boldsymbol{n}_{t,x,y}$. When the behavior of single spin components over time or snap shots of data fields are shown in this work, then these are labeled as such. However, the Skyrmion position or integrals (such as $\mathcal{D}$ from Chapter 3) are also shown. Here we explain the technical details of how those values were extracted from the data. The spatial derivative in either x or y direction of the lattice were done using the *gradient* method from the *numpy* library in python [144]. The integration was done by a sum over all lattice sites divided by the number of the considered sites. The Skyrmion position was calculated as a center of mass regarding the topological charge density following Ref. [111]. To this end, we calculated the topological charge density $q = \boldsymbol{n} \cdot (\partial_x \boldsymbol{n} \times \partial_y \boldsymbol{n})$ and subsequently calculated the cms

$$r_{\mathrm{Sk}} = \frac{\int q(x,y)\ r\ \mathrm{d}x\mathrm{d}y}{\int q(x,y)\ \mathrm{d}x\mathrm{d}y}\ ,\ \text{where } r \in \{x, y\}. \tag{A.4}$$

The Skyrmion radius was calculated, also following Ref. [111], as

$$R = \sqrt{\frac{\int q(x,y)\ [\boldsymbol{r} - \boldsymbol{r}_{Sk}]^2\ \mathrm{d}x\mathrm{d}y}{\int q(x,y)\ \mathrm{d}x\mathrm{d}y}}. \tag{A.5}$$

To extract the ferromagnetic sublattices from the simulation data, we used different methods. The case of the bilayer model is trivial since both sublattices are separate data sets representing ferromagnetic lattices. In the case of the bipartite antiferromagnet (monolayer where neighbors are from different sublattices), we either use the full lattice or separate the sublattices. The former was applied when we studied the antiferromagnetic Skyrmion as a macroscopic object neglecting the inner sublattice structure. To this end, we multiplied the vectors of one of both sublattices by -1. For stationary states of the lattice ($\partial_t \boldsymbol{n} = 0$) this resembles exactly the ferromagnetic counterpart, see Ch. 2 or Ref. [91]. For non-stationary states as moving AFM Skyrmions, this represents the center-of-mass dynamics since both sublattices are weighted equally. The second method was used when explicit sublattice relevant data was crucial, e.g., the relative position between the sublat-

tice Skyrmions. The data of each even row and each even column was compressed to the field of sublattice A and the data of each odd row and each odd column was compressed to sublattice B. In terms of python that means `sublatticeA = data[::2, ::2]` and `sublattice B = data[1::2, 1::2]`. This had the consequence of loss of information since the data of even row and odd column as well as odd row and even column were omitted. Nevertheless, this loss is necessary to keep the square structure of the fields. Both methods were used when appropriate so that the antiferromagnetic Skyrmion could be examined using the tools which already exists for ferromagnetic Skyrmions.

B. Relevant integrals

In the main text various integrals were necessary to consider. In this section, we want to show how they were solved. In all cases a three-dimensional vector field

$$\boldsymbol{n}(\boldsymbol{r}) = \begin{pmatrix} n_x(\boldsymbol{r}) \\ n_y(\boldsymbol{r}) \\ n_z(\boldsymbol{r}) \end{pmatrix} \tag{B.1}$$

was assumed living on a two-dimensional plane $\boldsymbol{r} \in \mathbb{R}^2$. The model is constructed in such a way that the vector field has a constant length of one, $|\boldsymbol{n}|^2 = 1$. Therefore, we can view it as a position of the unit sphere and transform the vector field to spherical coordinates

$$\boldsymbol{n}(\boldsymbol{r}) = \begin{pmatrix} \sin\Theta(\boldsymbol{r}) \ \cos\Phi(\boldsymbol{r}) \\ \sin\Theta(\boldsymbol{r}) \ \sin\Phi(\boldsymbol{r}) \\ \cos\Theta(\boldsymbol{r}) \end{pmatrix}. \tag{B.2}$$

It is convenient to transform the spatial coordinates (x, y) into polar coordinates $(\rho\cos\varphi, \rho\sin\varphi)$ when working with Skyrmions. Hereby the origin of the coordinate system $\rho = 0$ is exactly the Skyrmion center. If not stated otherwise, we assume Skyrmions of a typical rotation-invariant form. Then their components can be separated into [67]

$$\Theta(\rho, \varphi) = \Theta(\rho), \tag{B.3}$$

$$\Phi(\rho, \varphi) = m\varphi + \varphi_0. \tag{B.4}$$

It takes into account, that the angle Θ of the Skyrmion vector field, while not explicitly known, only depends on the radial coordinate while the angle Φ can explicitly be expressed with the angle coordinate φ. The parameters $m = \pm 1$ and φ_0 represent the Skyrmion vorticity and the kind of Skyrmion (Bloch or Néel). Here, only Skyrmions with a positive vorticity $m = 1$ are relevant. Thus, the vector field of the Skyrmion can be written as

$$\boldsymbol{n}_{\mathrm{Sk}}(\boldsymbol{r}) = \begin{pmatrix} \sin\Theta(\rho) \ \cos(\varphi + \varphi_0) \\ \sin\Theta(\rho) \ \sin(\varphi + \varphi_0) \\ \cos\Theta(\rho) \end{pmatrix}. \tag{B.5}$$

Although we do not know the form of $\Theta(\rho)$, it is independent of φ and can thus solve the integral $\int f(\rho, \phi)\mathrm{d}\varphi$. We also assume that the integral over ρ yields a finite result, so that if the integration over φ vanishes, the whole integral should vanish. In order to minimize

calculation errors, the integrals were done with the help of *Mathematica*. The original notebooks can be find below. Over the whole notebook we assume the vector field $\boldsymbol{n}$ to form a Skyrmion as in Eq. (B.5) and an effective field

$$\boldsymbol{H}_{\text{eff}} = -\frac{\lambda}{2}\boldsymbol{n} + A(\partial_x^2\boldsymbol{n} + \partial_y^2\boldsymbol{n}) + \boldsymbol{H}_{\text{DMI}} + Kn_z\boldsymbol{z}. \tag{B.6}$$

As explained in the main text, one typically distinguish between bulk- and interfacial DMI. While the former stabilizes Bloch Skyrmions, represented by $\varphi_0 = \pi/2$, the latter stabilizes Néel Skyrmions which are represented by $\varphi_0 = 0$. The corresponding terms in the effective field are

$$\boldsymbol{H}_{\text{DMI}}^{\text{bulk}} = -D\ (\partial_y n_z, -\partial_x n_z, \partial_x n_y - \partial_y n_x)^T, \tag{B.7}$$

$$\boldsymbol{H}_{\text{DMI}}^{\text{if}} = -D\ (\partial_x n_z, \partial_y n_z, -\partial_x n_x - d\partial_y n_y)^T. \tag{B.8}$$

The resulting integral solutions are shown in the following. We note that, the indices i, j and k denote that this equation holds for all $i, j, k \in \{x, y\}$ and are independent whether we considered a Bloch-type Skyrmion using bulk DMI or a Néel-type Skyrmion using interfacial DMI.

$$\int_0^{2\pi} r\ (\partial_i\boldsymbol{n}) \cdot \frac{\lambda}{2}\boldsymbol{n}\ \mathrm{d}\varphi = 0 \tag{B.9}$$

$$\int_0^{2\pi} r\ (\partial_i\boldsymbol{n}) \cdot A(\partial_x^2\boldsymbol{n} + \partial_y^2\boldsymbol{n})\ \mathrm{d}\varphi = 0 \tag{B.10}$$

$$\int_0^{2\pi} r\ (\partial_i\boldsymbol{n}) \cdot \boldsymbol{H}_{\text{DMI}}\ \mathrm{d}\varphi = 0 \tag{B.11}$$

$$\int_0^{2\pi} r\ (\partial_i\boldsymbol{n}) \cdot Kn_z\boldsymbol{z}\ \mathrm{d}\varphi = 0 \tag{B.12}$$

$$\int_0^{2\pi} r\ (\partial_i\partial_j\partial_k\boldsymbol{n}) \cdot \boldsymbol{H}_{\text{eff}}\ \mathrm{d}\varphi = 0 \tag{B.13}$$

$$\int_0^{2\pi} r\ (\partial_i\partial_j\boldsymbol{n}) \cdot \boldsymbol{H}_{\text{eff}}\ \mathrm{d}\varphi = \delta_{ij}\Lambda \tag{B.14}$$

$$\int_0^{2\pi} r\ (\partial_i\boldsymbol{n}) \cdot (\partial_j\boldsymbol{n})\ \mathrm{d}\varphi = \delta_{ij}\mathcal{D}. \tag{B.15}$$

We start by defining the polar coordinates as functions of the Cartesian coordinates

In[1]:=
```
ρ[x_, y_] := Sqrt[x^2 + y^2];
φ[x_, y_] := ArcTan[x, y];
```

Next, we define the three components of the vector field and store them in a three-dimensional vector. It is important to put the coordinate transform as a condition behind.

In[3]:=
```
n1 = Sin[θ[ρ[x, y]]] * Cos[φ[x, y] + φ0];
n2 = Sin[θ[ρ[x, y]]] * Sin[φ[x, y] + φ0];
n3 = Cos[θ[ρ[x, y]]];
n = {n1, n2, n3} /. {x^2 + y^2 → ρ^2, ArcTan[x, y] → φ, x → ρ Cos[φ], y → ρ Sin[φ]};
```

The integrals will contain spatial derivatives of the vector field in x and y direction. Therefore, we define those derivatives as vector fields. The notation is that:

dxn = ∂n/∂x**.**

It is convenient that Mathematica can handle the coordinate transform automatically.

In[7]:=
```
dxn1 = ∂x n1 /. {x^2 + y^2 → ρ^2, ArcTan[x, y] → φ, x → ρ Cos[φ], y → ρ Sin[φ]};
dxn2 = ∂x n2 /. {x^2 + y^2 → ρ^2, ArcTan[x, y] → φ, x → ρ Cos[φ], y → ρ Sin[φ]};
dxn3 = ∂x n3 /. {x^2 + y^2 → ρ^2, ArcTan[x, y] → φ, x → ρ Cos[φ], y → ρ Sin[φ]};
dxn = {dxn1, dxn2, dxn3};
dyn1 = ∂y n1 /. {x^2 + y^2 → ρ^2, ArcTan[x, y] → φ, x → ρ Cos[φ], y → ρ Sin[φ]};
dyn2 = ∂y n2 /. {x^2 + y^2 → ρ^2, ArcTan[x, y] → φ, x → ρ Cos[φ], y → ρ Sin[φ]};
dyn3 = ∂y n3 /. {x^2 + y^2 → ρ^2, ArcTan[x, y] → φ, x → ρ Cos[φ], y → ρ Sin[φ]};
dyn = {dyn1, dyn2, dyn3};
```

The same is done with derivatives of higher order. The notation here is, e.g. , **dxdyn** = $\frac{\partial^2 n}{\partial x \partial y}$ **.**

In[15]:=
```
dxdxn1 = ∂x,x n1 /. {x^2 + y^2 → ρ^2, ArcTan[x, y] → φ, x → ρ Cos[φ], y → ρ Sin[φ]};
dxdxn2 = ∂x,x n2 /. {x^2 + y^2 → ρ^2, ArcTan[x, y] → φ, x → ρ Cos[φ], y → ρ Sin[φ]};
dxdxn3 = ∂x,x n3 /. {x^2 + y^2 → ρ^2, ArcTan[x, y] → φ, x → ρ Cos[φ], y → ρ Sin[φ]};
dxdxn = {dxdxn1, dxdxn2, dxdxn3};

dydyn1 = ∂y,y n1 /. {x^2 + y^2 → ρ^2, ArcTan[x, y] → φ, x → ρ Cos[φ], y → ρ Sin[φ]};
dydyn2 = ∂y,y n2 /. {x^2 + y^2 → ρ^2, ArcTan[x, y] → φ, x → ρ Cos[φ], y → ρ Sin[φ]};
dydyn3 = ∂y,y n3 /. {x^2 + y^2 → ρ^2, ArcTan[x, y] → φ, x → ρ Cos[φ], y → ρ Sin[φ]};
dydyn = {dydyn1, dydyn2, dydyn3};

dxdyn1 = ∂x,y n1 /. {x^2 + y^2 → ρ^2, ArcTan[x, y] → φ, x → ρ Cos[φ], y → ρ Sin[φ]};
dxdyn2 = ∂x,y n2 /. {x^2 + y^2 → ρ^2, ArcTan[x, y] → φ, x → ρ Cos[φ], y → ρ Sin[φ]};
dxdyn3 = ∂x,y n3 /. {x^2 + y^2 → ρ^2, ArcTan[x, y] → φ, x → ρ Cos[φ], y → ρ Sin[φ]};
dxdyn = {dxdyn1, dxdyn2, dxdyn3};

dxdxdxn1 = ∂x,x,x n1 /. {x^2 + y^2 → ρ^2, ArcTan[x, y] → φ, x → ρ Cos[φ], y → ρ Sin[φ]};
dxdxdxn2 = ∂x,x,x n2 /. {x^2 + y^2 → ρ^2, ArcTan[x, y] → φ, x → ρ Cos[φ], y → ρ Sin[φ]};
dxdxdxn3 = ∂x,x,x n3 /. {x^2 + y^2 → ρ^2, ArcTan[x, y] → φ, x → ρ Cos[φ], y → ρ Sin[φ]};
dxdxdxn = {dxdxdxn1, dxdxdxn2, dxdxdxn3};

dxdxdyn1 = ∂x,x,y n1 /. {x^2 + y^2 → ρ^2, ArcTan[x, y] → φ, x → ρ Cos[φ], y → ρ Sin[φ]};
dxdxdyn2 = ∂x,x,y n2 /. {x^2 + y^2 → ρ^2, ArcTan[x, y] → φ, x → ρ Cos[φ], y → ρ Sin[φ]};
dxdxdyn3 = ∂x,x,y n3 /. {x^2 + y^2 → ρ^2, ArcTan[x, y] → φ, x → ρ Cos[φ], y → ρ Sin[φ]};
dxdxdyn = {dxdxdyn1, dxdxdyn2, dxdxdyn3};

dxdydyn1 = ∂x,y,y n1 /. {x^2 + y^2 → ρ^2, ArcTan[x, y] → φ, x → ρ Cos[φ], y → ρ Sin[φ]};
dxdydyn2 = ∂x,y,y n2 /. {x^2 + y^2 → ρ^2, ArcTan[x, y] → φ, x → ρ Cos[φ], y → ρ Sin[φ]};
dxdydyn3 = ∂x,y,y n3 /. {x^2 + y^2 → ρ^2, ArcTan[x, y] → φ, x → ρ Cos[φ], y → ρ Sin[φ]};
dxdydyn = {dxdydyn1, dxdydyn2, dxdydyn3};

dydydyn1 = ∂y,y,y n1 /. {x^2 + y^2 → ρ^2, ArcTan[x, y] → φ, x → ρ Cos[φ], y → ρ Sin[φ]};
dydydyn2 = ∂y,y,y n2 /. {x^2 + y^2 → ρ^2, ArcTan[x, y] → φ, x → ρ Cos[φ], y → ρ Sin[φ]};
dydydyn3 = ∂y,y,y n3 /. {x^2 + y^2 → ρ^2, ArcTan[x, y] → φ, x → ρ Cos[φ], y → ρ Sin[φ]};
dydydyn = {dydydyn1, dydydyn2, dydydyn3};
```

Now all derivatives up to third order are defined. In the next step we define the four parts of the effective field. Since our formalism traces the problem back to a ferromagnetic Skyrmion, the intra-sublattice and inter-sublattice terms of the effective field looks identical except of the parameter. Therefore, using these four parts of the effective field is sufficient for both intra- and inter-sublattice calculations.

In[43]:=
```
Heff1 = -λ / 2 * n /. {x^2 + y^2 → ρ^2, ArcTan[x, y] → φ, x → ρ Cos[φ], y → ρ Sin[φ]};
Heff2 =
  A * (dxdxn + dydyn) /. {x^2 + y^2 → ρ^2, ArcTan[x, y] → φ, x → ρ Cos[φ], y → ρ Sin[φ]};
Heff3b = -D * {dyn3, -dxn3, dxn2 - dyn1} /.
    {x^2 + y^2 → ρ^2, ArcTan[x, y] → φ, x → ρ Cos[φ], y → ρ Sin[φ]};
Heff3i = D * {dxn3, dyn3, -dxn1 - dyn2} /.
    {x^2 + y^2 → ρ^2, ArcTan[x, y] → φ, x → ρ Cos[φ], y → ρ Sin[φ]};
Heff4 =
  K * n3 * {0, 0, 1} /. {x^2 + y^2 → ρ^2, ArcTan[x, y] → φ, x → ρ Cos[φ], y → ρ Sin[φ]};
Heffb = Heff1 + Heff2 + Heff3b + Heff4 /.
    {x^2 + y^2 → ρ^2, ArcTan[x, y] → φ, x → ρ Cos[φ], y → ρ Sin[φ]};
Heffi = Heff1 + Heff2 + Heff3i + Heff4 /.
    {x^2 + y^2 → ρ^2, ArcTan[x, y] → φ, x → ρ Cos[φ], y → ρ Sin[φ]};
```

The following will be done for two different cases. At first, we assume a system with Bulk DMI hosting a Bloch type Skyrmion, i.e. $\varphi 0 = \pi/2$.

We show that all integrals containing the scalar product of the effective field parts and derivatives of order 1 and 3 of the vector field vanish

In[50]:=
```
{FullSimplify[
   Integrate[ρ * Heff1.dxn /. {φ0 → Pi / 2}, {φ, 0, 2 * Pi}], Assumptions → ρ ≥ 0],
 FullSimplify[
   Integrate[ρ * Heff2.dxn /. {φ0 → Pi / 2}, {φ, 0, 2 * Pi}], Assumptions → ρ ≥ 0],
 FullSimplify[
   Integrate[ρ * Heff3b.dxn /. {φ0 → Pi / 2}, {φ, 0, 2 * Pi}], Assumptions → ρ ≥ 0],
 FullSimplify[
   Integrate[ρ * Heff4.dxn /. {φ0 → Pi / 2}, {φ, 0, 2 * Pi}], Assumptions → ρ ≥ 0]}
```

Out[50]=
```
{0, 0, 0, 0}
```

In[51]:=
```
{FullSimplify[
   Integrate[ρ * Heff1.dyn /. {φ0 → Pi / 2}, {φ, 0, 2 * Pi}], Assumptions → ρ ≥ 0],
 FullSimplify[
   Integrate[ρ * Heff2.dyn /. {φ0 → Pi / 2}, {φ, 0, 2 * Pi}], Assumptions → ρ ≥ 0],
 FullSimplify[
   Integrate[ρ * Heff3b.dyn /. {φ0 → Pi / 2}, {φ, 0, 2 * Pi}], Assumptions → ρ ≥ 0],
 FullSimplify[
   Integrate[ρ * Heff4.dyn /. {φ0 → Pi / 2}, {φ, 0, 2 * Pi}], Assumptions → ρ ≥ 0]}
```

Out[51]=
```
{0, 0, 0, 0}
```

In[52]:=
```
{FullSimplify[
   Integrate[ρ * Heffb.dxdxdxn /. {φ0 → Pi / 2}, {φ, 0, 2 * Pi}], Assumptions → ρ ≥ 0],
 FullSimplify[
   Integrate[ρ * Heffb.dxdxdyn /. {φ0 → Pi / 2}, {φ, 0, 2 * Pi}], Assumptions → ρ ≥ 0],
 FullSimplify[
   Integrate[ρ * Heffb.dxdydyn /. {φ0 → Pi / 2}, {φ, 0, 2 * Pi}], Assumptions → ρ ≥ 0],
 FullSimplify[
   Integrate[ρ * Heffb.dydydyn /. {φ0 → Pi / 2}, {φ, 0, 2 * Pi}], Assumptions → ρ ≥ 0]}
```

Out[52]=
```
{0, 0, 0, 0}
```

Finally, we will calculate what is called the dissipation tensor D and the force constant Λ in the main text.

In[53]:=
```
FullSimplify[
 Integrate[ρ * Heffb.dxdyn /. {φ0 → Pi / 2}, {φ, 0, 2 * Pi}], Assumptions → ρ ≥ 0]
```

Out[53]=
$$0$$

In[54]:=
```
FullSimplify[
 Integrate[ρ * Heffb.dxdxn /. {φ0 → Pi / 2}, {φ, 0, 2 * Pi}], Assumptions → ρ ≥ 0]
FullSimplify[
 Integrate[ρ * Heffb.dydyn /. {φ0 → Pi / 2}, {φ, 0, 2 * Pi}], Assumptions → ρ ≥ 0]
```

Out[54]=
$$\frac{1}{2\,\rho^3}\pi\,\Big(\big(2\,A+\lambda\,\rho^2\big)\,\text{Sin}[\theta[\rho]]^2+\rho\,\Big(\theta'[\rho]\,\Big(4\,D\,\rho\,\text{Sin}[\theta[\rho]]^2-\big(2\,A+K\,\rho^2\big)\,\text{Sin}[2\,\theta[\rho]]+\rho\,\theta'[\rho]\,\Big(4\,A+(-K+\lambda)\,\rho^2-\big(2\,A+K\,\rho^2\big)\,\text{Cos}[2\,\theta[\rho]]+D\,\rho\,\text{Sin}[2\,\theta[\rho]]+2\,\rho^2\,\theta'[\rho]\,(D+A\,\theta'[\rho])\Big)\Big)+2\,\rho\,\Big(\text{Sin}[\theta[\rho]]\,\Big(-\big(\big(2\,A+K\,\rho^2\big)\,\text{Cos}[\theta[\rho]]\big)+D\,\rho\,\text{Sin}[\theta[\rho]]\Big)+2\,A\,\rho\,\theta'[\rho]\Big)\,\theta''[\rho]+2\,A\,\rho^3\,\theta''[\rho]^2\Big)\Big)$$

Out[55]=
$$\frac{1}{2\,\rho^3}\pi\,\Big(\big(2\,A+\lambda\,\rho^2\big)\,\text{Sin}[\theta[\rho]]^2+\rho\,\Big(\theta'[\rho]\,\Big(4\,D\,\rho\,\text{Sin}[\theta[\rho]]^2-\big(2\,A+K\,\rho^2\big)\,\text{Sin}[2\,\theta[\rho]]+\rho\,\theta'[\rho]\,\Big(4\,A+(-K+\lambda)\,\rho^2-\big(2\,A+K\,\rho^2\big)\,\text{Cos}[2\,\theta[\rho]]+D\,\rho\,\text{Sin}[2\,\theta[\rho]]+2\,\rho^2\,\theta'[\rho]\,(D+A\,\theta'[\rho])\Big)\Big)+2\,\rho\,\Big(\text{Sin}[\theta[\rho]]\,\Big(-\big(\big(2\,A+K\,\rho^2\big)\,\text{Cos}[\theta[\rho]]\big)+D\,\rho\,\text{Sin}[\theta[\rho]]\Big)+2\,A\,\rho\,\theta'[\rho]\Big)\,\theta''[\rho]+2\,A\,\rho^3\,\theta''[\rho]^2\Big)\Big)$$

In[56]:=
```
FullSimplify[Integrate[ρ * dxn.dyn /. {φ0 → Pi / 2}, {φ, 0, 2 * Pi}], Assumptions → ρ ≥ 0]
FullSimplify[Integrate[ρ * dxn.dxn /. {φ0 → Pi / 2}, {φ, 0, 2 * Pi}], Assumptions → ρ ≥ 0]
FullSimplify[Integrate[ρ * dyn.dyn /. {φ0 → Pi / 2}, {φ, 0, 2 * Pi}], Assumptions → ρ ≥ 0]
```

Out[56]=
$$0$$

Out[57]=
$$\frac{\pi\,\text{Sin}[\theta[\rho]]^2}{\rho}+\pi\,\rho\,\theta'[\rho]^2$$

Out[58]=
$$\frac{\pi\,\text{Sin}[\theta[\rho]]^2}{\rho}+\pi\,\rho\,\theta'[\rho]^2$$

The integrals above were done for Bloch type Skyrmions together with a bulk DMI. Since we claim that the integrals are the same for Néel type Skyrmion we repeat the integrals considering Néel type Skyrmions, $\varphi 0 = 0,$ and interfacial DMI.

We show that all integrals containing the scalar product of the effective field parts and derivatives of order 1 and 3 of the vector field vanish

In[59]:=
```
{FullSimplify[Integrate[ρ * Heff1.dxn /. {φ0 → 0}, {φ, 0, 2 * Pi}], Assumptions → ρ ≥ 0],
 FullSimplify[Integrate[ρ * Heff2.dxn /. {φ0 → 0}, {φ, 0, 2 * Pi}], Assumptions → ρ ≥ 0],
 FullSimplify[Integrate[ρ * Heff3i.dxn /. {φ0 → 0}, {φ, 0, 2 * Pi}], Assumptions → ρ ≥ 0],
 FullSimplify[Integrate[ρ * Heff4.dxn /. {φ0 → 0}, {φ, 0, 2 * Pi}], Assumptions → ρ ≥ 0]}
```

Out[59]=
```
{0, 0, 0, 0}
```

In[60]:=
```
{FullSimplify[Integrate[ρ * Heff1.dyn /. {φ0 → 0}, {φ, 0, 2 * Pi}], Assumptions → ρ ≥ 0],
 FullSimplify[Integrate[ρ * Heff2.dyn /. {φ0 → 0}, {φ, 0, 2 * Pi}], Assumptions → ρ ≥ 0],
 FullSimplify[Integrate[ρ * Heff3i.dyn /. {φ0 → 0}, {φ, 0, 2 * Pi}], Assumptions → ρ ≥ 0],
 FullSimplify[Integrate[ρ * Heff4.dyn /. {φ0 → 0}, {φ, 0, 2 * Pi}], Assumptions → ρ ≥ 0]}
```

Out[60]=
```
{0, 0, 0, 0}
```

In[61]:=
```
{FullSimplify[
   Integrate[ρ * Heffi.dxdxdxn /. {φ0 → 0}, {φ, 0, 2 * Pi}], Assumptions → ρ ≥ 0],
 FullSimplify[
   Integrate[ρ * Heffi.dxdxdyn /. {φ0 → 0}, {φ, 0, 2 * Pi}], Assumptions → ρ ≥ 0],
 FullSimplify[
   Integrate[ρ * Heffi.dxdydyn /. {φ0 → 0}, {φ, 0, 2 * Pi}], Assumptions → ρ ≥ 0],
 FullSimplify[
   Integrate[ρ * Heffi.dydydyn /. {φ0 → 0}, {φ, 0, 2 * Pi}], Assumptions → ρ ≥ 0]}
```

Out[61]=
```
{0, 0, 0, 0}
```

Finally, we will calculate what is called the dissipation tensor D and the force constant Λ in the main text.

In[62]:=
```
FullSimplify[Integrate[ρ * Heffi.dxdyn /. {φ0 → 0}, {φ, 0, 2 * Pi}], Assumptions → ρ ≥ 0]
```

Out[62]=
```
0
```

In[63]:=
```
FullSimplify[Integrate[ρ * Heffi.dxdxn /. {φ0 → 0}, {φ, 0, 2 * Pi}], Assumptions → ρ ≥ 0]
FullSimplify[Integrate[ρ * Heffi.dydyn /. {φ0 → 0}, {φ, 0, 2 * Pi}], Assumptions → ρ ≥ 0]
```

Out[63]=
$$\frac{1}{2\,\rho^3}\pi\,\Big(\big(2\,A+\lambda\,\rho^2\big)\,\text{Sin}[\theta[\rho]]^2+\rho\,\Big(\theta'[\rho]\,\Big(4\,D\,\rho\,\text{Sin}[\theta[\rho]]^2-\big(2\,A+K\,\rho^2\big)\,\text{Sin}[2\,\theta[\rho]]+\rho\,\theta'[\rho]\,\Big(4\,A+(-K+\lambda)\,\rho^2-\big(2\,A+K\,\rho^2\big)\,\text{Cos}[2\,\theta[\rho]]+D\,\rho\,\text{Sin}[2\,\theta[\rho]]+2\,\rho^2\,\theta'[\rho]\,(D+A\,\theta'[\rho])\Big)\Big)+2\,\rho\,\Big(\text{Sin}[\theta[\rho]]\,\Big(-\big(\big(2\,A+K\,\rho^2\big)\,\text{Cos}[\theta[\rho]]\big)+D\,\rho\,\text{Sin}[\theta[\rho]]\Big)+2\,A\,\rho\,\theta'[\rho]\Big)\,\theta''[\rho]+2\,A\,\rho^3\,\theta''[\rho]^2\Big)\Big)$$

Out[64]=
$$\frac{1}{2\,\rho^3}\pi\,\Big(\big(2\,A+\lambda\,\rho^2\big)\,\text{Sin}[\theta[\rho]]^2+\rho\,\Big(\theta'[\rho]\,\Big(4\,D\,\rho\,\text{Sin}[\theta[\rho]]^2-\big(2\,A+K\,\rho^2\big)\,\text{Sin}[2\,\theta[\rho]]+\rho\,\theta'[\rho]\,\Big(4\,A+(-K+\lambda)\,\rho^2-\big(2\,A+K\,\rho^2\big)\,\text{Cos}[2\,\theta[\rho]]+D\,\rho\,\text{Sin}[2\,\theta[\rho]]+2\,\rho^2\,\theta'[\rho]\,(D+A\,\theta'[\rho])\Big)\Big)+2\,\rho\,\Big(\text{Sin}[\theta[\rho]]\,\Big(-\big(\big(2\,A+K\,\rho^2\big)\,\text{Cos}[\theta[\rho]]\big)+D\,\rho\,\text{Sin}[\theta[\rho]]\Big)+2\,A\,\rho\,\theta'[\rho]\Big)\,\theta''[\rho]+2\,A\,\rho^3\,\theta''[\rho]^2\Big)\Big)$$

In[65]:=
```
FullSimplify[Integrate[ρ * dxn.dyn /. {φ0 → 0}, {φ, 0, 2 * Pi}], Assumptions → ρ ≥ 0]
FullSimplify[Integrate[ρ * dxn.dxn /. {φ0 → 0}, {φ, 0, 2 * Pi}], Assumptions → ρ ≥ 0]
FullSimplify[Integrate[ρ * dyn.dyn /. {φ0 → 0}, {φ, 0, 2 * Pi}], Assumptions → ρ ≥ 0]
```

Out[65]=
$$0$$

Out[66]=
$$\frac{\pi \, \text{Sin}[\Theta[\rho]]^2}{\rho} + \pi \rho \, \Theta'[\rho]^2$$

Out[67]=
$$\frac{\pi \, \text{Sin}[\Theta[\rho]]^2}{\rho} + \pi \rho \, \Theta'[\rho]^2$$

As a last check we want to see if the parameter Λ is the same for both Skyrmion types

In[68]:=
```
Simplify[Integrate[ρ * Heffi.dxdxn /. {φ0 → 0}, {φ, 0, 2 * Pi}] -
  Integrate[ρ * Heffb.dxdxn /. {φ0 → Pi / 2}, {φ, 0, 2 * Pi}], Assumptions → ρ ≥ 0]
```

Out[68]=
$$0$$

C. Commutator relations

In the main text in Sec. 2.2 we showed that the Landau-Lifshitz equation of motion can also be derived via the Ehrenfest theorem while using the mean field Ansatz. To this end, the commutator relations of quantum mechanical spin operators are needed. While the results were presented in the main text, we will here show the explicit calculations of the commutators.
The first commutator in question is $\left[\sum_{i,r} \boldsymbol{S}_i \cdot \boldsymbol{S}_{i+r}, \boldsymbol{S}_k\right]$. It is more convenient to calculate it using component representation and separating it into pair-wise commutators

$$\left[\sum_{i,r}\sum_{a=x,y,z} S_i^a S_{i+r}^a, \sum_{b=x,y,z} S_k^b \boldsymbol{e}_b\right] = \sum_{i,r,a,b}\left(S_i^a [S_{i+r}^a, S_k^b] - [S_k^b, S_i^a] S_{i+r}^a\right)\boldsymbol{e}_b. \tag{C.1}$$

For these, we can use the general spin operator commutation relation

$$\left[S_j^a, S_k^b\right] = i\hbar\delta_{jk}\sum_c \epsilon_{abc} S_j^c, \tag{C.2}$$

so that the equation above can be written as

$$\left[\sum_{i,r}\sum_a S_i^a S_{i+r}^a, \sum_b S_k^b \boldsymbol{e}_b\right] = i\hbar \sum_{i,r,a,b,c}\left(S_i^a \delta_{i+r,k}\epsilon_{abc} S_k^c - \delta_{ik}\epsilon_{bac} S_i^c S_{i+r}^a\right)\boldsymbol{e}_b. \tag{C.3}$$

We will treat the terms independently, starting with the term left from the minus sign. Considering that the sum over i goes over each single lattice site, we can shift the summation index $i \to i - r$ without altering the total sum. The term then reads

$$\sum_{i,r,a,b} S_{i-r}^a \delta_{i,k}\epsilon_{abc} S_k^c = \sum_{r,a,b,c} S_{k-r}^a \epsilon_{abc} S_k^c. \tag{C.4}$$

Additionally, we assume a symmetric lattice, so that for each neighbor at $-r$ there is also a neighbor at $+r$. Since the sum goes over all r, we can re-write the summation as

$$\sum_{r,a,b,c} S_{k-r}^a \epsilon_{abc} S_k^c = \sum_{r,a,b,c} S_{k+r}^a \epsilon_{abc} S_k^c. \tag{C.5}$$

The second term does not need particular attention, except the (anti-) symmetry of $\epsilon_{bac} = -\epsilon_{abc}$, since the sum over i is absorbed by the Kronecker δ. Therefore, the commutator

from Eq. (C.1) can be written as

$$\left[\sum_{i,r}\sum_{a} S_i^a S_{i+r}^a, \sum_b S_k^b \boldsymbol{e}_b\right] = i\hbar \sum_{r,a,b,c} \epsilon_{abc} \left(S_{k+r}^a S_k^c + S_k^c S_{k+r}^a\right) \boldsymbol{e}_b. \tag{C.6}$$

In conclusion, comparing the result with the component notation of a vector product,

$$\boldsymbol{S}_i \times \boldsymbol{S}_j = \sum_{a,b,c} \epsilon_{abc} S_i^a S_j^b \boldsymbol{e}_c, \tag{C.7}$$

we find that the commutator relation we aimed to calculate is

$$\left[\sum_i \sum_r \boldsymbol{S}_i \cdot \boldsymbol{S}_{i+r}, \boldsymbol{S}_k\right] = -i\hbar \sum_r \left(\boldsymbol{S}_{k+r} \times \boldsymbol{S}_k - \boldsymbol{S}_k \times \boldsymbol{S}_{k+r}\right). \tag{C.8}$$

The next commutator is the one connected to the Dzyaloshinskii-Moriya interaction (DMI). It involves the anti-symmetric tensor, $\boldsymbol{D}_{ij} = -\boldsymbol{D}_{ji}$, and reads

$$\left[\sum_{i,r} \boldsymbol{D}_{i,i+r} \cdot \left(\boldsymbol{S}_i \times \boldsymbol{S}_{i+r}\right), \boldsymbol{S}_k\right] = \sum_{i,r} \sum_{a,b,c,d} \epsilon_{abc} D_{i,i+r}^c \left[S_i^a S_{i+r}^b, S_k^d\right] \boldsymbol{e}_d. \tag{C.9}$$

Similiar to the calculations previously, we separate the commutator into pair-wise commutations,

$$\left[S_i^a S_{i+r}^b, S_k^d\right] = S_i^a \left[S_{i+r}^b, S_k^d\right] - \left[S_k^d, S_i^a\right] S_{i+r}^b, \tag{C.10}$$

so that we can use the general spin operator commutation relation from Eq. (C.2). Consequently, we can write Eq. (C.10) as

$$S_i^a \left[S_{i+r}^b, S_k^d\right] - \left[S_k^d, S_i^a\right] S_{i+r}^b = S_i^a i\hbar\delta_{i+r,k} \sum_e \epsilon_{bde} S_k^e - i\hbar\delta_{i,k} \sum_e \epsilon_{dae} S_k^e S_{i+r}^b. \tag{C.11}$$

Considering the starting commutator, we get essentially two terms,

$$\begin{aligned}\left[\sum_{i,r} \boldsymbol{D}_{i,i+r} \cdot \left(\boldsymbol{S}_i \times \boldsymbol{S}_{i+r}\right), \boldsymbol{S}_k\right] &= i\hbar \sum_{i,r} \sum_{a,b,c,d,e} \epsilon_{abc} D_{i,i+r}^c S_i^a \delta_{i+r,k} \epsilon_{bde} S_k^e \boldsymbol{e}_d \\ &\quad - i\hbar \sum_{i,r} \sum_{a,b,c,d,e} \epsilon_{abc} D_{i,i+r}^c \delta_{i,k} \epsilon_{dae} S_k^e S_{i+r}^b \boldsymbol{e}_d,\end{aligned} \tag{C.12}$$

which we will regard separately in the following. For the first term, we again shift the summation index $i \to i - r$. This term then reads

$$i\hbar \sum_{i,r} \sum_{a,b,c,d,e} \epsilon_{abc} D_{i,i+r}^c S_i^a \delta_{i+r,k} \epsilon_{bde} S_k^e \boldsymbol{e}_d = i\hbar \sum_{i,r} \sum_{a,b,c,d,e} \epsilon_{abc} D_{i-r,i}^c S_{i-r}^a \delta_{i,k} \epsilon_{bde} S_k^e \boldsymbol{e}_d. \tag{C.13}$$

Next, we apply the sum over i and re-order the terms and parameters in a convenient way, ensuring that the order of the spin operators S is not altered. This leads to

$$i\hbar \sum_{i,r} \sum_{a,b,c,d,e} \epsilon_{abc} D^c_{i,i+r} S^a_i \delta_{i+r,k} \epsilon_{bde} S^e_k \boldsymbol{e}_d = i\hbar \sum_r \sum_{a,b,c,d,e} \epsilon_{acb} \epsilon_{bed} S^a_{k-r} D^c_{k-r,k} S^e_k \boldsymbol{e}_d. \quad \text{(C.14)}$$

Note that $D^c_{k-r,k}$ is a real number and, thus, commute with any other element. The goal is a representation in vector notation. To do so, we compare Eq. (C.14) with the component notation of a double cross product,

$$(\boldsymbol{A} \times \boldsymbol{B}) \times \boldsymbol{C} = \sum_{i,j,k,m,n} \epsilon_{mni} \epsilon_{ijk} A_m B_n C_j \boldsymbol{e}_k, \quad \text{(C.15)}$$

and immediately see that it can be written as

$$i\hbar \sum_r \sum_{a,b,c,d,e} \epsilon_{acb} \epsilon_{bed} S^a_{k-r} D^c_{k-r,k} S^e_k \boldsymbol{e}_d = i\hbar \sum_r (\boldsymbol{S}_{k-r} \times \boldsymbol{D}_{k-r,k}) \times \boldsymbol{S}_k. \quad \text{(C.16)}$$

By additionally assuming a symmetric lattice and using the (anti-) symmetry of the DMI tensor, the first term of Eq. (C.12) finally concludes to

$$i\hbar \sum_{i,r} \sum_{a,b,c,d,e} \epsilon_{abc} D^c_{i,i+r} S^a_i \delta_{i+r,k} \epsilon_{bde} S^e_k \boldsymbol{e}_d = -i\hbar \sum_r (\boldsymbol{S}_{k+r} \times \boldsymbol{D}_{k,k+r}) \times \boldsymbol{S}_k. \quad \text{(C.17)}$$

Next, we consider the second term of Eq. (C.12), where we can apply the sum and re-order the parameters, again ensuring that the order of the operators does not change. It reads

$$-i\hbar \sum_{i,r} \sum_{a,b,c,d,e} \epsilon_{abc} D^c_{i,i+r} \delta_{i,k} \epsilon_{dae} S^e_k S^b_{i+r} \boldsymbol{e}_d = i\hbar \sum_r \sum_{a,b,c,d,e} \epsilon_{dea} \epsilon_{abc} S^e_k S^b_{k+r} D^c_{k,k+r} \boldsymbol{e}_d. \quad \text{(C.18)}$$

It can be brought into vector notation by comparing it to the component notation of a double vector product, this time

$$\boldsymbol{A} \times (\boldsymbol{B} \times \boldsymbol{C}) = \sum_{i,j,k,m,n} \epsilon_{ijk} \epsilon_{kmn} A_j B_m C_n \boldsymbol{e}_i, \quad \text{(C.19)}$$

leading to

$$i\hbar \sum_r \sum_{a,b,c,d,e} \epsilon_{dea} \epsilon_{abc} S^e_k S^b_{k+r} D^c_{k,k+r} \boldsymbol{e}_d = i\hbar \sum_r \boldsymbol{S}_k \times (\boldsymbol{S}_{k+r} \times \boldsymbol{D}_{k,k+r}). \quad \text{(C.20)}$$

Combing both terms, Eqs. (C.17) and (C.20), we can conclude for the final commutation relation

$$\begin{aligned}\left[\sum_{i,r} \boldsymbol{D}_{i,i+r} \cdot (\boldsymbol{S}_i \times \boldsymbol{S}_{i+r}) \, , \boldsymbol{S}_k\right] = &- i\hbar \sum_r (\boldsymbol{S}_{k+r} \times \boldsymbol{D}_{k,k+r}) \times \boldsymbol{S}_k \\ &+ i\hbar \sum_r \boldsymbol{S}_k \times (\boldsymbol{S}_{k+r} \times \boldsymbol{D}_{k,k+r}) \, .\end{aligned} \tag{C.21}$$

D. Additional simulation results

In the main part, in Chapter 3, the simulation results for a system of two coupled lattices, representing a synthetic antiferromagnet were presented. Here, we show the corresponding simulations for a single-layer AFM square lattice. The results of those simulations are shown in the following figures, D.1, D.2, and D.3. These are the equivalents to Figs. 3.3, 3.4, and 3.7 of the main part. Here we see that they are similar to the simulation results for the bilayer system, which is in accordance to the analytically derived formalism.

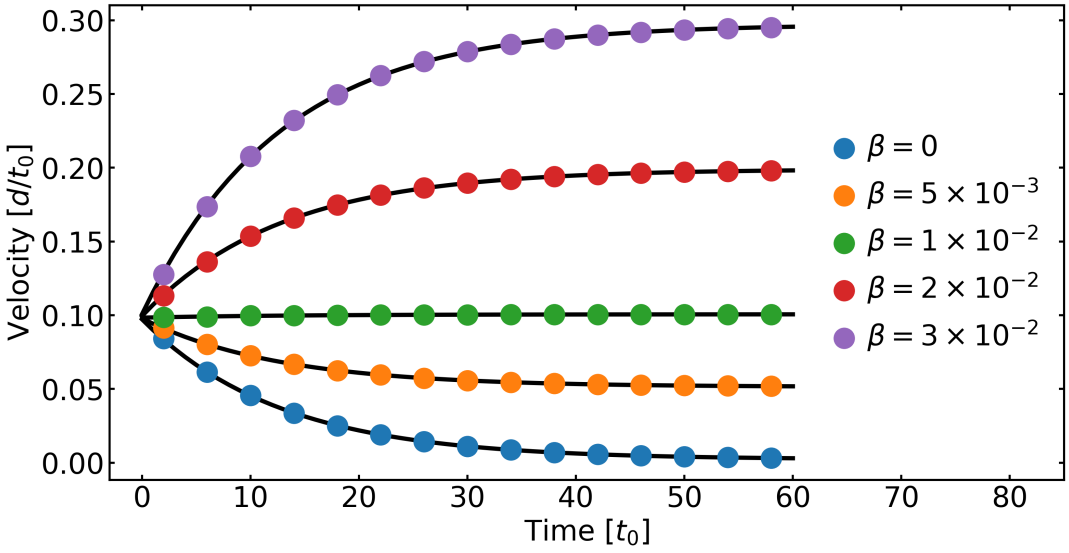

Figure D.1.: Velocity of a Skyrmion in a single-layer antiferromagnetic lattice driven by two uni-directional flowing electric currents over time for different values of the parameter β at $\alpha = 0.01$. While the symbols represent the Skyrmion velocity obtained from the simulation, the solid lines are fits to Eq. (3.48). This is the equivalent to Fig. 3.3 in Ch. 3.

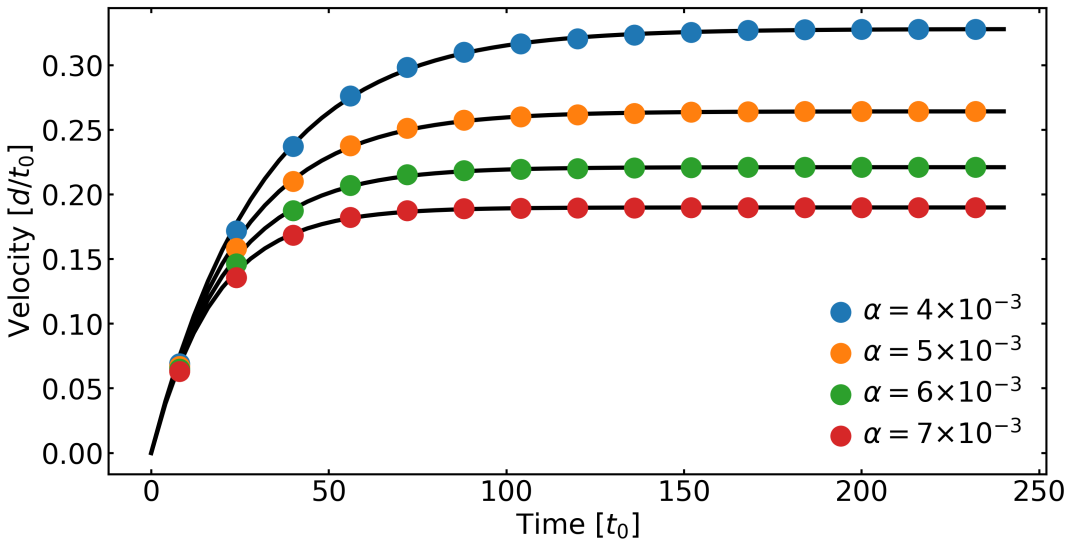

Figure D.2.: Velocity of a Skyrmion in a single-layer antiferromagnetic lattice driven by two anti-parallel flowing electric currents over time for different values of the Gilbert damping parameter α. While the symbols represent the Skyrmion velocity obtained from the simulation, the solid lines are fits to Eq. (3.49). This is the equivalent to Fig. 3.4 in Ch. 3.

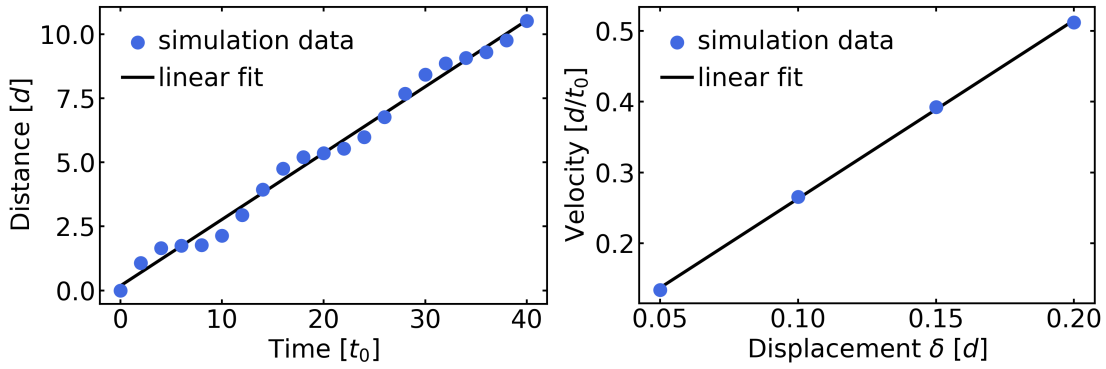

Figure D.3.: Left: Distance traveled by a freely moving Skyrmion in a single-layer antiferromagnetic lattice due to an initial sublattice Skyrmion displacement. The dots mark the distance the Skyrmion traveled in the simulation while the solid line is a linear fit to these distances. Right: Fitted Skyrmion velocity in dependence on the initial displacement. The symbols mark the fitted velocities while the solid line is a linear fit according to Eq. (3.27). This is the equivalent to Fig. 3.7 in Ch. 3.

Bibliography

[1] T. H. R. Skyrme, *A non-linear field theory*, Proc. R. Soc. Lond. A **260**, 127–138 (1961).

[2] A. A. Belavin and A. M. Polyakov, *Metastable states of two-dimensional isotropic ferromagnets*, Pis'ma Zh. Eksp. Teor. Fiz. **22**, 503-506 (1975).

[3] A. N. Bogdanov and D. A. Yablonskiui, *Thermodynamically stable "vortices" in magnetically ordered crystals. The mixed state of magnets*, Sov. Phys. JETP. **68**, 101 (1989).

[4] U. Rößler, A. Bogdanov, and C. Pfleiderer, *Spontaneous skyrmion ground states in magnetic metals*, Nature **442**, 797–801 (2006).

[5] S. Mühlbauer, B. Binz, F. Jonietz, C. Pfleiderer, A. Rosch, A. Neubauer, R. Georgii, and P. Böni, *Skyrmion Lattice in a Chiral Magnet*, Science **323**, 915-919 (2009).

[6] X. Yu, Y. Onose, N. Kanazawa, *et al.*, *Real-space observation of a two-dimensional skyrmion crystal*, Nature **465**, 901–904 (2010).

[7] S. Heinze, K. von Bergmann, M. Menzel, *et al.*, *Spontaneous atomic-scale magnetic skyrmion lattice in two dimensions*, Nature Phys. **7**, 713–718 (2011).

[8] S. S. P. Parkin, H. Masamitsu, and T. Luc, *Magnetic domainwall racetrack memory*, Science **320**, 190 (2008).

[9] C. Kittel, *Physical Theory of Ferromagnetic Domains*, Rev. Mod. Phys. **21**, 541 (1949).

[10] N. Papanicolaou, *Antiferromagnetic domain walls*, Phys. Rev. B **51**, 15062 (1995).

[11] M. Tsoi, R. E. Fontana, and S. S. P. Parkin, *Magnetic domain wall motion triggered by an electric current*, Appl. Phys. Lett. **83**, 2617–2619 (2003).

[12] L. Berger, *Low-field magnetoresistance and domain drag in ferromagnets*, J. Appl. Phys. **49**, 2156–2161 (1978).

[13] O. Gomonay, T. Jungwirth, and J. Sinova, *High Antiferromagnetic Domain Wall Velocity Induced by Néel Spin-Orbit Torques*, Phys. Rev. Lett. **117**, 017202 (2016).

[14] A.V. Mikhailov and A.I. Yaremchnk, *Forced motion of a domain wall in the field of a spin wave*, JETP Lett. **39**, 296-299 (1984).

[15] E. G. Tveten, A. Qaiumzadeh, and A. Brataas, *Antiferromagnetic Domain Wall Motion Induced by Spin Waves*, Phys. Rev. Lett. **112**, 147204 (2014).

[16] M. M. Bogdan, and O. V. Charkina, *Spin waves in easy-axis antiferromagnets with precessing domain walls*, Low Temp. Phys. **40**, 84–89 (2014).

[17] N. Romming, C. Hanneken, M. Menzel, J. E. Bickel, B. Wolter, K. von Bergmann , A. Kubetzka, and R. Wiesendanger, *Writing and Deleting Single Magnetic Skyrmions*, Science **341** ,636-639(2013).

[18] S. Woo, *et al.*, *Observation of room-temperature magnetic skyrmions and their current-driven dynamics in ultrathin metallic ferromagnets*, Nat. Mater. **15**, 501–506 (2016).

[19] S. Meyer, M. Perini, S. von Malottki, *et al.*, *Isolated zero field sub-10 nm skyrmions in ultrathin Co films*, Nat. Commun. **10**, 3823 (2019).

[20] F. Jonietz, *et al.*, *Spin Transfer Torques in MnSi at Ultralow Current Densities*, Science **330**, 1648-1651 (2010).

[21] M. E. Knoester, J. Sinova, and R. A. Duine, *Phenomenology of current-skyrmion interactions in thin films with perpendicular magnetic anisotropy*, Phys. Rev. B **89**, 064425 (2014).

[22] S. Yang, *et al.*, *Fundamentals and applications of the skyrmion Hall effect*, Appl. Phys. Rev. **11**, 041335 (2024).

[23] B. Göbel, A. Mook, J. Henk, and I. Mertig, *Overcoming the speed limit in skyrmion racetrack devices by suppressing the skyrmion Hall effect*, Phys. Rev. B **99**, 020405(R) (2019).

[24] Y. Zhang, *et al.*, *Magnetic skyrmions without the skyrmion Hall effect in a magnetic nanotrack with perpendicular anisotropy*, Nanoscale **9**, 10212–10218 (2017).

[25] Y. Hirata, DH. Kim, S. K. Kim, *et al.*, *Vanishing skyrmion Hall effect at the angular momentum compensation temperature of a ferrimagnet*, Nat. Nanotechnol. **14**, 232–236 (2019).

[26] X. Zhang, Y. Zhou, and M. Ezawa, *Antiferromagnetic Skyrmion: Stability, Creation and Manipulation*, Sci Rep **6**, 24795 (2016).

[27] H. Velkov, O. Gomonay, M .Beens, G. Schwiete, A. Brataas, J. Sinova, and R. A. Duine, *Phenomenology of current-induced skyrmion motion in antiferromagnets*, New J. Phys. **18**, 075016 (2016).

[28] W. Koshibae and N. Nagaosa, *Theory of skyrmions in bilayer systems*, Sci. Rep. **7**, 42645 (2017).

[29] W. Legrand, D. Maccariello, F. Ajejas, S. Collin, A. Vecchiola, K. Bouzehouane, N. Reyren, V. Cros, and A. Fert, *Roomtemperature stabilization of antiferromagnetic skyrmions in synthetic antiferromagnets*, Nat. Mater. **19**, 34 (2020).

[30] B. Göbel, A. Mook, J. Henk, and I. Mertig, *Antiferromagnetic skyrmion crystals: Generation, topological Hall, and topological spin Hall effect*, Phys. Rev. B **96**, 060406(R) (2017).

[31] A. N. Bogdanov, U. K. Rößler, M. Wolf, and K.-H. Müller, *Magnetic structures and reorientation transitions in noncentrosymmetric uniaxial antiferromagnets*, Phys. Rev. B **66**, 214410 (2002).

[32] J. Barker and O. A. Tretiakov, *Static and Dynamical Properties of Antiferromagnetic Skyrmions in the Presence of Applied Current and Temperature*, Phys. Rev. Lett. **116**, 147203 (2016).

[33] P. Bak and M. H. Jensen, *Theory of helical magnetic structures and phase transitions in MnSi and FeGe*, J. Phys. C: Solid State Phys. **13**, L881 (1980).

[34] N. Romming, A. Kubetzka, C. Hanneken, K. von Bergmann, and R. Wiesendanger, *Field-Dependent Size and Shape of Single Magnetic Skyrmions*, Phys. Rev. Lett. **17**, 177203 (2015).

[35] K. Litzius, I. Lemesh, B. Krüger, *et al.*, *Skyrmion Hall effect revealed by direct time-resolved X-ray microscopy*, Nature Phys. **13**, 170–175 (2017).

[36] E. M. Lifshitz and L.P. Pitaevskii, *Statistical Physics, Part 2: Theory of the Condensed State. Vol. 9 of L. D. Landau and E. M. Lifshitz*, Pergamon Press, Oxford, 1980.

[37] I. Dzyaloshinsky, *A thermodynamic theory of "weak" ferromagnetism of antiferromagnetics*, J. Phys. Chem. Solids **4**, 241-255 (1958).

[38] T. L. Gilbert, *A phenomenological theory of damping in ferromagnetic materials*, IEEE Trans. Magn. **40**, 3443-3449 (2004).

[39] G. Tatara, and H. Kohno, and J. Shibata, *Microscopic approach to current-driven domain wall dynamics*, Phys. Rep. **468**, 213-301 (2008).

[40] M. Stier, M. Creutzburg, and M. Thorwart, *Rashba-induced chirality switching of domain walls and suppression of the Walker breakdown*, Phys. Rev. B **90**, 014433 (2014).

[41] J.C. Slonczewski , *Current-driven excitation of magnetic multilayers*, J. Magn. Magn. Mater. **159**, L1-L7 (1996).

[42] A. Thiaville, Y. Nakatani, J. Miltat, and N. Vernier, *Domain wall motion by spin-polarized current: a micromagnetic study*, J. Appl. Phys. **95**, 7049–7051 (2004).

[43] S. Zhang and Z. Li, *Roles of Nonequilibrium Conduction Electrons on the Magnetization Dynamics of Ferromagnets*, Phys. Rev. Lett. **93**, 127204 (2004).

[44] A. Thiaville, Y. Nakatani, J. Miltat, and Y. Suzuki, *Micromagnetic understanding of current-driven domain wall motion in patterned nanowires*, Europhys. Lett. **69**, 990 (2005).

[45] M. Stier, W. Häusler, T. Posske, G. Gurski, and M. Thorwart, *Skyrmion–Anti-Skyrmion Pair Creation by in-Plane Currents*, Phys. Rev. Lett. **118**, 267203 (2017).

[46] S. D. Pollard, L. Huang, K.S. Buchanan, D.A. Arena, and Y. Zhu, *Direct dynamic imaging of non-adiabatic spin torque effects*, Nat. Commun. **3**, 1028 (2012).

[47] S. Zhang and S. S.-L. Zhang, *Generalization of the Landau-Lifshitz-Gilbert Equation for Conducting Ferromagnets*, Phys. Rev. Lett. **102**, 086601 (2009).

[48] A. Yamaguchi, T. Ono, S. Nasu, K. Miyake, K. Mibu, and T. Shinjo, *Real-Space Observation of Current-Driven Domain Wall Motion in Submicron Magnetic Wires*, Phys. Rev. Lett. **92**, 077205 (2004).

[49] N. Vernier, D. A. Allwood, D. Atkinson, M. D. Cooke, and R. P. Cowburn, *Domain wall propagation in magnetic nanowires by spin-polarized current injection*, Europhys. Lett. **65**, 526 (2004).

[50] A. A. Thiele, *Steady-State Motion of Magnetic Domains*, Phys. Rev. Lett. **30**, 230 (1973).

[51] M. Lau, W. Häusler, and M. Thorwart, *Moving skyrmions in antiferromagnets by sublattice displacements*, Phys. Rev. B **111**, 144411 (2025).

[52] J. C. Martinez and M. B. A. Jalil, *Topological dynamics and current-induced motion in a skyrmion lattice*, New J. Phys. **18**, 033008 (2016).

[53] K. Zeissler, S. Finizio, C. Barton, *et al.*, *Diameter-independent skyrmion Hall angle observed in chiral magnetic multilayers*, Nat. Commun. **11**, 428 (2020).

[54] P. Siegl, E. Y. Vedmedenko, M. Stier, M. Thorwart, and T. Posske, *Controlled creation of quantum skyrmions*, Phys. Rev. Research **4**, 023111 (2022).

[55] J.-M. Schwindt, *Tutorium Quantenmechanik*, SpringerSpektrum, Heidelberg, 2016.

[56] W. Heisenberg, *Mehrkörperproblem und Resonanz in der Quantenmechanik*, Z. Phys. **38**, 411–426 (1926).

[57] P. A. M. Dirac, *On the Theory of Quantum Mechanics*, Proc. Phys. Soc. London, Sec. A **112**, 661-677 (1926).

[58] W. Heisenberg, *Zur Theorie des Ferromagnetismus* Z. Phys. **49**, 619–636 (1928).

[59] B. Krüger, *Current-Driven Magnetization Dynamics: Analytical Modeling and Numerical Simulation* (Doctoral dissertation), University of Hamburg (2011).

[60] T. Moriya, *Anisotropic Superexchange Interaction and Weak Ferromagnetism*, Phys. Rev. **120**, 91 (1960).

[61] K. Zakeri, *Probing of the interfacial Heisenberg and Dzyaloshinskii–Moriya exchange interaction by magnon spectroscopy*, J. Phys. Condens. Matter **29**, 013001 (2016).

[62] C. Schütte and M. Garst, *Magnon-skyrmion scattering in chiral magnets*, Phys. Rev. B **90**, 094423 (2014).

[63] A. Auerbach, *Interacting Electrons and Quantum Magnetism*, Springer New York, NY, 1994.

[64] S. Michel and M. Potthoff, *Spin Berry curvature of the Haldane model*, Phys. Rev. B **106**, 235423 (2022).

[65] A. Bogdanov and A. Hubert, *Thermodynamically stable magnetic vortex states in magnetic crystals*, J. Magn. Magn. Mater. **138**, 255-269 (1994).

[66] A. N. Bogdanov, and D. A. Yablonskiui, *Thermodynamicallystable "vortices" in magnetically ordered crystals. The mixed state of magnets*, Zh. Eksp. Teor. Fiz. **95**, 178-182 (1989).

[67] N. Nagaosa and Y. Tokura, *Topological properties and dynamics of magnetic skyrmions*, Nature Nanotech. **8**, 899–911 (2013).

[68] S. Rohart and A. Thiaville, *Skyrmion confinement in ultrathin film nanostructures in the presence of Dzyaloshinskii-Moriya interaction*, Phys. Rev. B **88**, 184422 (2013).

[69] B. Göbel, A. Mook, J. Henk, I. Mertig, and O. A. Tretiakov, *Magnetic bimerons as skyrmion analogues in in-plane magnets*, Phys. Rev. B **99**, 060407 (2019).

[70] R. Skomski, *Simple Models of Magnetism*, Oxford University Press, 2008.

[71] K. Everschor, M. Garst, B. Binz, F. Jonietz, S. Mühlbauer, C. Pfleiderer, and A. Rosch, *Rotating skyrmion lattices by spin torques and field or temperature gradients*, Phys. Rev. B **86**, 054432 (2012).

[72] K. Everschor, *Current-Induced Dynamics of Chiral Magnetic Structures: Skyrmions, Emergent Electrodynamics and Spin-Transfer Torques* (Doctoral dissertation), Universität zu Köln (2012).

[73] K. Everschor-Sitte and M. Sitte, *Real-space Berry phases: Skyrmion soccer*, J. Appl. Phys. **115**, 172602 (2014).

[74] F. N. Rybakov and N. S. Kiselev, *Chiral magnetic skyrmions with arbitrary topological charge*, Phys. Rev. B **99**, 064437 (2019).

[75] A. Thiaville and J. Miltat, *Topology and Magnetic Domain Walls*, In: Zang, J., Cros, V., Hoffmann, A. (eds) Topology in Magnetism. Springer Series in Solid-State Sciences **192**, Springer, 2018.

[76] X. Lv, Y. Huang, K. Pei, C. Yang, T. Zhang, W. Li, G. Cao, J. Zhang, Y. Lai, R. Che, *Manipulating the Magnetic Bubbles and Topological Hall Effect in 2D Magnet* Fe_5GeTe_2 Adv. Funct. Mater. **34**, 2308560 (2024).

[77] A. M. Kosevich, B. A. Ivanov, and A. S. Kovalev, *Magnetic Solitons*, Phys. Rep. **194**, 117–238 (1990).

[78] P. Sutcliffe, *Hopfions in chiral magnets*, J. Phys. A **51**, 375401 (2018).

[79] N. Kent, N. Reynolds, D. Raftrey, *et al.*, *Creation and observation of Hopfions in magnetic multilayer systems*, Nat. Commun. **12**, 1562 (2021).

[80] F. N. Rybakov, N. S. Kiselev, A. B. Borisov, L. Döring, C. Melcher, and S. Blügel, *Magnetic hopfions in solids*, APL Mater. **10**, 111113 (2022).

[81] F. Zheng, N. S. Kiselev, F. N. Rybakov, L. Yang, W. Shi, S. Blügel, and R. E. Dunin-Borkowski, *Hopfion rings in a cubic chiral magnet*, Nature **623**, 718–723 (2023).

[82] S. Komineas and N. Papanicolaou, *Skyrmion dynamics in chiral ferromagnets*, Phys. Rev. B **92**, 064412 (2015).

[83] M. Shen, Y. Zhang, J. Ou-Yang, X. Yang, and L. You *Motion of a skyrmionium driven by spin wave*, Appl. Phys. Lett. **112**, 062403 (2018).

[84] C. Back, *et al.*, *The 2020 skyrmionics roadmap*, J. Phys. D: Appl. Phys. **53**, 363001 (2020).

[85] M. Hassan, *et al.*, *Dipolar skyrmions and antiskyrmions of arbitrary topological charge at room temperature*, Nat. Phys. **20**, 615–622 (2024).

[86] W. Koshibae and N. Nagaosa, *Creation of skyrmions and antiskyrmions by local heating*, Nat Commun **5**, 5148 (2014).

[87] F. Austrup, W. Häusler, M. Lau, and M. Thorwart, *Dynamics of skyrmion shrinking*, Phys. Rev. B **111**, 134446 (2025).

[88] A. Nayak, V. Kumar, T. Ma, *et al.*, *Magnetic antiskyrmions above room temperature in tetragonal Heusler materials*, Nature **548**, 561–566 (2017).

[89] W. Koshibae and N. Nagaosa, *Theory of antiskyrmions in magnets*, Nat. Commun. **7**, 10542 (2016).

[90] S. A. Montoya, *et al.*, *Tailoring magnetic energies to form dipole skyrmions and skyrmion lattices*, Phys. Rev. B **95**, 024415 (2017).

[91] M. Lau, W. Häusler, and M. Thorwart, *Spin wave driven skyrmions in a bipartite antiferromagnetic lattice*, Phys. Rev. B **109**, 014435 (2024).

[92] R. Juge, N. Sisodia, J. U. Larrañaga, *et al.*, *Skyrmions in synthetic antiferromagnets and their nucleation via electrical current and ultra-fast laser illumination*, Nat. Commun. **13**, 4807 (2022).

[93] S. S. P. Parkin, R. Bhadra, and K. P. Roche, *Oscillatory magnetic exchange coupling through thin copper layers*, Phys. Rev. Lett. **66**, 2152 (1991).

[94] Van Tuong Pham *et al.*, *Fast current-induced skyrmion motion in synthetic antiferromagnets*, Science **384**, 307-312 (2024).

[95] J. Masell and K. Everschor-Sitte, *Current-Induced Dynamics of Chiral Magnetic Structures: Creation, Motion, and Applications*, In: Kamenetskii, E. (eds) Chirality, Magnetism and Magnetoelectricity. Topics in Applied Physics **138**, Springer, Cham. (2021).

[96] O. A. Tretiakov, D. Clarke, Gia-Wei Chern, Ya. B. Bazaliy, and O. Tchernyshyov, *Dynamics of Domain Walls in Magnetic Nanostrips*, Phys. Rev. Lett. **100**, 127204 (2008).

[97] E. G. Tveten, A. Qaiumzadeh, O. A. Tretiakov, and A. Brataas, *Staggered Dynamics in Antiferromagnets by Collective Coordinates*, Phys. Rev. Lett. **110**, 127208 (2013).

[98] J. Iwasaki, M. Mochizuki, and N. Nagaosa, *Universal current-velocity relation of skyrmion motion in chiral magnets*, Nat Commun **4**, 1463 (2013).

[99] F. Büttner, C. Moutafis, M. Schneider, *et al.*, *Dynamics and inertia of skyrmionic spin structures*, Nature Phys. **11**, 225–228 (2015).

[100] I. Makhfudz, B. Krüger, and O.Tchernyshyov, *Inertia and Chiral Edge Modes of a Skyrmion Magnetic Bubble*, Phys. Rev. Lett. **109**, 217201 (2012).

[101] D. Wang, H.-B. Braun, and Y. Zhou, *Dynamical mass generation for ferromagnetic skyrmions in two dimensions*, J. Magn. Magn. Mater. **564**, 170062 (2022).

[102] V. P. Kravchuk, D. D. Sheka, U. K. Rößler, J. van den Brink, and Y. Gaididei, *Spin eigenmodes of magnetic skyrmions and the problem of the effective skyrmion mass*, Phys. Rev. B **97**, 064403 (2018).

[103] H. V. Gomonay and V. M. Loktev, *Spin transfer and current-induced switching in antiferromagnets*, Phys. Rev. B **81**, 144427 (2010).

[104] S. Panigrahy, S. Mallick, J. Sampaio and S. Rohart, *skyrmion inertia in synthetic antiferromagnets*, Phys. Rev. B **106**, 144405 (2022).

[105] R. Tomasello, E. Martinez, R. Zivieri, L. Torres, M. Carpentieri, and G. Finocchio, *A strategy for the design of skyrmion racetrack memories*, Sci. Rep. **4**, 6784 (2014).

[106] K. M. D. Hals, Y. Tserkovnyak, and A. Brataas, *Phenomenology of Current-Induced Dynamics in Antiferromagnets*, Phys. Rev. Lett. **106**, 107206 (2011).

[107] A. Salimath, Fengjun Zhuo, R. Tomasello, G. Finocchio, and A. Manchon, *Controlling the deformation of antiferromagnetic skyrmions in the high-velocity regime*, Phys. Rev. B **101**, 024429 (2020).

[108] X. S. Wang, H. Y. Yuan, and X. R. Wang, *A theory on skyrmion size*, Commun. Phys. **1**, 31 (2018).

[109] H.-B. Braun, *Fluctuations and instabilities of ferromagnetic domain-wall pairs in an external magnetic field*, Phys. Rev. B **50**, 16485 (1994).

[110] M. Weißenhofer, L. Rózsa, and U. Nowak, *Skyrmion Dynamics at Finite Temperatures: Beyond Thiele's Equation*, Phys. Rev. Lett. **127**, 047203 (2021).

[111] M. Stier, R. Strobel, S. Krause, W. Häusler, and M. Thorwart, *Role of impurity clusters for the current-driven motion of magnetic skyrmions*, Phys. Rev. B **103**, 054420 (2021).

[112] S. Schroeter and M. Garst, *Scattering of high-energy magnons off a magnetic skyrmion*, Low Temp. Phys. **41**, 817 (2015).

[113] G. Bauer, E. Saitoh, and B. J. van Wees, *Spin caloritronics*, Nature Mater. **11**, 391–399 (2012).

[114] N. Biniskos, *et al.*, *An overview of the spin dynamics of antiferromagnetic* Mn_5Si_3, APL Mater. **11**, 081103 (2023).

[115] P. Siegl, M. Stier, A. F. Schäffer, E. Y. Vedmedenko, T. Posske, R. Wiesendanger, and M. Thorwart, *Creating arbitrary sequences of mobile magnetic skyrmions and antiskyrmions*, Phys. Rev. B **106**, 014421 (2022).

[116] A. F. Schäffer, P. Siegl, M. Stier, T. Posske, J. Berakdar, M. Thorwart, R. Wiesendanger, and E. Y. Vedmedenko, *Rotating edge-field driven processing of chiral spin textures in racetrack devices*, Sci. Rep. **10**, 20400 (2020).

[117] P. Fazekas, *Lecture Notes on Electron Correlation and Magnetism*, World Scientific, Singapore, 1999.

[118] F. Keffer and C. Kittel, *Theory of antiferromagnetic resonance*, Phys. Rev. **85**, 329 (1952).

[119] M. W. Daniels, R. Cheng, W. Yu, J. Xiao, and D. Xiao, *Nonabelian magnonics in antiferromagnets*, Phys. Rev. B **98**, 134450 (2018).

[120] E. G. Tveten, T. Müller, J. Linder, and A. Brataas, *Intrinsic magnetization of antiferromagnetic textures*, Phys. Rev. B **93**, 104408 (2016).

[121] W. Nolting, *Grundkurs Theoretische Physik 3: Elektrodynamik*, Springer Spektrum Berlin, Heidelberg, 2013.

[122] C. Liu, J. Chen, T. Liu, *et al.*, *Long-distance propagation of short-wavelength spin waves*, Nat Commun **9**, 738 (2018).

[123] M. Garst, J. Waizner, and D. Grundler, *Collective spin excitations of helices and magnetic skyrmions: review and perspectives of magnonics in non-centrosymmetric magnets*, J. Phys. D: Appl. Phys. **50**, 293002 (2017).

[124] C. Psaroudaki, P. Aseev, and D. Loss, *Quantum Brownian motion of a magnetic skyrmion*, Phys. Rev. B **100**, 134404 (2019).

[125] M. W. Daniels, W. Yu, R. Cheng, J. Xiao, and D. Xiao, *Topological spin Hall effects and tunable skyrmion Hall effects in uniaxial antiferromagnetic insulators*, Phys. Rev. B **99**, 224433 (2019).

[126] J. Sampaio, V. Cros, S. Rohart, A. Thiaville, and A. Fert, *Nucleation, stability and current-induced motion of isolated magnetic skyrmions in nanostructures*, Nature Nanotech **8**, 839–844 (2013).

[127] J. Iwasaki, A. J. Beekman, and N. Nagaosa, *Theory of magnon-skyrmion scattering in chiral magnets*, Phys. Rev. B **89**, 064412 (2014).

[128] S.-Z. Lin, C. D. Batista, C. Reichhardt, and A. Saxena, *AC current generation in chiral magnetic insulators and skyrmion motion induced by the spin Seebeck effect*, Phys. Rev. Lett. **112**, 187203 (2014).

[129] L. Kong and J. Zang, *Dynamics of an insulating skyrmion under a temperature gradient*, Phys.Rev.Lett. **111**, 067203 (2013).

[130] G. Qin, X. Zhang, R. Zhang, K. Pei, C. Yang, C. Xu, Y. Zhou, Y. Wu, H. Du, and R. Che, *Dynamics of magnetic skyrmions driven by a temperature gradient in a chiral magnet FeGe*, Phys. Rev. B **106**, 024415 (2022).

[131] K. V. Yershov, A. Kákay, and V. P. Kravchuk, *Curvature-induced drift and deformation of magnetic skyrmions: Comparison of the ferromagnetic and antiferromagnetic cases*, Phys. Rev. B **105**, 054425 (2022).

[132] S. Woo, K. M. Song, X. Zhang, *et al.*, *Current-driven dynamics and inhibition of the skyrmion Hall effect of ferrimagnetic skyrmions in GdFeCo films*, Nat. Commun. **9**, 959 (2018).

[133] L. Sánchez-Tejerina, R. Tomasello, V. Puliafito, B. Azzerboni, M. Carpentieri, and G. Finocchio, *Unified Framework for Micromagnetic Modeling of Ferro-, Ferri-, and Antiferromagnetic Materials at Mesoscopic Scale: Domain Wall Dynamics as a Case Study*, IEEE Magn. Lett. **11**, 1-5 (2020).

[134] L. Caretta, M. Mann, F. Büttner, *et al.*, *Fast current-driven domain walls and small skyrmions in a compensated ferrimagnet*, Nature Nanotech. **13**, 1154–1160 (2018).

[135] M. Heigl, S. Koraltan, M. Vaňatka, *et al.*, *Dipolar-stabilized first and second-order antiskyrmions in ferrimagnetic multilayers*, Nat. Commun. **12**, 2611 (2021).

[136] Y. Shen, Q. Zhang, P. Shi, *et al.*, *Optical skyrmions and other topological quasiparticles of light*, Nat. Photon. **18**, 15–25 (2024).

[137] T. He, Y. Meng, L. Wang, *et al.*, *Optical skyrmions from metafibers with subwavelength features*, Nat. Commun. **15**, 10141 (2024).

[138] A. Vansteenkiste, J. Leliaert, M. Dvornik, M. Helsen, F. Garcia-Sanchez, B. Van Waeyenberge, *The design and verification of MuMax3*, AIP Advances **4**, 107133 (2014).

[139] M. Donahue, *OOMMF User's Guide, Version 1.0*, 6376, National Institute of Standards and Technology, Gaithersburg, MD (1999).

[140] Cuda toolkit, URL: https://developer.nvidia.com/cuda-toolkit.

[141] Boost C++ libraries, URL: https://www.boost.org.

[142] K. Ahnert, D. Demidov, and M. Mulansky, *Solving Ordinary Differential Equations on GPUs*, In: Kindratenko, V. (eds) Numerical Computations with GPUs, Springer, 2014.

[143] A. Kaw and E. Kalu, *Numerical Methods with Applications: Abridged*, (Lulu.com, 2008), ISBN 978-0-578-05765-1.

[144] C. R. Harris, K. J. Millman, S. J. van der Walt, *et al.*, *Array programming with NumPy*, Nature **585**, 357 (2020).

Eidesstattliche Versicherung

Hiermit versichere ich an Eides statt, die vorliegende Dissertationsschrift selbst verfasst und keine anderen als die angegebenen Hilfsmittel und Quellen benutzt zu haben.
Sofern im Zuge der Erstellung der vorliegenden Dissertationsschrift generative Künstliche Intelligenz (gKI) basierte elektronische Hilfsmittel verwendet wurden, versichere ich, dass meine eigene Leistung im Vordergrund stand und dass eine vollständige Dokumentation aller verwendeten Hilfsmittel gemäß der Guten wissenschaftlichen Praxis vorliegt. Ich trage die Verantwortung für eventuell durch die gKI generierte fehlerhafte oder verzerrte Inhalte, fehlerhafte Referenzen, Verstöße gegen das Datenschutz- und Urheberrecht oder Plagiate.

Hamburg, den _____ Unterschrift: _____